Imperial College London
Department of Chemistry

Fourier Transform Infrared Spectroscopic Imaging of Live Cells

Benjamin J. Turner

February 17, 2018

Supervised by Sergei G. Kazarian, Marina Kuimova, and Bernadette Byrne

Submitted in part fulfilment of the requirements for the degree of
Doctor of Philosophy in Chemistry of Imperial College London
and the Diploma of Imperial College London

I would like to dedicate this thesis to my family for all their help and support.

Declaration

This thesis is a description of the work carried out in the Department of Chemical Engineering at Imperial College London between October 2013 and September 2017 under the supervision of Professor Sergei Kazarian. Except where acknowledged, the material is the original work of the author and no part of it has been submitted for a degree at any other university.

Copyright

The copyright of this thesis rests with the author and is made available under a Creative Commons Attribution Non-Commercial No Derivatives licence. Researchers are free to copy, distribute or transmit the thesis on the condition that they attribute it, that they do not use it for commercial purposes and that they do not alter, transform or build upon it. For any reuse or redistribution, researchers must make clear to others the licence terms of this work.

Abstract

There is an increasing demand for label-free methods of cell analysis in fields such as cell biology, drug discovery, and medical diagnostics. Many optical techniques have been developed to this end, which typically use physical properties such as refractive index to better visualise cells without the need for fluorescent markers. However, if chemical information about the sample is desired then these techniques provide limited information.

Fourier Transform Infrared (FTIR) spectroscopic imaging has emerged as a powerful analytical tool that has been used to study a wide variety of biological samples. By using a focal plane array (FPA) detector, thousands of spatially resolved infrared spectra can be recorded simultaneously, creating a chemical map of a sample. FTIR spectroscopic imaging is also a label-free and inherently non-destructive form of measurement. However, due to the high molar absorptivity of water, the use of FTIR spectroscopic imaging to study living cells remains challenging. As cells must be maintained in an aqueous environment, severe restrictions are placed on the maximum path lengths that can be used in infrared spectroscopic imaging experiments.

The purpose of this research was to further develop the application of micro attenuated total reflection (ATR)-FTIR spectroscopic imaging to the study of live cells. Micro ATR-FTIR spectroscopic imaging avoids the path length restriction seen in transmission mode, as the path length is not dependent on the sample's thickness. This means micro ATR-FTIR spectroscopic imaging can be done in bulk aqueous environments. A robust methodology to culture adherent cells directly on an ATR crystal surface was developed, and the extent to which subcellular features can be visualised was investigated. Multiple-reflection ATR spectroscopy of live cells is also presented. This thesis then presents for the first time the detection of an exogenous molecule within a living cell by FTIR spectroscopic imaging. The recently developed analysis method disrelation mapping was also applied to a spectroscopic imaging dataset of a single living cell. Evidence of a different distribution of molecular states of water, compared to that seen in bulk water, was detected in living cells.

Acknowledgements

I would like to thank my supervisors Professor Sergei Kazarian, Dr Marina Kuimova, and Dr Bernadette Byrne, for giving me the chance to undertake this PhD project. I particularly thank Sergei Kazarian for his exceptional patience throughout the project and all I have learned from him. I found Sergei's enthusiasm for research and work ethic particularly inspiring. I would also like to thank Professor Oscar Ces, who greatly assisted me in finding this PhD project.

I benefited from the help and training of many post docs, fellow students, and academic visitors throughout my PhD. I would like to thank Dr Jennifer Dougan, Dr Maxime Boulet-Audet, Dr Shinzawa Hideyuki, Dr Andrew Ewing, and Alessandra Vichi, for all their training, support, and interesting conversation. I would particularly like to thank Dr James Kimber for his continuous support, advice, and friendship. I would also like to thank the Agilent Engineer Daniel Barry, who went above and beyond to help the Kazarian group.

Most importantly, I would like to thank Dr Rebecca Luxton. I would not even have applied to the Institute of Chemical Biology without her support. I wouldn't know what day it was, let alone successfully complete a PhD, without her love, support, and persistent attempts to remind me what I should be doing. Finally, I would also like to thank my parents, brothers, and sister for all their support and most importantly their patience.

Contents

Declaration **3**

Copyright **4**

Abstract **5**

Acknowledgements **6**

List of Figures **10**

List of Tables **17**

List of Symbols **19**

List of Abbreviations **21**

Publications and Conferences **23**

1 Introduction **24**

1.1 Objectives 26

2 Literature Review **27**

2.1 Cell Architecture 27

2.2 Label-Free Imaging 29

2.3 FTIR Theory 31

2.3.1 Molecular Vibrations 31

2.3.2 Vibrational Transitions 32

2.4 Mid-Infrared Spectroscopy Instrumentation 35

2.5 Sampling Modes 38

2.5.1 Transmission 38

2.5.2 Attenuated Total Reflection 38

2.5.3 FTIR Spectroscopic Imaging 40

2.6 Univariate Spectral Analysis 42

2.7 Multivariate Spectral Analysis 43

2.8 Generalised 2D Correlation Spectroscopy . . . 44
2.9 FTIR Spectroscopy of Live Cells . . . 47
2.9.1 Spatial Resolution in FTIR Microscopes . . . 48
2.9.2 Path Length Restrictions of Aqueous Samples . . . 49
2.9.3 FTIR Spectroscopy Using a Synchrotron Source . . . 50
2.9.4 Effect of Chromatic Aberration from IR Transparent Windows 51
2.10 Transmission Mode FTIR Spectroscopy and Spectroscopic Imaging . 52
2.10.1 Protein Conformation . . . 52
2.10.2 Cell Cycle . . . 53
2.10.3 Spectral Changes from Exogenous Molecules . . . 53
2.11 ATR-FTIR Spectroscopy and Spectroscopic Imaging . . . 54
2.12 Raman Spectroscopy . . . 55

3 Experimental 57
3.1 Cell Culture Equipment and Reagents . . . 57
3.1.1 Subculturing . . . 57
3.1.2 Cell Freezing Protocol . . . 57
3.1.3 Cell Thawing Protocol . . . 58
3.2 Multiple-Reflection ATR-FTIR Spectroscopy Measurements . . . 58
3.3 Micro ATR-FTIR Spectroscopic Imaging . . . 59
3.4 Data Import . . . 62
3.5 Matlab GUI . . . 63
3.6 Integration Methods . . . 63

4 ATR Spectroscopy and Spectroscopic Imaging of Live Cells 65
4.1 Introduction . . . 65
4.2 Methodology Development . . . 66
4.2.1 Chamber . . . 66
4.2.2 Experimental Procedure . . . 67
4.2.3 Water Vapour Removal . . . 67
4.2.4 Surface Modification of Germanium Accessory . . . 69
4.3 Results and Discussion . . . 70
4.3.1 Spatial Resolution of Micro ATR-FTIR Spectroscopic Imaging 70
4.3.2 Cell Morphology on Germanium Surface . . . 71
4.3.3 Cell Detection Using the Amide II Band . . . 72
4.3.4 Visualising the Cell Nucleus . . . 74
4.3.5 Visualising other Sub-Cellular Regions . . . 76
4.4 Conclusion . . . 78

5 ATR-FTIR Spectroscopy and Spectroscopic Imaging for Drug Detection in Living Cells 79
5.1 Introduction . . . 79
5.2 Multiple-Reflection ATR-FTIR Spectroscopy . . . 81
5.2.1 Sample Preparation . . . 81
5.2.2 Instrument Setup . . . 81
5.2.3 Heating System . . . 82
5.3 Results and Discussion . . . 82
5.3.1 Multiple-Reflection Accessory . . . 82
5.3.2 Cell Tolerance to DMSO . . . 84
5.3.3 Detecting the Cellular Uptake of Metal-Carbonyl Derivative . 85
5.3.4 Metal-Carbonyl Band Shift . . . 87
5.4 Germanium ATR-FTIR Spectroscopic Imaging . . . 88
5.4.1 Instrument Settings . . . 88
5.4.2 Experimental Setup . . . 88
5.5 Results and Discussion . . . 89
5.5.1 Cell Detection . . . 89
5.5.2 Drug Detection . . . 90
5.5.3 Sub-Cellular Localisation . . . 90
5.6 Conclusion . . . 92

6 Two-Dimensional Correlation Analysis to Investigate Molecular States of Water in Living Cells 93
6.1 Introduction . . . 93
6.2 Methods . . . 95
6.2.1 Sample Preparation . . . 95
6.2.2 Experimental Setup . . . 95
6.2.3 2D Correlation Analysis . . . 95
6.2.4 Disrelation Mapping . . . 96
6.3 Results and Discussion . . . 97
6.3.1 2D Correlation Analysis of Water Perturbed by Temperature . 97
6.4 2D Correlation Analysis of Cell Adhesion . . . 99
6.5 Disrelation Mapping of the OH Stretching Region . . . 101
6.6 Disrelation Mapping of the Amide/OH Region . . . 104
6.7 Conclusion . . . 107

7 Conclusion and Future Work 108
7.1 ATR-FTIR Spectroscopic Imaging of Live Cells . . . 108

7.2 Micro ATR-FTIR Spectroscopic Imaging for Drug Detection within Living Cells 109
7.3 Disrelation Mapping to Investigate Molecular States of Water in Live Cells 109
7.4 Overall Conclusions 110
7.5 Recommendations for Future Work 111

Bibliography **112**

Appendices **128**

List of Figures

2.1 Image illustrating the main organelles of a typical animal cell. The nucleus contains the cells DNA. The mitochondrion carries out aerobic respiration, providing energy for the cells endothermic processes. The lysosome breaks down foreign material within the cell. The centrioles are primarily used during cell mitosis. The smooth and rough endoplasmic reticulum is involved in the synthesis of proteins. The image was taken from Norman and Lodwich (2007) 28
2.2 Illustration of the cell cycle phases. G_0: the cell is not participating in the cell cycle. G_1: RNA and proteins essential for the phase S are produced. S: DNA is replicated. G_2: the cell prepares for mitosis. M: cell undergoes mitosis and splits into 2 daughter cells. 29
2.3 Image taken from Alberts et al. (2002) illustrating different phase contrast methods. Four images are shown of the same fibroblast cell in culture. The images were taken using: (A) Bright-field microscopy, (B) Phase-contrast microscopy, (C) DIC microscopy, (D) Dark-field microscopy 30
2.4 Illustration of the eigenfunctions corresponding to the vibrational energy states. The graph depicts the probability amplitude as a function of displacement from the equilibrium position. The red line shows a classical harmonic oscillator equation. The blue lines show the quantum oscillator eigenfunctions of the first three energy levels 33
2.5 Schematic of a Michelson interferometer adapted from Jackson (2006). Infrared light passes through a beam splitter, where half of the light is sent to a fixed mirror and rest to a moving mirror. The two beams of polychromatic light are then recombined and superimpose. 36
2.6 Illustration of an interferogram and its corresponding spectrum (adapted from Atkins and de Paula (2002)). The two are related by the Fourier transform. 37
2.7 Illustration of attenuated total reflection 39

2.8 Illustration of the structure of a spectroscopic imaging dataset. (Adapted from Kidder et al. (2006)) 42
2.9 Illustration of the method for generating an integrated absorbance image using method A integration. The spectral range of interest is integrated to get the integrated absorbance. This is carried for the spectrum recorded by each pixel. The integrated absorbance is then plotted as a function of pixel position. 43
2.10 Illustration of the linear algebra equation common to classical least squares, principal component analysis, and multivariate curve resolution. 44
2.11 Figure taken from Miller and Dumas (2010) showing an absorbance spectrum of a fixed cell compared to the transmittance spectrum of water. 47
2.12 Illustration of using an additional lens to remove chromatic aberration. Section (A) illustrates chromatic aberration through an infrared transparent window. Section (B) shows the addition of the lens to the top window, forming a pseudo-hemisphere. This has the same effect as using a hemispherical solid immersion lens. This increases the spatial resolution by 1.4× in addition to removing chromatic aberration. Part (C) shows the setup for samples between two windows. A bottom lens is added to improve illumination from the condenser . . . 51

3.1 The Specac multiple-reflection ATR accessory. Infrared light travels into the sample compartment from the right and hits mirror 1. Mirror 1 controls the angle infrared light meets the ATR crystal. Mirror 2 aligns the path from the accessory to the detector. Screw 1 fixes the accessory position in the sample compartment. Dials 1 and 2 on the stage ensure the accessory is level. (B) The same ATR accessory within the spectrometer's sample compartment and connected to a purged air supply. 59
3.2 Agilent's germanium micro-ATR accessory. Picture (A) shows the accessory inverted. Picture (B) shows the same accessory mounted on the Agilent microscope objective. 60

3.3 (A) Live view of the illumination of the FPA detector in ATR mode when the germanium accessory is well aligned. (B) Settings to achieve the maximum dynamic range from the ADC. (C) Live view of the FPA detector while the germanium accessory is in contact with a USAF 1951 resolution target, after a non-uniformity correction. (D) The corresponding visible image. 61
3.4 Screen shot of the Matlab GUI developed for spectroscopic image analysis. The GUI shows an integrated absorbance image on the right. By clicking on a pixel of interest its spectrum is plotted in the graph in the middle. 63
3.5 Illustration of the four main different integration methods used in univariate analysis of spectroscopic images. These methods, using Bruker's nomenclature, are referred to as: (A) method A, (B) method B, (C) method P, (D) method R. 64

4.1 Reproduced from Kuimova et al. (2009). (A) A typical spectrum of a cell from a germanium micro ATR-FTIR imaging dataset. (B) Pictures illustrating the chamber used to ensure cells were submerged in medium throughout incubation and measurement. (C) Integrated absorbance images showing the chemical distribution of amide II, phosphate I, and glycogen. 66
4.2 Pictures illustrating the new chamber designed for ATR-FTIR spectroscopic imaging experiments on live cells. Picture (A) shows the chamber mounted on the Ge accessory. Picture (B) shows the chamber inverted. The needle illustrates a small hole in the side of the chamber. This was to ensure gaseous exchange during incubation when the top of the chamber is sealed. 67
4.3 Plot (A) shows two spectra taken from the same FTIR spectroscopic imaging dataset but different pixels. The blue and red spectra are typical of cell medium and cells respectively. Plot (B) shows the same two spectra after water vapour has been optimally subtracted . 68
4.4 Pictures illustrating the difference in surface wettability of a germanium disk before (A) and after (B) UV/ozone cleaning. From the side on view it can be seen that the contact angle has been reduced to zero in picture (B) after UV/ozone cleaning. 69

4.5 Integrated absorbance image of a polymer laminate obtained using micro ATR mode, adapted from Kimber et al. (2016). Plot (A) shows the integrated absorbance of one row of pixels extracted from integrated absorbance image (B). A sigmoid function has been fitted to plot (A) to assess the spatial resolution. 70
4.6 Visible images of cells directly on the Ge ATR accessory 16 hours after seeding. Both Images were acquired using a visible microscope in reflection mode. Image (A) shows the result of poly-L-lysine coating. Image (B) shows the result of UV/ozone cleaning. 71
4.7 Integrated absorbance images of amide II (A) and amide I (B). 72
4.8 Integrated absorbance images of amide II before (A) and after (B) a 3×3 box filter was applied to the image. Image (C) and (D) show the results of k-means cluster analysis of image (A) and (B) respectively. Each colour represents membership to a different cluster. Plot (E) shows the average spectrum taken from all of the clusters in image (D). 73
4.9 Spectrum recorded from one FPA pixel before (A) and after (B) cell medium subtraction. 74
4.10 Integrated absorbance images of phosphate I before (A) and after (B) a 3×3 box filter is applied to the image. Image (C) and (D) are (A) and (B) respectively, with image area corresponding to cell medium discarded 75
4.11 Plot (A) shows spectra illustrating the difference in lineshape of the phosphate I band in different regions of the cell. The yellow and blue spectrum correspond to the cytoplasm and nucleus respectively. The green spectrum was generated by averaging the whole cell. Image (B) shows the integrated absorbance of phosphate I with the area known to correspond to cell medium discarded. The blue and yellow squares indicate the area averaged to generate the spectra seen in plot (A). . 76
4.12 (A) Image of the integrated absorbance ratio between the CH_2 and CH_3 bands. (B) Integrated absorbance image of the glycogen band at 1030 cm^{-1}. Image (C) is identical to image (B), except the image area corresponding to cell medium has been removed. (D) Average spectrum generated from the red square indicated in image (C). . . . 77

5.1 Schematic of the chemical structure of the metal-carbonyl based compound, kindly provided by the Policar group. Referred to in the text as compound **1** 81

5.2 Illustration of the two setups to heat the multiple-reflection ATR accessory. Picture (A) shows the use of a heated aluminium lid. A PDMS spacer is between the aluminium lid and the ATR accessory to create a seal. A platinum temperature sensor is attached to the heater directly. Picture (B) shows the setup to heat the accessory directly. Two 20 W heaters and the temperature sensor were attached to the ATR top-plate. An acetate lid and PDMS spacer was used to create a seal. 82
5.3 Spectral kinetic illustrating the increase in absorbance of bands corresponding to cells as the cell population adheres to the germanium ATR crystal surface 83
5.4 Spectral kinetic (A) and picture (B) show that cells were found to be mostly dead after 16 hours when the ATR top-plate was heated directly. Spectral kinetic (C) and picture (d) indicate that, although showing limited growth, cells remained viable 16 hours when the heated top plate was used. 84
5.5 (A) Spectra illustrating the reduction in spectral band absorbance as a result of adding DMSO. Picture (B) shows cell exposure to trypan blue after the experiment, indicating cells are still viable 4 hours after DMSO addition 85
5.6 Spectral kinetic from a multiple-reflection ATR-FTIR experiment. The increase in absorbance of metal-carbonyl bands can be seen, indicating an accumulation of the metal-carbonyl derivative compound within cells. 85
5.7 Integrated absorbance of amide II and the A_1-band versus time. The absorbance kinetics have been vector normalised to more easily view the two profiles together. 86
5.8 Spectral kinetic illustrating the spectral band changes within the first 60 minutes (A) and 60 minutes onwards (B) 87
5.9 Spectral kinetic illustrating the shift to lower wavenumber of the metal-carbonyl bands 88
5.10 Integrated absorbance image using the amide II band showing cells (A) before and (B) 40 minutes after incubation with compound **1** . . 89
5.11 k-means clustering of the Amide II integrated absorbance image. Each colour represents membership to a distinct cluster. The spectra in plot (A) show the average spectrum from each cluster in image (B) of the corresponding colour. 90

5.12 Integrated absorbance images generated using the metal-carbonyl E band (A) and the cell's phosphate I band (B). The red and blue spectrum in plot (C) shows the average spectrum from the red and blue marked regions indicated in both images (A) and (B). 91

6.1 Schematic showing the generation of disrelation maps from two method P absorbance images. 97
6.2 (A) Illustration of the linear baseline distortion caused by the change in temperature. (B) A spectral kinetic showing the changes in water's OH stretching band as a function of temperature, after a linear offset correction was applied to the data. 98
6.3 Synchronous (A) and asynchronous (B) spectrum generated from generalised 2D correlation analysis of the spectra presented in figure 6.2. 98
6.4 Spectra at 0 minutes and 4 hours after seeding cells onto the ZnSe ATR crystal at room temperature. Although measurements were taken every 10 minutes for 4 hours, only the first and last spectrum are shown here. 99
6.5 Part (A) and (B) show the synchronous and asynchronous 2D correlation spectrum, respectively, of the OH stretching region from the spectral kinetic shown in figure 6.4. Part (C) and (D) show the synchronous and asynchronous 2D correlation spectrum from the same spectral kinetic in the fingerprint region 100
6.6 (A) Integrated absorbance image of amide II. The line illustrates the spectra extracted for disrelation analysis. The plots below show the extracted spectra after an offset-correction at (B) 3700 cm^{-1} in the 3600 - 3000 cm^{-1} region, and (C) 1750 cm^{-1} in 1750 - 1450 cm^{-1} region. 102
6.7 Synchronous (A) and disrelation (B) analysis of the spectra extracted from the line illustrated in figure 6.6. Image (C) shows a disrelation map generated from the disrelation intensity between 3220 cm^{-1} and 3420 cm^{-1}. 103
6.8 (A) Disrelation analysis of the amide region between 1750-1400 cm^{-1} with the OH stretching region between 3000-3600 cm^{-1}. The crosspeaks at 3420/1640 cm^{-1} and 3420/1540 cm^{-1} show there is out-of-phase variation between protein and intermediately bound water. The disrelation maps were generated using the following crosspeaks: (B) 1540/3420 cm^{-1}, (C) 2930/3420 cm^{-1}, (D) 1080/3420 cm^{-1}. Significant disrelation intensity been be seen at the cell/cell medium interface in image (B) but not in images (C) and (D). 105

6.9 Asynchronous spectrum between fingerprint region and OH stretching region of the spectral kinetic presented in figure 6.4. 106

List of Tables

2.1 Table illustrating the percentage mass of the main macromolecules within a cell. Information was taken from Alberts et al. (2002) 28

2.2 ATR crystal properties (Pike Technologies, 2011). n_1 = refractive index of crystal; LWL = long wavelength limit. d_p = depth of penetration at 1000 cm^{-1}. 40

7.1 Table summarising the properties of the main label-free microscopy techniques discussed in section 2.2.*Lateral resolution of infrared spectroscopic imaging is typically 8 µm in transmission mode and 3 µm in ATR mode. 128

List of Symbols

Symbol	Description	Unit
A	absorbance	-
C	probability amplitude	-
$C*$	probability amplitude complex conjugate	-
c	concentration	$\mathrm{mol\,dm^{-3}}$
D_{IR}	difference spectrum	-
d_p	depth of penetration	m
E	energy	J
H	Hamiltonian	J
h	planck's constant	$\mathrm{J\,s}$
$\hbar$	reduced planck's constant	$\mathrm{J\,s\,rad^{-1}}$
I	intensity	$\mathrm{W\,m^{-2}}$
l	path length	m
L	Spectral length	-
n	integer	-
m	mass	kg
N	iso-noda matrix	-
S	spectrum	-
T	transmittance	-
X	correlation spectrum	-
x_0	position of equilibrium	m
x	distance	m
Y	discrete dynamic spectrum	-
$\tilde{y}$	dynamic spectrum	-
Z	discrete orthogonal spectrum	-
ϵ	molar absorptivity	$\mathrm{dm^3\,mol^{-1}\,cm^{-1}}$
η	refractive index	-
θ	angle	rad
λ	wavelength	m
Λ	disrelation spectrum	-
μ	dipole moment	$\mathrm{C\,m}$
ν	vibrational quantum number	-
ν_n	spectral variable	-

Symbol	Description	Unit
$\tilde{\nu}$	wavenumber	cm^{-1}
Ψ	asynchronous spectrum	-
ρ	energy density	$\mathrm{J\,m}^{-1}$
Φ	synchronous spectrum	-
ω	angular frequency	$\mathrm{rad\,s}^{-1}$
ψ	wavefunction	-

List of Abbreviations

Abbreviations	Description
ADC	analogue to digital converter
AFM	atomic force microscopy
AFM-IR	atomic force microscopy infared
ATR	attenuated total reflection
CaF_2	calcium fluoride
CARS	coherent anti-Stokes Raman
CHO	chinese hamster ovary cell line
DIC	differential interference contrast
DMEM	Dulbecco's modified Eagle's medium
DMSO	dimethyl sulfoxide
DTGS	deuterated triglycine sulfate
FACS	fluorescence-activated cell sorting
FBS	fetal bovine serum
FPA	focal plane array
FTIR	Fourier transform infrared
Ge	germanium
GUI	graphical user interface
HCA	hierarchical cluster analysis
HEK	human embryonic kidney cell line
HeNe	helium neon
IRE	internal reflection element
L-15	Leibovitz's Medium
LRD	least resolvable distance
MCT	mercury cadmium telluride

Abbreviations	Description
NA	numerical aperture
OPD	optical path difference
PBS	phoshate buffered saline
PCA	principal component analysis
PDMS	polydimethylsiloxane
PTFE	polytetrafluoroethylene
RSR	resonance Raman spectroscopy
SERS	surface enhanced Raman scattering
SKOV	human ovary cancer cell line
SNOM	scanning near-field optical microscopy
SOD1	superoxide dismutase 1
SPR	surface plasmon resonance
T25	25 cm^3 tissue culture flask
T75	75 cm^3 tissue culture flask
TCDD	2,3,7,8-tetrachlorodibenzo-p-dioxin
TERS	tip enhanced Raman spectroscopy
TIR	total internal reflection
ZnS	zinc sulphide

Publications and Conferences

Publications

Shinzawa, H., Turner, B., Mizukado, J., Kazarian, S. G., 2017. Protein hydration in living cells probed by Fourier transform infrared (FT-IR) spectroscopic imaging. Analyst, 142, 2475-2483

Kimber, J. A., Foreman, L., Turner, B., Rich, P., Kazarian, S. G., 2016. FTIR spectroscopic imaging and mapping with correcting lenses for studies of biological cells and tissues. Faraday Discuss., 187, 69-85

Taylor, J. D., Hawthorne, W. J., Lo, J., Dear, A., Jain, N., Meisl, G., Andreasen, M., Fletcher, C., Koch, M., Darvill, N., Scull, N., Andrés, E., Sefer, L., Wenman, R., Lambert, S., Jean, J., Xu, Y., Turner, B., Kazarian, S. G., Chapman, M. R., Bubeck, D., de Simone, A., Knowles, T. P., Matthews, S. J., 2016. Electrostatically-guided inhibition of curli amyloid nucleation by the CsgC-like family of chaperones. Scientific Reports., 6, 2045-2322

Conferences

The International Society for Clinical Spectroscopy Summer School, Lake Windermire, UK, 2016

Clinical Infrared and Raman Spectroscopy Network Conference, University of Exeter, UK, 2015. Poster: Fourier Transform Infrared Imaging of Live Cells.

Outreach

Imperial Festival, Chemical Photography, May 2016

Imperial Festival, Chemical Photography, May 2014

1 Introduction

There is a continuous demand to improve and develop new methods to study biological systems such as cells and tissue. For example, pharmaceutical companies are in great need of more effective methods in early stage drug discovery. Target based approaches have dominated the industry for the last 25 years, but the high failure rate of hit compounds has renewed interest in phenotypic based methods (Fang, 2014). These experiments require living cells, increasing demand for robust technology that can analyse cell behaviour in a high throughput manner (Moffat et al., 2017).

Fluorescence based techniques have dominated cell microscopy because, once an appropriate fluorescent labelling strategy has been developed, it can give very sensitive measurements with high specificity, depending on the nature of the fluorescent marker. Fluorescence microscopy can be combined with super resolution techniques to achieve nanoscale resolution (van de Linde et al., 2012), and can achieve single molecule sensitivity with techniques such as total internal reflection fluorescence microscopy (Sako and Uyemura, 2002).

One disadvantage of fluorescence microscopy is that the R&D effort is often considerable to develop fluorescent labelling strategies to study a new system. Another problem is that there is often unwanted interference from the labelling species. For example, the most common method to measure the uptake and distribution of a drug within a cell is to use a fluorescent analogue or to modify the drug with a fluorescent tag (Zheng et al., 2011). Using these types of approaches sub-cellular resolution is achievable (Balaz and Lukacova, 2002), but it is questionable whether what is being measured is representative of the drug in its native form. These disadvantages have lead to the increasing interest in label-free methods to study drug-cell interactions (Yamauchi et al., 2011; Kasprowicz et al., 2017). Visible light microscopy techniques have been developed to exploit inherent physical differences within cells, such as refractive index, to generate image contrast (Kühn et al., 2013). These techniques have shown promise in phenotypic screening of cells (Rappaz et al., 2014; Pavillon et al., 2014) and label-free inspection of tissue samples (Kandel et al., 2017). Optical biosensors based on bioelectrical impedance have also been developed for label-free

studies of live cells (Fang, 2006).

Infrared spectroscopic imaging has also emerged as a label-free and non-destructive way to analyse biological samples, using molecular vibrations to generate image contrast. Imaging methods based on vibrational spectroscopy can provide chemical information about a sample, which can be hard to extract from the aforementioned label-free techniques. Infrared spectroscopic imaging has been applied to the analysis of a variety of biological samples and can be used to probe biochemical changes within samples (Chan and Kazarian, 2016). When combined with multivariate analysis, FTIR spectroscopy can discriminate between normal and cancerous tissue, and a variety of other disease states (Bellisola and Sorio, 2012; Walsh et al., 2012). This has lead to applications of FTIR spectroscopic imaging as a quantitative and label-free tool for histopathology (Pilling and Gardner, 2016). FTIR spectroscopy also has the potential to detect exogenous molecules within biological samples directly, and there is evidence that biochemical changes reflected in spectral bands can be used to discriminate drug modes of action (Draux et al., 2009; Flower et al., 2011; Derenne et al., 2011).

Although much more challenging, interest has also grown in the use of infrared spectroscopy to study live cells. The advantage of doing so is the removal of perturbations caused by fixation and drying, which are now known to distort the infrared spectrum (Li et al., 2017; Vaccari et al., 2012b). Another disadvantage of fixation or drying cells is that the scope for kinetic experiments is limited. There is also the danger of misidentifying spectral changes caused by the cell's normal dynamic processes, such as the cell cycle, as being associated with disease states (Jimenez-Hernandez et al., 2015; Bedolla et al., 2013; Boydston-White et al., 1999). However, there are major technical challenges associated with FTIR spectroscopy of live cells. Of particular concern is the high absorbance of water in the mid-infrared region. Cells are both mostly water and need to be maintained in aqueous environments to remain alive. Most FTIR spectroscopy studies have been done in transmission mode and this necessitates the use of very small path lengths. The high percentage presence of water also makes detecting trace elements of interest more challenging.

An alternative form of infrared spectroscopic imaging that avoids this problem is ATR-FTIR spectroscopic imaging. As the path length is not dependent on the thickness of the sample, ATR-FTIR spectroscopic imaging allows experiments to be conducted in bulk aqueous environments without saturation. ATR-FTIR spectroscopic imaging can also achieve a higher spatial resolution than is possible with transmission mode imaging in air, due to the high refractive index of ATR crystals. Despite these advantages, very few attempts have been made to apply ATR-FTIR

spectroscopic imaging to the study of live cells, which is precisely the aim of this project.

1.1 Objectives

The specific objectives of this project are:

- Develop a reliable methodology for micro ATR-FTIR spectroscopic imaging of live cells. The main challenge associated with ATR-FTIR spectroscopic imaging is that the sample must be in direct contact with the ATR crystal surface. This means in practice that a reproducible method for culturing adherent cells directly on the ATR crystal surface for long periods of time will need to be established.

- Assess the ability of ATR-FTIR spectroscopic imaging to directly visualise the distribution of a drug within a living cell. As spectroscopic imaging can provide chemical information, exogenous molecules, such as drugs, could in principle be detected if the instrument is sensitive enough. This has so far not been achieved in transmission mode FTIR spectroscopic imaging experiments. If direct drug detection is possible then subcellular drug localisation, biochemical changes within the cell, and phenotypic information could be probed simultaneously in future experiments.

- To use micro ATR-FTIR spectroscopic imaging combined with the recently developed analysis technique disrelation mapping to investigate the extent to which molecular states of water can be detected within living cells. This so far has not been possible with FTIR spectroscopy, due to the difficulty of obtaining high quality spectra in the OH stretching region of the infrared spectrum.

2 Literature Review

The primary motivation behind this thesis is to apply FTIR spectroscopic imaging to studies involving live cells. This chapter aims to summarise the key topics that are relevant to the work undertaken.

Section 2.1 to 2.2 will briefly cover the elementary basics of a cell's structure and discuss other label-free methods to study cells. Section 2.3 to 2.8 will include the theoretical background and instrumentation of FTIR spectroscopic imaging. It will also cover some of the common ways to analyse spectroscopic imaging datasets and the practical computation behind 2D correlation analysis. Section 2.9 onward will summarise the current challenges and progress in applying FTIR spectroscopy to the study of live cells and then briefly Raman spectroscopy.

2.1 Cell Architecture

A cell is the smallest organised unit of molecules considered to be alive and was not discovered until sufficiently high-resolution microscopes became available (Alberts et al., 2002, chapter 9). It then became apparent that animal and plant tissue was composed of aggregates of smaller units. The idea that cells are the basic building block of living organisms is one of the tenants of cell theory, which was first proposed by Schleiden and Schwann in the 1800s (Mazzarello, 1999).

The use of cells as model systems was not possible until the development of cell culture methods, allowing various types of animal cells to be grown, maintained outside the body, and studied in isolation (Alberts et al., 2002, chapter 8). The first human cell line that was successfully extracted and cultured was the HeLa cell line, which originated from a cervical blastoma (Taylor, 2014). Cell based assays are now extensively used in a variety of scientific disciplines.

Although cells are simple in a biological context, they are still complex chemical systems. To maintain its chemical environment, a semi-permeable phospholipid membrane, known as the cell membrane, encloses the intracellular contents. Although the shape of cells can vary, their size is limited by maintaining optimal diffusion rates. The cell is further compartmentalised by phospholipid membranes into

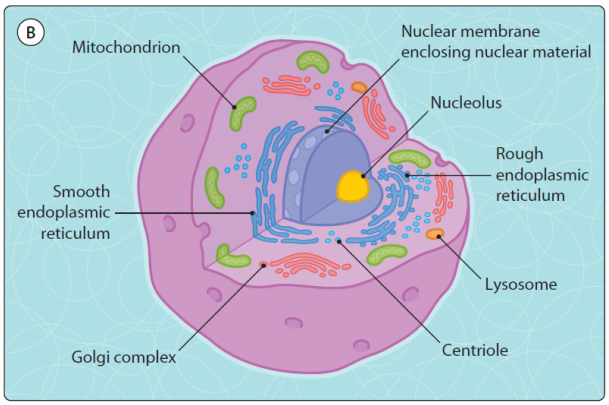


Figure 2.1: Image illustrating the main organelles of a typical animal cell. The nucleus contains the cells DNA. The mitochondrion carries out aerobic respiration, providing energy for the cells endothermic processes. The lysosome breaks down foreign material within the cell. The centrioles are primarily used during cell mitosis. The smooth and rough endoplasmic reticulum is involved in the synthesis of proteins. The image was taken from Norman and Lodwich (2007)

.

organelles with specific functions, as illustrated in figure 2.1. The contents within the cell membrane but outside the nuclear membrane is called the cytoplasm. The contents of the nucleus, which contains the cell's DNA, is the nucleoplasm.

Cells are primarily built from the macromolecules protein, the nucleic acids DNA and RNA, polysaccharides, and lipids. These are all polymers built from a series of condensation reactions linking relevant monomers together. 26.35% of the cell's weight is accounted for by these macromolecules, as summarised in table 2.1. DNA

Table 2.1: Table illustrating the percentage mass of the main macromolecules within a cell. Information was taken from Alberts et al. (2002)

Component	percentage weight
H_2O	70.0
Protein	18.0
Small metabolites	3.0
Phospholipids	3.0
Other lipids	2.0
Polysaccharides	2.0
RNA	1.1
inorganic ions	1.0
DNA	0.25

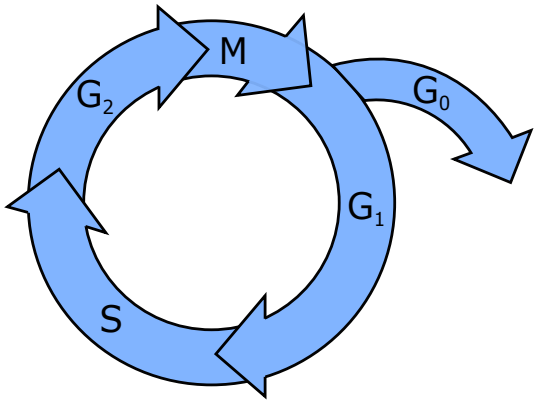


Figure 2.2: Illustration of the cell cycle phases. G_0: the cell is not participating in the cell cycle. G_1: RNA and proteins essential for the phase S are produced. S: DNA is replicated. G_2: the cell prepares for mitosis. M: cell undergoes mitosis and splits into 2 daughter cells.

contains all of the information needed to make a copy of the cell's proteins encoded in genes. RNA is involved in gene expression to synthesise proteins. Proteins themselves are the most active of the macromolecules and account for most of the dry weight of cells. They are involved in reaction catalysis of most of the cell's metabolic processes, providing structural rigidity, and generating mechanical force. Water also has many functions within the cell and accounts for 70% of its weight. It is the medium within which the cell's metabolic reactions take place and is itself a metabolite in many metabolic processes.

The primary task of a cell other than maintaining its structure is to replicate itself. It does this in a process known as a cell cycle, where one parent cell synthesises the material required for a second cell and splits into two daughter cells by mitosis (Alberts et al., 2002, Chapter 17). This is elaborated on in figure 2.2. Most cells will not do this indefinitely and there is a finite number of times they will divide. They then terminate the cell cycle permanently (Holman et al., 2000b). Immortalised cells are an important exception to this, and will divide indefinitely. Notable examples are embryonic cells, which are naturally immortal, and cancer cells, which have in someway evaded the normal cell regulation to stop dividing (Taylor, 2014, chapter 3).

2.2 Label-Free Imaging

For a microscopy technique to effectively visualise a sample of interest, sufficient image contrast must be generated. In visible microscopy, image contrast manifests from differences in colour and transmittance across the sample (Stephens and Allan,

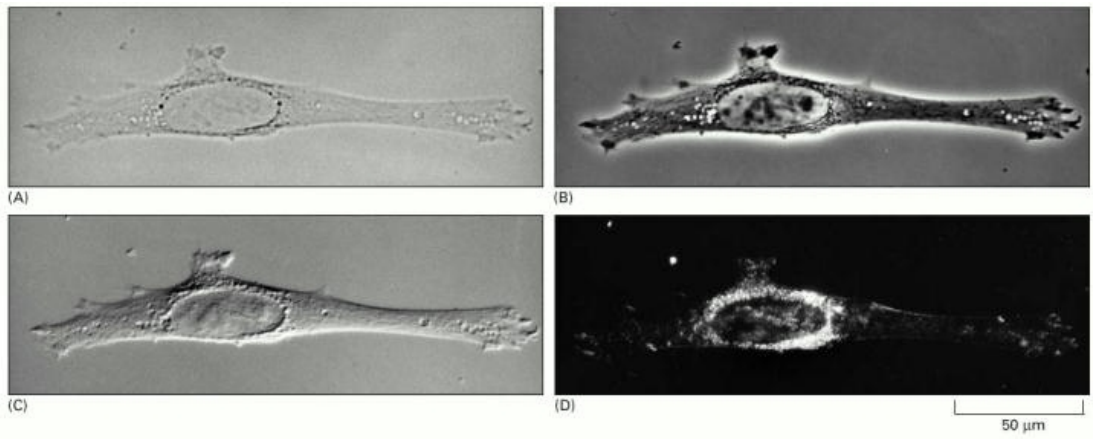


Figure 2.3: Image taken from Alberts et al. (2002) illustrating different phase contrast methods. Four images are shown of the same fibroblast cell in culture. The images were taken using: (A) Bright-field microscopy, (B) Phase-contrast microscopy, (C) DIC microscopy, (D) Dark-field microscopy

2003). Unfortunately, most cells or tissue samples are both colourless and translucent, making them hard to visualise using traditional bright-field transmission microscopy(Marquet et al., 2005). This was the impetus to develop staining techniques to improve image contrast (Alberts et al., 2002, chapter 9). These are heavily used in fields such as histopathology, where tissue samples are microscopically examined for signs of disease such as cancer(Walsh et al., 2012). Fluorescence microscopy also avoids this problem as the only recorded visible light is from the probe itself. Label-free optical methods of studying cells rely on other physical properties of the cell to generate image contrast. These can be grouped into white light, nonlinear, linear, and nonlinear-spectroscopic methods (Pavillon et al., 2014). These techniques have been summarised in table 7.1.

White light methods tend to exploit density and refractive index heterogeneity within the cell (Molder et al., 2008). When light passes through a living cell, it is retarded differently depending on thickness, density, and refractive index. Phase contrast methods convert this phase difference into an intensity difference (Majeed et al., 2015), as illustrated in figure 2.3. Modern techniques can also provide quantitative information about the phase difference and therefore the optical thickness of a sample. There are now several variations of quantitative phase microscopy based on interferometry or holographic techniques which can be used for cell-based phenotype studies (Marquet et al., 2014).

Both nonlinear and nonlinear-spectroscopic methods became possible through the development of high-power pulsed laser sources, which are required to generate nonlinear optical responses (Pavillon et al., 2014). Microscopy based on second and third

harmonic generation uses the sample as a nonlinear scattering medium in which two or three photons are up-converted into one photon, which is half or a third of the wavelength, respectively. They produce background-free images and have an intrinsic sectioning ability, because the nonlinear optical process will only occur with a significant frequency where there is a sufficiently high photon density (Mouras et al., 2013). The optical sectioning ability of these techniques is dependent on the numerical aperture of the optical system and the brilliance of the light source, which influence the focal volume within the sample with a sufficient photon density. For second and third harmonic generation to occur, the sample also needs to fulfil specific symmetry requirements. Second harmonic generation requires non-centrosymmetric materials, so only certain materials such as collagen and microtubules can be visualised within cells (Mertz, 2004). Third harmonic generation generally requires a change in refractive index and as such occurs at interfaces (Weigelin et al., 2016).

Nonlinear-spectroscopic techniques are also based on nonlinear scattering phenomenon. The most widely used are coherent anti-Stokes Raman spectroscopy (CARS) and stimulated Raman scattering (SRS), which are coherent Raman scattering methods. These techniques can produce strong signals compared to spontaneous Raman, allowing rapid imaging of biological samples, with video-rate imaging possible (Evans et al., 2005). These techniques are used most effectively when the spectroscopic band of interest is already known. These techniques can also suffer from background effects such as nonresonant background signal and self-phase modulation (Mouras et al., 2013). If the whole vibrational spectrum is desired, then linear spectroscopic imaging methods based on spontaneous Raman or infrared spectroscopy are more suitable techniques.

2.3 FTIR Theory

To describe the theory behind FTIR spectroscopy one must use time dependent quantum mechanics. This has been done rigorously elsewhere (Atkins and Friedman, 2011; Fayer, 2001). This section will only give a summary and will then move on to the essentials of FTIR instrumentation and spectroscopic imaging.

2.3.1 Molecular Vibrations

To simplify the quantum mechanical treatment of molecular vibrations, we can consider the overall vibrational motion of a molecule to be the superposition of independent normal vibrational modes. A molecule with N atoms will have $3N-6$ vibrational modes (unless the molecule is linear, where the formula becomes $3N-5$).

The simplest model for a vibrating molecule is a diatomic molecule that behaves as a harmonic oscillator, which only has one vibrational mode. The relevant eigenvalue problem to solve is

$$H|\psi\rangle = E|\psi\rangle \tag{2.1}$$

where H is the Hamiltonian operator, $|\psi\rangle$ is the wavefunction that describes the motion of the harmonic oscillator, and E is the energy eigenvalue. We can consider this wavefunction to be a superposition of eigenfunctions, or vibrational energy states, such that

$$|\psi\rangle = \sum_{\nu} C_\nu |\nu\rangle \tag{2.2}$$

where ν is the vibrational quantum number, C_ν is the probability amplitude of observing the harmonic oscillator in a state $|\nu\rangle$. The probability of observing the harmonic oscillator in a particular state is calculated by taking the product of the eigenfunction's probability amplitude and its complex conjugate

$$\langle\nu|C_\nu^* C_\nu|\nu\rangle = C_\nu^* C_\nu \langle\nu|\nu\rangle = C_\nu^* C_\nu. \tag{2.3}$$

The energy eigenvalues follow the general formula

$$E = \hbar\omega\left(\nu + \frac{1}{2}\right) \tag{2.4}$$

where ω is angular frequency of the vibration. Equation 2.4 illustrates two important features of the quantum harmonic oscillator, namely that the oscillator cannot have zero energy and that there are discrete vibrational energy levels. The graphical solution of the harmonic oscillator eigenfunctions is shown in figure 2.4, which are time independent solutions. This means, without an external perturbation, the probability of a vibrational mode being in a particular energy state will remain constant.

2.3.2 Vibrational Transitions

In infrared spectroscopy, we perturb molecules with light to couple vibrational energy states and induce transitions. At room temperature, most molecules are in the ground energy state $|0\rangle$. The fundamental transition from $|0\rangle$ to $|1\rangle$ is the most common transition seen in an infrared spectroscopy experiment. Light with the correct energy to induce fundamental vibrational transitions for most molecules is found in the mid-infrared region. For low electric field strength, we can use first order time-dependent perturbation theory to calculate the fundamental transition

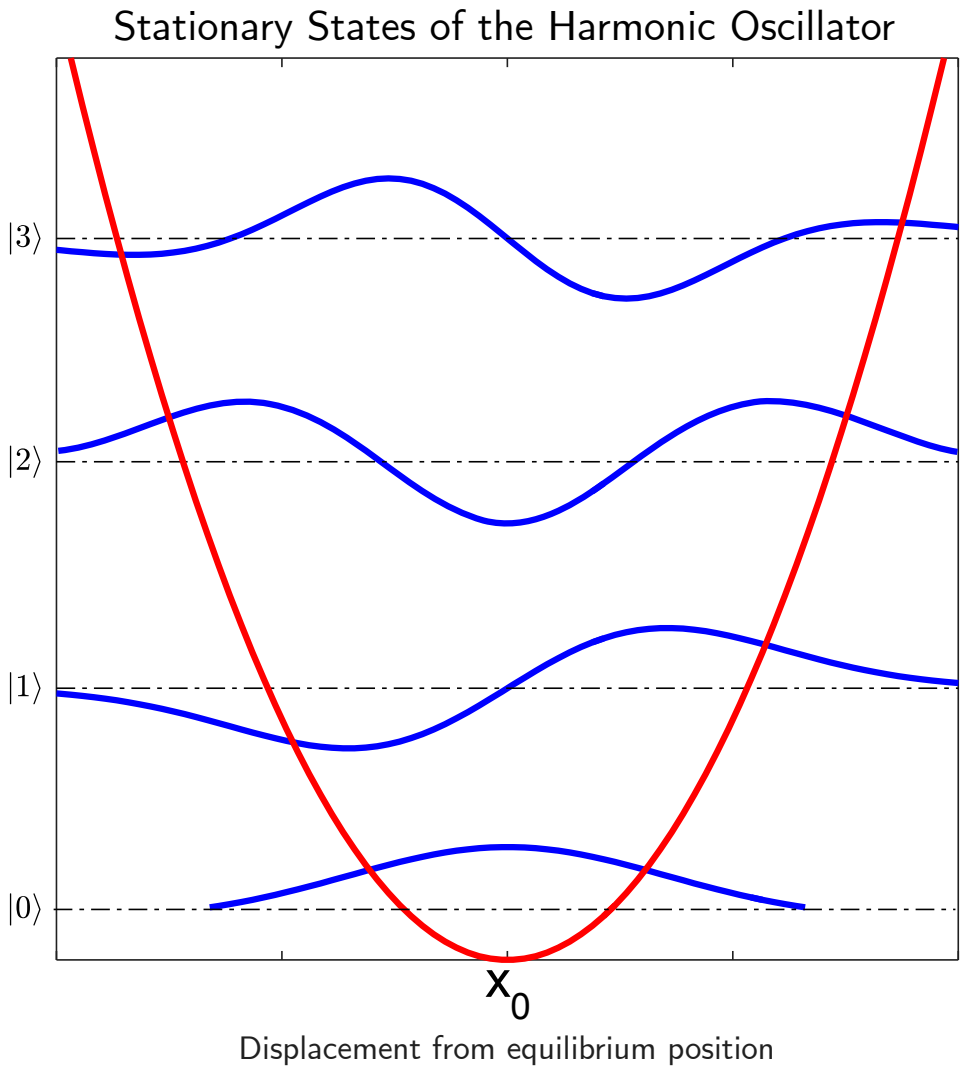


Figure 2.4: Illustration of the eigenfunctions corresponding to the vibrational energy states. The graph depicts the probability amplitude as a function of displacement from the equilibrium position. The red line shows a classical harmonic oscillator equation. The blue lines show the quantum oscillator eigenfunctions of the first three energy levels

probability as the harmonic oscillator is perturbed by an oscillating electric field. We can consider the Hamiltonian as

$$H(t) = H + H'(t) \tag{2.5}$$

where H is the time independent zeroth order Hamiltonian that describes the harmonic oscillator and $H'(t)$ describes the time-dependant perturbation of the system. The change in the probability amplitude, C_1, of observing the harmonic oscillator

in excited state $|1\rangle$ is given by

$$\frac{dC_1}{dt} = -\frac{i}{\hbar}\langle 1|H'|0\rangle. \tag{2.6}$$

When the energy of the light matches the transition energy between two energy states the resonance condition is met and the probability of observing the harmonic oscillator in the excited state $|1\rangle$ is

$$C_1^* C_1 = \frac{2\pi}{3\hbar^2}|\mu_{10}|^2 \rho(\nu_{10})t \tag{2.7}$$

where μ_{10} is the transition dipole moment operator. This shows us that the probability of observing the harmonic oscillator in state $|1\rangle$ varies linearly with time and the radiation density of light. It also shows us that the transition rate is proportional to the modulus squared of the transition dipole operator. We can use the transition dipole moment to establish how likely a transition is to occur and derive the gross selection rule for infrared spectroscopy. We can expand the dipole moment in terms of displacement of the nuclei from their equilibrium position

$$\mu = \mu_0 + \left(\frac{d\mu}{dx}\right)_0 x + \frac{1}{2}\left(\frac{d^2\mu}{dx^2}\right)_0 x^2 + \dots \tag{2.8}$$

This means that the transition dipole will take the form

$$\langle \nu'|\mu|\nu\rangle = \mu_0\langle \nu'|\nu\rangle + \left(\frac{d\mu}{dx}\right)_0 \langle \nu'|x|\nu\rangle + \frac{1}{2}\left(\frac{d^2\mu}{dx^2}\right)_0 \langle \nu'|x^2|\nu\rangle + \dots \tag{2.9}$$

We can see from equation 2.9 that, unless the dipole moment varies with displacement, i.e. vibration, then all the terms become zero and the transition is said to be forbidden. A further specific selection rule for infrared spectroscopy is that the transition dipole moment will equal zero unless the vibrational quantum number changes by one during the transition. This rule arises from properties of the eigenfunctions of the harmonic oscillator, which are Hermite polynomials. In reality, vibrations are anharmonic and this means forbidden transitions under the harmonic approximation become weakly allowed. Two common types of forbidden transitions are overtone and combination transitions. Overtones are transitions where the change in vibrational quantum number is greater than one. Combination bands occur when multiple vibrational modes are excited simultaneously through vibrational coupling.

2.4 Mid-Infrared Spectroscopy Instrumentation

The features common to all infrared spectrometers are a source of infrared radiation, a method of exposing a sample to infrared light, and a detector to record infrared light intensity. Most modern bench-top infrared spectrometers generally use a silicon carbide globar to generate infrared light, and either a deuterated triglycine sulfate (DTGS) or a mercury cadmium telluride (MCT) detector to measure the infrared light intensity (Buijs, 2006; Theocharous and Birch, 2006).

Globars are an incandescent light source that emits light as a result of being heated. Silicon carbide rods can be heated to 1800K by passing electrical current through it, and can be heated to 1400K for years without degradation (Buijs, 2006). Synchrotron facilities can also be used to generate infrared light and benefit from a higher brilliance than can be achieved with incandescent sources. More recently other types of infrared sources have emerged such as supercontinuum lasers, nonlinear optical sources, and quantum cascade lasers. These types of sources also benefit from high brilliance, but currently none of these systems can span the whole mid infrared region.

DTGS are thermal detectors that use the pyroelectric property of deuterated triglycine sulfate crystals (Theocharous and Birch, 2006). When heated these crystals generate charge, creating a voltage across the crystal. This charge is quickly neutralised, as the charge is lost to the detector circuit. By modulating the incident radiation on the crystal, a series of electrical current pulses flow through the detector circuit. MCT detectors exploit the property of photoconductivity (Theocharous and Birch, 2006). Mercury cadmium telluride is a low energy band gap semiconductor, that acts as a photoresistor in the detector circuit. Its resistance drops when exposed to infrared light, because infrared light induces electronic transitions between the valence band and the conducting band of MCT. This means that the electrical conductivity of the detector increases in the presence of infrared light. MCT detectors are more sensitive than DTGS dectectors but require cooling to 77 K, which is typically done using liquid nitrogen. DTGS detectors can be thermo-electrically cooled.

Both of these detectors can only detect the overall brightness from the radiation it is measuring. If the incident radiation at the detector is polychromatic, as is the case for incandescent sources, the power spectrum across the frequency range cannot be directly detected. The initial solution to this problem was to use a monochromator to sequentially select and direct small frequency bands from the broadband source to the detector. A grating dispersed the light and a slit selected the desired frequency band. The size of the slit defined the spectral resolution. The power spectrum is

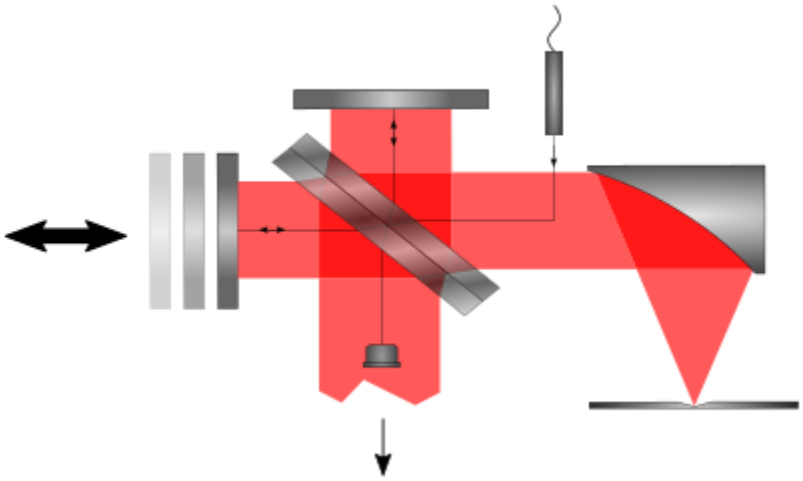


Figure 2.5: Schematic of a Michelson interferometer adapted from Jackson (2006). Infrared light passes through a beam splitter, where half of the light is sent to a fixed mirror and rest to a moving mirror. The two beams of polychromatic light are then recombined and superimpose.

recorded by scanning the grating through a range of angles corresponding to the desired frequency range. This is a form of discrete frequency spectroscopy.

In the 1960s, infrared spectroscopy using optical interferometry superseded grating based methods. Interferometry based methods exploit the property that the interferometric autocorrelation of an electromagnetic field is related to its power spectrum by the Fourier transform (Cohen, 1998), as illustrated in figure 2.6. For this reason, interferometry based infrared spectroscopy is known as Fourier transform infrared spectroscopy (FTIR). Most FTIR spectrometers in use today use a form of Michelson interferometer, as illustrated in figure 2.5 (Jackson, 2006). The infrared beam is split into two arms where the optical path length of one arm is kept fixed, while the other is varied using a movable mirror. This difference in the optical path length (OPD) is also known as the optical retardation . The ensemble of frequencies composing the infrared light undergoes constructive and destructive interference when recombined depending on the OPD. A digital representation of the infrared beam's interferometric autocorrelation, or interferogram, is generated by recording the intensity at a range of evenly spaced OPD values. The power spectrum as a function of wavenumber can then be calculated by taking the Fourier transform of the interferogram. The spectral resolution is defined by the maximum OPD capable by the interferometer. The short wavelength limit is determined by the sampling rate. This is a consequence of the Nyquist theorem, which states that a continuous sinusoid can only be restored from a discrete representation if the sampling frequency is at least twice the frequency of the original sinusoid.

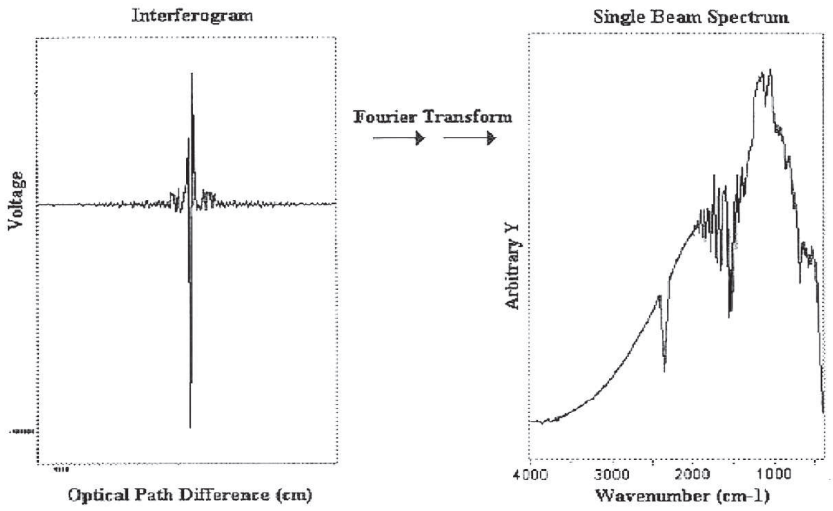


Figure 2.6: Illustration of an interferogram and its corresponding spectrum (adapted from Atkins and de Paula (2002)). The two are related by the Fourier transform.

In practice, the spectrometer uses the interference pattern from a 633 nm HeNe laser to track its OPD. As the HeNe laser produces monochromatic light its interference pattern will be the autocorrelation of two identical cosine functions, which will also be a cosine function. Specifically, the interference pattern will have the form

$$I(x) = \cos\left(\frac{x2\pi}{\lambda}\right) = \cos\left(x\tilde{\nu}2\pi\right) \tag{2.10}$$

where x is the OPD. λ and $\tilde{\nu}$ correspond to the wavelength and wavenumber of the HeNe laser, respectively. The signal detected from the HeNe laser's interferogram will be zero every time that

$$x = \frac{\lambda}{4}\left(2n - 1\right) \tag{2.11}$$

where $n \in \mathbb{Z}$. This will occur twice as the OPD changes by a distance of λ. This event is known as a zero crossing, which is used to trigger an analog-to-digital converter to digitise the IR signal. The Δx between two zero crossings is 316.5 nm. This means the highest frequency that can be digitally recorded by the spectrometer is the frequency of the HeNe beam. For infrared experiments it is not necessary to record frequencies this high so the interferogram is often digitised every 2 or 3 zero crossings.

FTIR spectrometers have a higher throughput, faster collection times, and better wavelength accuracy compared to dispersive spectrometers. These are known as the Fellgett, Jacquinot, and Connes advantages (Gronholtz and Herres, 1984).

2.5 Sampling Modes

2.5.1 Transmission

To measure a sample's infrared absorption spectrum the infrared light intensity is measured as a function of wavelength with and without the sample present. The sampling mode is the method by which infrared light interacts with the sample. Matter can absorb light during total internal reflection (TIR), external reflection, transmission, and transflection, which defines the possible sampling modes.

In transmission mode we measure the sample's transmittance across the mid-infrared frequency range. The sample is simply placed in the infrared beam path of the instrument. A transmittance spectrum $T(\lambda)$ is calculated by dividing the sample spectrum by the reference spectrum recorded in the sample's absence.

$$T(\lambda) = \frac{I}{I_0} \tag{2.12}$$

Another common unit is absorbance, which is calculated by taking the negative log of the transmittance

$$A(\lambda) = -log\left(\frac{I}{I_0}\right). \tag{2.13}$$

Absorbance has the advantage of being directly proportional to concentration, as described by the Beer-Lambert law

$$A(\lambda) = \epsilon(\lambda)cl \tag{2.14}$$

Where l is the path length, $\epsilon(\lambda)$ is the molar absorptivity coefficient as a function of wavelength, and c is the concentration of the sample. In transmission mode the path length is determined by the thickness of the sample. The highest usable path length in a transmission mode experiment is limited by the sample's concentration and molar absorptivity.

In practice light is attenuated by a combination of absorption, scattering, and reflection at the sample's surface. Scattering generally manifests as a baseline distortion in the infrared spectrum, but in some cases, such as resonant Mie scattering (Bambery et al., 2012), the effect on the spectra is more complicated.

2.5.2 Attenuated Total Reflection

Total internal reflection requires an interface between two media with different refractive indexes. The optically denser medium is referred to as the internal reflection

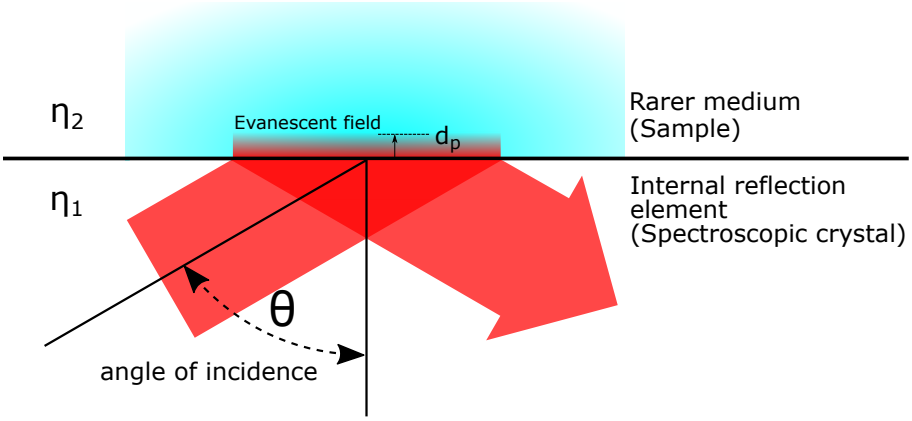


Figure 2.7: Illustration of attenuated total reflection

element (IRE). When light travelling through the IRE meets an interface with an optically rarer medium at an angle above the critical angle (as defined by Snell's law), total internal reflection occurs. At the interface, a non-propagating electric field, known as an evernescent field, exponentially decays with increasing distance into the rarer medium. The depth of penetration d_p is the distance the field travels into the rarer medium before it has decayed to e^{-1} of the initial field strength, and this is calculated from the following equation

$$d_p = \frac{\lambda}{2\pi n_1 \left(\sin^2\theta - n_{21}^2\right)^{0.5}} \tag{2.15}$$

where $n_{21} = n_2/n_1$. n_1 is the refractive index of the IRE, n_2 is the refractive index of the sample, and θ is the angle of incidence of the infrared light relative to the normal (Mirabella, 2006). If the rarer medium is absorptive in the infrared region then energy is transferred to the rarer medium and this is the basis of the attenuated total internal reflection (ATR) spectroscopy, as illustrated in figure 2.7. In ATR spectroscopy the sample is the rarer medium which is placed in contact with the internal reflection element, which is usually a high refractive index crystal. The most commonly used crystals are summarised in table 2.2. In contrast with transmission imaging, the path length is not dependent on the thickness of the sample. As the penetration depth is dependent on wavelength, it varies across the mid-infrared region. This distorts the relative absorbance of spectral bands compared to a transmission experiment. The depth of penetration also depends on the angle of the incident light. This means the sample can be probed at different depths, opening up the possibility of using ATR spectroscopic imaging for depth profiling (Wrobel et al., 2015).

Table 2.2: ATR crystal properties (Pike Technologies, 2011). n_1 = refractive index of crystal; LWL = long wavelength limit. d_p = depth of penetration at 1000 cm^{-1}.

Material	n_1	LWL (cm^{-1})	d_p (µm)	pH Range	Hardness (kg mm^{-2})
Diamond/ZnSe	2.4	525	2	1-14	5,700
Germanium	4	780	0.66	1-14	550
Silicon	3.4	1500	0.85	1-12	1150
ZnS	2.2	850	3.86	5-9	240
ZnSe	2.4	525	2	5-9	120

To compare the absorbance from ATR mode to transmission mode one can calculate the effective path length of the evanescent field. This is defined as the equivalent path length in a transmission measurement that would lead to the same absorption. The effective thickness, first proposed by Harrick (Averett et al., 2008), depends on the polarisation and the standard equations are

$$d_{e\perp} = \frac{n_{21}\lambda_0 \cos\theta}{n_1\pi(1-n_{21}^2)(\sin^2\theta - n_{21}^2)^{0.5}} \tag{2.16}$$

for s polarised light and

$$d_{e\parallel} = \frac{n_{21}\lambda_0 cos\theta(\sin^2\theta - n_{21}^2)}{n_1\pi(1-n_{21}^2)[(1+n_{21}^2)\sin^2\theta - n_{21}^2](\sin^2\theta - n_{21}^2)^{0.5}}. \tag{2.17}$$

for p polarised light. In unpolarised light there is an equal amount of s and p polarised light, so the average of the two equations is taken. These equations are approximations which do not work for strongly absorbing samples or account for anomalous dispersion.

2.5.3 FTIR Spectroscopic Imaging

In single element FTIR spectroscopy, one spectrum is collected representing the average infrared absorption from the sample cross section exposed to the infrared beam. If the sample is homogeneous, then this spectrum is representative of the entire sample. If however the sample is heterogeneous, then this spectrum gives no information about the chemical distribution across the sample. Using a single element detector, the only way to discern the chemical distribution within a sample would be to sequentially scan different subsets of the sample, which is known as mapping. With the development of focal plane array (FPA) detectors, thousands

of spatially resolved spectra can be recorded simultaneously, which is known as spectroscopic imaging. If high resolution and a large field of view are both required, such as imaging of large sections of tissue samples, then a hybrid approach of imaging with mapping can be employed.

As an optical technique, infrared spectroscopy can also be combined with magnifying optics to probe the chemical distribution of smaller samples areas. Without any magnification the pixel resolution would be defined by the pixel's physical area, which is around 40x40 µm in an FPA detector. In transmission mode, the setup is very similar to visible optical microscopy. The key difference is that reflective optics are used instead of lenses. This is to avoid the optical aberration, which would inevitably occur using refractive optics over such a large wavelength range (Sommer, 2006).

The resolving power of a traditional optical microscope is fundamentally limited by diffraction. Rather than focusing to a point, imaging forming rays from a sample form a spherical interference pattern known as an Airy disk. The resolving power of a microscope can ultimately be viewed as the smallest distance for which two Airy disks can be resolved. A common criterion for this least resolvable distance (LRD) is the Rayleigh criterion

$$LRD = \frac{0.61\lambda}{n \sin \theta}. \tag{2.18}$$

The numerical aperture $n \sin \theta$ is the ability of an objective to gather light and θ represents the largest angle from which the objective can accept light. As LRD is a function of wavelength, infrared in transmission mode cannot achieve the same resolution as visible microscopy, fluorescence, or Raman due to the larger wavelength of infrared light. The theoretical resolution limit in micro-transmission FTIR is between 13 µm and 2.5 µm across the mid infrared region with a 0.6 NA objective.

ATR-FTIR spectroscopic imaging can achieve higher spatial resolution than transmission. By acting as an immersion lens, the high refractive index of the ATR crystal increases the numerical aperture and thus decreases the LRD. For example, if germanium is used, a spatial resolution four times greater than possible in air can be achieved, as germanium's refractive index is 4 (Chan et al., 2005; Kazarian and Chan, 2010).

The spectral resolution can be increased beyond this using near-field techniques that are not subject to the diffraction limit, making nanoscale resolution possible. These include Infrared scattering-type scanning near-field optical microscopy (s-SNOM) (Vobornik et al., 2005), infrared atomic force microscopy (AFM-IR) (Dazzi et al., 2012), and tip enhanced Raman spectroscopy (TERS) (Chan and Kazarian, 2011). Generally, these techniques involve an AFM tip and use either local electro-

magnetic field enhancement or use the tip as the detector itself. In either case, the limit of detection is defined by the size of the near field probe, not the wavelength of light. All of these techniques have achieved lateral resolution under 100 nm but measurement times are significantly slower than conventional spectroscopic imaging. The use of a near field probe means imaging is currently not possible, and recording spectroscopic maps with such high resolution will mean a high number of scans for even a small sample area. In the case of ARM-IR and s-SNOM a discrete source of infrared light is used, so in addition to mapping these techniques must scan through the desired infrared frequencies separately.

2.6 Univariate Spectral Analysis

The raw data from an FPA detector is a rank three tensor where the first two dimensions are spatial, referring to the x and y axis of the detector array grid, and the third dimension is the spectral dimension, as illustrated in figure 2.8. One of the most common ways to analyse this data is to generate a chemical map. The simplest way to do this is simply to choose one wavelength and plot the value as a function of the FPA pixels. A more robust alternative is to integrate a band of interest for

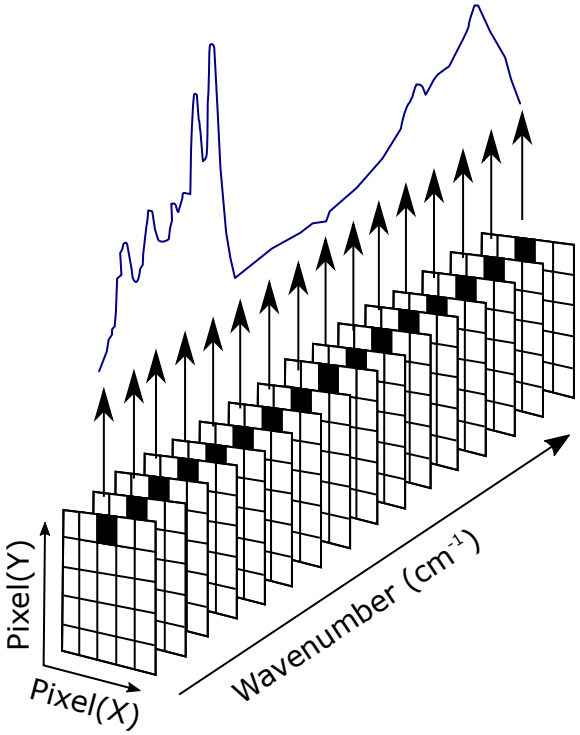


Figure 2.8: Illustration of the structure of a spectroscopic imaging dataset. (Adapted from Kidder et al. (2006))

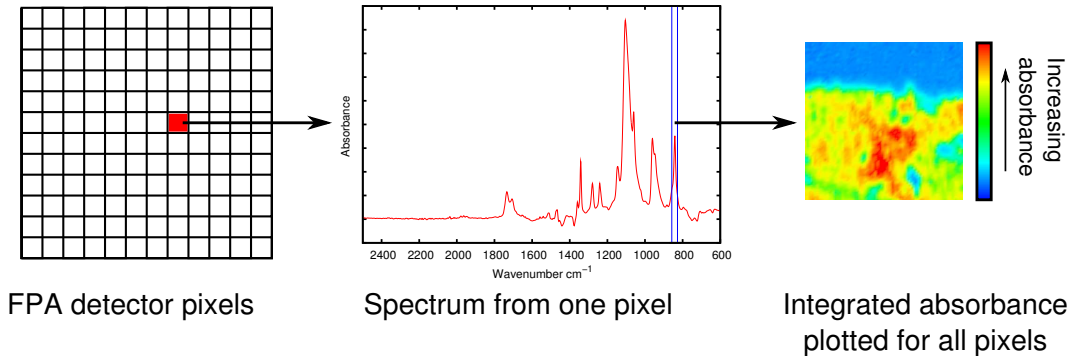


Figure 2.9: Illustration of the method for generating an integrated absorbance image using method A integration. The spectral range of interest is integrated to get the integrated absorbance. This is carried for the spectrum recorded by each pixel. The integrated absorbance is then plotted as a function of pixel position.

each of the spectra, as shown in figure 2.9. This can be done for multiple peaks from the same dataset to examine how the distribution of different chemical groups vary relative to each other. Peak intensity is not the only method of generating contrast in the chemical map; for instance, peak shifting can also be used (Chan et al., 2007).

2.7 Multivariate Spectral Analysis

Multivariate analysis is the application of multivariate statistics to a dataset. The goal is the simultaneous analysis of more than one outcome variable. Most of these techniques are intertwined with linear algebra and thus use matrices. This means the raw spectroscopic imaging dataset must be reshaped from three dimensions to two. In this form, the rows of a matrix are referred to as samples, which correspond to the spectrum recorded from each pixel. Each wavenumber in the digitised spectrum is a column, and is referred to as a feature.

Multivariate curve resolution, classical least squares, and principal component analysis all use the same basic linear algebra equation illustrated in figure 2.10, but the interpretation and method of solving the equation is different. In classical least squares, A and B are concentration and pure spectra, respectively. In this instance, we know X and A so we can solve the equation analytically. Multivariate curve resolution has the same interpretation, but we do not know what the pure spectral components are ahead of time (Koch et al., 2014). For principal component analysis, A and B are the scores and loadings respectively, and can be solved in a number of ways such as the NIPALS (Geladi and Kowalski, 1986) algorithm or the

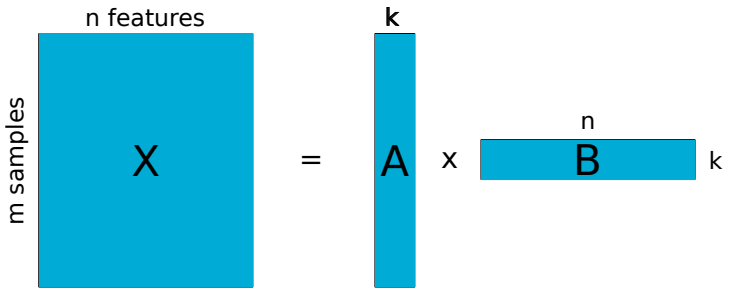


Figure 2.10: Illustration of the linear algebra equation common to classical least squares, principal component analysis, and multivariate curve resolution.

eigenvalue-eigenvector approach.

In clustering methods, each spectrum is viewed as a point in an n-dimensional space, where n is the number of spectral variables. The goal is to find spectra which are close together by whichever distance metric is chosen. Two common approaches to clustering are hierarchical cluster analysis (HCA) and k-means clustering. Hierarchical clustering is an iterative process where the two most similar samples are found and then averaged. This continues until all of the samples have been merged. HCA can provide information about how many, if any, natural clusters there are within the data. In k-means clustering the number of clusters is predefined and the goal of the algorithm is to optimise the position of the cluster centroids. This is defined as the centroid position that provides the least overall difference between the samples and their assigned cluster.

2.8 Generalised 2D Correlation Spectroscopy

The theory of 2D correlation spectroscopy has been extensively covered by Noda and Ozaki (2005). This section covers the theory necessary to calculate 2D correlation spectra on discrete data.

The dynamic spectrum $\tilde{y}(\nu, t)$ of a system is defined as the spectral intensity variation induced by an external perturbation. Often the perturbation is time, but many other perturbations can be used. If the system has very few spectral bands then changes in intensity or band shifts are obvious by visual inspection. However, if the dynamic spectrum is more complicated, it can be difficult to analyse all of the spectral variations.

2D correlation spectroscopy emerged as an analytical technique to help deal with

this problem. It was first developed by Isao Noda for sinusoidally varying dynamic systems (Noda, 1989), where the function describing the perturbation has an analytical solution. Later, generalised 2D correlation spectroscopy was developed, which can be used with any spectroscopy technique, or combination of techniques (Noda, 1993). This used the Fourier transform to approximate the perturbation function. Generalised 2D correlation spectroscopy is a quantitative measure of how spectral variables vary within the perturbation observation window. For two spectral variables, the correlation spectrum can be expressed as

$$X(\nu_1, \nu_2) = \langle \tilde{y}(\nu_1, t), \tilde{y}(\nu_2, t) \rangle \tag{2.19}$$

which represents the spectral correlation intensity between the variation of the two spectral variables. This is done independently between all possible pairs of spectral variables within a dataset, which gives the correlation its characteristic square shape. The correlation function is a complex number function

$$X(\nu_1, \nu_2) = \Phi(\nu_1, \nu_2) + i\Psi(\nu_1, \nu_2) \tag{2.20}$$

where Φ is the synchronous spectrum and Ψ is the asynchronous spectrum. Originally the rigorous calculation of the generalised 2D correlation spectrum required the use of the Fourier transform (Noda, 1993), but methods have since been developed that avoid the Fourier transform (Noda, 2000). The synchronous spectrum can be computed as

$$\Phi(\nu_1, \nu_2) = \frac{1}{t_1 - t_0} \int_{t_0}^{t_1} \tilde{y}(\nu_1, t)\tilde{y}(\nu_2, t)dt \tag{2.21}$$

which can be interpreted as the perturbation duration averaged spectral intensity variation of the spectral variables ν_1 and ν_2. As recorded dynamic spectra are discrete rather than continuous, the integral is replaced by a summation. Within this framework the dynamic spectrum becomes a column vector

$$\tilde{\mathbf{y}}(\nu_1) = \begin{bmatrix} \tilde{y}(\nu_1, t_1) \\ \tilde{y}(\nu_1, t_2) \\ \vdots \\ \tilde{y}(\nu_1, t_m) \end{bmatrix} \tag{2.22}$$

and the synchronous spectrum can be calculated with the following equation

$$\Phi(\nu_1, \nu_2) = \frac{1}{m-1} \sum_{j=1}^{m} \tilde{\mathbf{y}}_j(\nu_1) \cdot \tilde{\mathbf{y}}_j(\nu_2). \tag{2.23}$$

where $\tilde{\mathbf{y}}_j(\nu) = \tilde{y}(\nu, t_j)$. The asynchronous spectrum can also be calculated separately using the Hilbert transform. The orthogonal spectrum $\tilde{z}(\nu, t)$ is defined as a the Hilbert transform of the dynamic spectrum.

$$\tilde{z}(\nu, t) = \frac{1}{\pi} \int_{-\inf}^{\inf} \frac{\tilde{y}(\nu, t')}{t - t'} dt'. \tag{2.24}$$

The orthogonal spectrum is a function where the phase of its Fourier components are shifted by $\pi/2$ compared to the dynamic spectrum. Once the orthogonal spectrum has been computed the equation to calculate the asynchronous intensity is simply

$$\Psi(\nu_1, \nu_2) = \frac{1}{t_1 - t_0} \int_{t_0}^{t_1} \tilde{y}(\nu_1, t) \tilde{z}(\nu_2, t) dt. \tag{2.25}$$

With a discrete dynamic spectrum the equation becomes

$$\Psi(\nu_1, \nu_2) = \frac{1}{m-1} \sum_{j=1}^{m} \tilde{\mathbf{y}}_j(\nu_1) \cdot \tilde{\mathbf{z}}_j(\nu_2). \tag{2.26}$$

$\tilde{\mathbf{z}}_j(\nu_2)$ is calculated using the Hilbert-Noda transformation (Noda and Ozaki, 2005)

$$\tilde{\mathbf{z}}_j(\nu_2, t) = \sum_{k=1}^{m} N_{jk} \cdot \tilde{\mathbf{y}}_k(\nu_2) \tag{2.27}$$

where

$$N_{jk} \begin{cases} 0 & \text{if } j = k \\ 1/\pi(k-j) & \text{otherwise.} \end{cases} \tag{2.28}$$

An approximation of the asynchronous spectrum called the disrelation spectrum is also commonly used. It can be calculated directly from the synchronous spectrum

$$\Lambda^2(\nu_1, \nu_2) = \Phi(\nu_1, \nu_1)\Phi(\nu_2, \nu_2) - \Phi^2(\nu_1, \nu_2). \tag{2.29}$$

2.9 FTIR Spectroscopy of Live Cells

The main spectroscopic features of live cells come from water and bio-macromolecules, as shown in figure 2.11. The amide bands correspond to protein backbone vibrations and the phosphate bands correspond mostly to the nucleic acids DNA and RNA. It has been shown recently that the phosphate II band at 1220 cm^{-1} is a good marker for cellular DNA, and the spectral contribution at 1120 cm^{-1} under the envelope of the phosphate I centred at 1080 cm^{-1} is the best marker for RNA (Zucchiatti et al., 2016). The C-H stretch region at around 3000 cm^{-1} is typically assigned to lipids.

Water accounts for the strongest bands seen in live cells and is typically subtracted, either by physical removal, in the case of fixation and drying, or by spectral subtraction during data processing. Spectral subtraction is often done for superficial reasons rather than being strictly necessary for spectral analysis (Chan and Kazarian, 2016), and proper subtraction of water is not straightforward (Rahmelow and Hubner, 1997).

Most FTIR spectroscopy or spectroscopic imaging measurements on cells have been done using fixed or dried cells. This is due to the technical difficulty associated with keeping cells alive and the signal to noise compromises made when doing experiments in aqueous environments. Despite these difficulties, experiments using live cells avoid the biochemical distortions associated with fixation or drying (Vaccari et al., 2012b) and are less distorted from effects such as resonant Mie scattering (Mattson et al., 2013). Another significant advantage is that the capability for

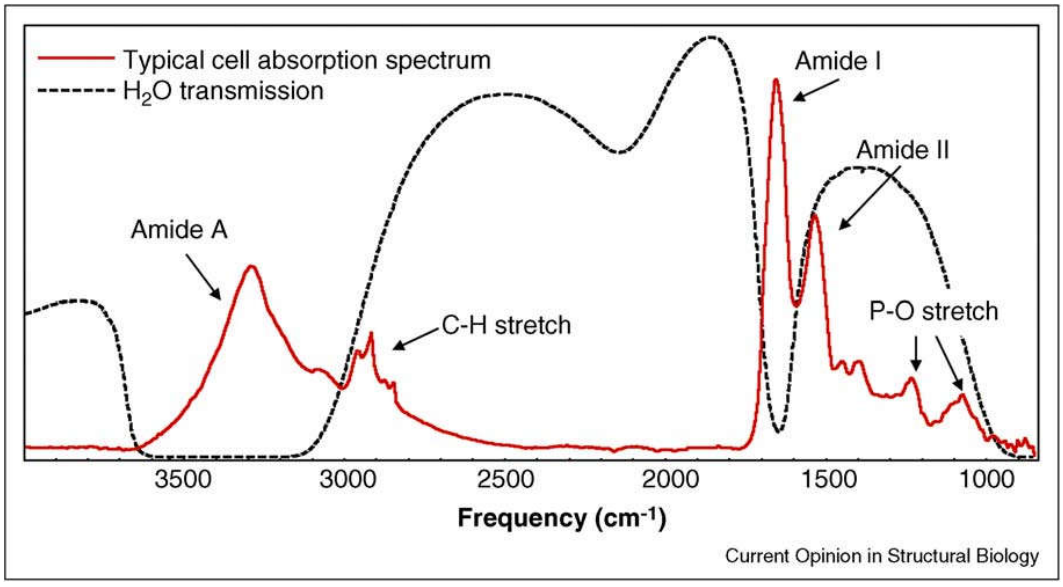


Figure 2.11: Figure taken from Miller and Dumas (2010) showing an absorbance spectrum of a fixed cell compared to the transmittance spectrum of water.

time-lapse studies greatly increases. Once the methodology for keeping cells alive during infrared measurements is established, they can be periodically scanned for the desired time course. If cells are fixed or dried then this flexibility is gone.

In the next few sections some of the challenges and the most successful applications of infrared spectroscopy to the study of live cells will be highlighted. Transmission and ATR mode will be considered separately.

2.9.1 Spatial Resolution in FTIR Microscopes

As previously mentioned in section 2.5.3, the relatively long wavelength of infrared light makes the spatial resolution requirements challenging for FTIR spectroscopic measurements. Most cell organelles are on the order of 1 µm or lower in size, which is beyond the resolution capability of transmission mode infrared spectroscopy. Often in FTIR micro-spectroscopy experiments, subcellular resolution is not required and apertures are set to get an average spectrum from a whole cell.

In FTIR spectroscopic imaging or mapping it would be desirable to resolve subcellular features, so that biochemical responses in different organelles can be distinguished. The resolution provided by FTIR spectroscopic imaging is sufficient to distinguish the nucleus from the cytoplasm. It has also been shown that the Golgi apparatus/endoplasmic reticulum can be visualised using the CH_3/CH_2 band ratio, within the CH stretching region at 2900-3000 cm^{-1}, in fixed cells (Sandt et al., 2013; Clède et al., 2014).

ATR-FTIR spectroscopic imaging enjoys better spatial resolution than found in transmission imaging, but so far has not been shown capable of resolving smaller cell features. No attempt to visualise the Golgi apparatus from the CH_3/CH_2 band ratio has been reported from ATR-FTIR spectroscopic imaging studies. However, the spectral contribution of a sub-band at 1023 cm^{-1}, underneath the phosphate I envelope, has been tentatively assigned to the endoplasmic reticulum (Kuimova et al., 2009).

In FTIR spectroscopic imaging studies the projected pixel size is often used to indicate the spatial resolution, and projected pixel sizes as low as 0.5×0.5 μm^2 have been reported (Mitri et al., 2015; Mattson et al., 2013). Unfortunately, this does not reflect the true resolving power of an instrument, although spatial oversampling can improve image quality (Reddy et al., 2013). Another important consideration for spectroscopic imaging beyond simply resolving a feature is obtaining spatially resolved spectra. As previously mentioned in section 2.5.3, the Rayleigh criterion is often used to determine the lateral resolution of a microscope. However, this criterion was originally developed for visible microscopy, where recognising small

features is the main goal. In spectroscopic imaging this distance is not sufficient to get spatially resolved spectra. Whilst two Airy disk diffraction patterns can be distinguished at the distance defined by the Rayleigh criterion, they would still have significant overlap, resulting in a significant spectral contribution from neighbouring sample material.

The USAF 1951 resolution target is often used to test the spatial resolution in microscopic systems. However, this is a highly idealised system, and was also designed to indicate spatial resolution based on the Rayleigh criterion. Generally, real samples have a much smaller contrast in refractive index and are thicker. Thus the achieved spatial resolution in a real sample is often worse (Chan et al., 2005; Kazarian and Chan, 2010). To address this problem, Chan and Kazarian (2013b) used a model sample consisting of a 6 µm laminate of polymer films. The polymers were spectrally distinct but had similar refractive indexes. With this model system the spatial resolution was found to be three times worse than seen using the USAF 1951 resolution target in the same spectral region.

2.9.2 Path Length Restrictions of Aqueous Samples

One major challenge of FTIR spectroscopic imaging of live cells is the high molar absorptivity of water. Cell cultures must be maintained in an aqueous environment, and are themselves mostly water. This places major restrictions on the path length in transmission mode experiments. This is a general problem for infrared spectroscopy of aqueous solutions. For instance, when studying proteins in aqueous solution the best signal to noise in the amide I region is achieved with a path length of 3-4 µm (Venyaminov and Prendergast, 1997) in H_2O, and 40–60 µm in D_2O. Longer path lengths are possible with the use of a brighter source, such as a quantum cascade laser. For instance, Schwaighofer et al. (2016) used a 478 µm thick PTFE spacer to measure poly-L-lysine dissolved in D_2O buffer. This indicates that H_2O solutions could be measured at path lengths above 12-16 µm with a good signal to noise using a QCL system.

The vast majority of FTIR transmission mode studies of live cells to date have been done using a synchrotron, where a path length above 12.5 µm is not feasible. This necessitates the use of microfluidics, which is an active area of research to improve the methodology of FTIR transmission mode imaging. The first IR-transparent microfluidic system applied to live cell assays was demonstrated by Vaccari et al. (2012a). An 8.5 µm thick layer XARP 3100/10 photoresist was spin coated onto a CaF_2 window, and channels were fabricated using UV lithography. The device was then thermomechanically sealed with another CaF_2 window, and so

could not be disassembled. Air chambers were built in so that background scans could be periodically taken during experiments without moving the device. Later, CaF_2 windows were modified with a thin layer of silicon to improve device sealing (Grenci et al., 2012; Mitri et al., 2014).

Other innovations in microfluidic setups include the use of an open channel microfluidic device which allowed the long term monitoring of cell lines for as long as 7 days by micro-spectroscopy (Loutherback et al., 2015). Birarda et al. (2016) have worked to lower the cost of microfluidic device fabrication by developing a method involving embedding IR transparent windows in PDMS. Chan and Kazarian (2013a) also developed a low-cost method of adding microfluidic channels to commercially available optical flow cells. A mylar spacer was sandwiched between two windows and a micro-drop system printed wax droplets directly on the bottom window to form precise channels.

ATR-FTIR spectroscopic imaging avoids this problem as the effective path length is not defined by the sample thickness. Instead the challenge for ATR measurements is that cells must be in direct contact with the ATR crystal. This means in practice that cells must be grown directly on the surface of the ATR element.

2.9.3 FTIR Spectroscopy Using a Synchrotron Source

As previously mentioned, live cell FTIR spectroscopy experiments are challenging because of the high absorbance of water and the high spatial resolution requirements. The high brilliance of synchrotron sources can help with these challenges and consequently most FTIR spectroscopy of live cells has been done using a synchrotron source.

Synchrotron sources have been mainly employed for micro-spectroscopy, where an aperture and MCT detector are used in combination with a microscope. The infrared beam size from a synchrotron is generally 10-20 µm and retains over 80% of its power through a 10 µm aperture (Miller and Dumas, 2006). This means much better signal to noise can be obtained compared to an incandescent source when illuminating very small subsections of a sample. Good signal to noise can be achieved using a 3 µm aperture with this configuration, allowing diffraction limited areas of a sample to be measured. Once the diameter of the aperture increases above 70 µm, there is no advantage to using a synchrotron source in terms of infrared throughput. This has implications for spectroscopic imaging, where the area of the detector array chip is 2 mm^2 for a 64×64 array detector. The beam is not wide enough to illuminate the whole detector array chip, and expanding the beam to do so would give no better performance than a globar source.

This has been addressed by combining multiple beams to increase the illumination area (Nasse et al., 2011). Until more powerful sources become more widely used, it is likely that the majority of transmission mode FTIR studies on cells will remain at synchrotron facilities. A multibeam synchrotron source has also been combined with ATR-FTIR spectroscopic imaging and demonstrated the ability to image live cells (Mariangela et al., 2011). However, the most meaningful work on live cells using ATR mode has been done using incandescent sources which will be covered in section 2.11.

2.9.4 Effect of Chromatic Aberration from IR Transparent Windows

Often transmission mode flow cells and microfluidic devices employ infrared transparent windows such as CaF_2. Unfortunately in a microscopy experiment light is not travelling normal to the sample and refraction occurs upon entering the window. This introduces chromatic aberration, and frequencies across the infrared region will not focus at the same point within the sample. This reduces the quality of spectra collected in micro-spectroscopy, and images collected in spectroscopic imaging.

Chan and Kazarian (2013b) overcame this issue by employing an additional CaF_2 window acting as a solid state immersion lens. Solid immersion optics are usually a single hemispherical or superhemisherical lens (Wu et al., 2000), but this additional CaF_2 window was designed so that, in combination with the top sample window, it formed a pseudo-hemisphere. With this configuration infrared light meets the

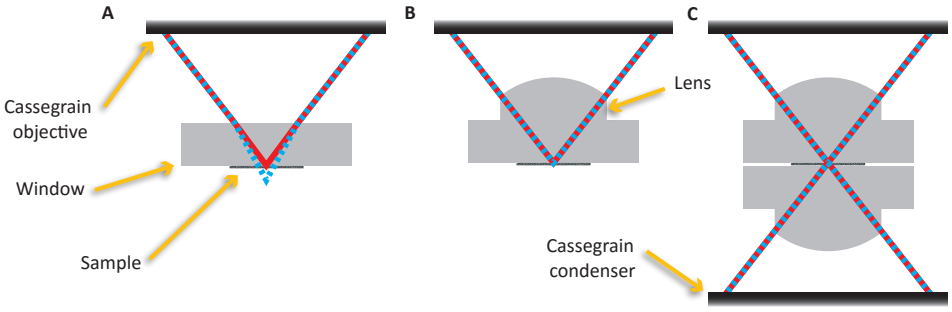


Figure 2.12: Illustration of using an additional lens to remove chromatic aberration. Section (A) illustrates chromatic aberration through an infrared transparent window. Section (B) shows the addition of the lens to the top window, forming a pseudo-hemisphere. This has the same effect as using a hemispherical solid immersion lens. This increases the spatial resolution by 1.4× in addition to removing chromatic aberration. Part (C) shows the setup for samples between two windows. A bottom lens is added to improve illumination from the condenser

window-air boundary normal to the interface, so no refraction occurs. An additional benefit from this approach was a 1.4× increase in spatial resolution, corresponding to the refractive index of CaF_2.

This was then combined with a second window (Chan and Kazarian, 2013a) to improve illumination from the condenser. Kimber et al. (2016) further developed the methodology so that the lens could be used when mapping tissue samples.

2.10 Transmission Mode FTIR Spectroscopy and Spectroscopic Imaging

2.10.1 Protein Conformation

As mentioned in section 2.1 of the literature review, cells are primarily composed of proteins, lipids, nucleic acids, and water. These are also the source of the primary spectroscopic bands we see in the infrared spectrum of a cell.

The strongest infrared bands seen from a cell are assigned to amide I and II at 1640 cm^{-1} and 1550 cm^{-1}, which correspond to protein. It has been known for a long time that the amide I band is sensitive to changes in protein's secondary structure, so the amide I band can be used to probe protein conformational change. Mitri et al. (2015) used FTIR micro-spectroscopy to study the spectral changes induced in live cells by heat shock. They found a common spectral signature of the heat shock response in two cell lines. Using 2D correlation analysis, a persistent increase of β-folded protein aggregate from 40 minutes to 2 hours was seen. Post-translational modifications of proteins have also been studied. It was demonstrated that protein phosphorylation could be detected during neuronal differentiation from a marked increase in the intensity of the 1080 cm^{-1} phosphate I band (Chen et al., 2012).

FTIR spectroscopic imaging using a multibeam synchrotron source has also been used to study protein misfolding in live cells (Gelfand et al., 2015). CHO cells were transfected to overexpress a mutant superoxide dismutase (SOD1) enzyme, which included a fluorescent tag for identification. SOD1 is an important enzyme, and its aggregation is involved in the disease amyotrophic lateral sclerosis. Cells producing high-intensity fluorescence were selected and imaged for 24 hours. The high protein regions of the cytosol were found to have a high antiparallel β-sheet structure consistent with the structure of SOD1 protein. As the time course progressed the overall proportion of parallel β-sheet increased in these regions, which has been previously identified as a marker of aggregation in vitro.

2.10.2 Cell Cycle

Boydston-White et al. (1999) first illustrated that the FTIR spectrum of a cell varied depending on its phase in the cell cycle. Cells were sorted using fluorescence-activated cell sorting (FACS) and dried before being measured by micro-spectroscopy. This was an important insight and had implications for the results of previous studies. For example, experiments on exfoliated cells presented spectral differences between normal, dysplastic and neoplastic human cervical tissue (Chiriboga et al., 1998). It became clear that it was the overall difference in distribution of cells in each of the cell cycle phases that was being detected. Cell heterogeneity due to its phase has been shown to cause difficulty discriminating diseased and non-diseased cells, as well as drug-cell interactions and responses to radiation (Bedolla et al., 2013).

Although there are now many studies illustrating spectral differences due to cell-cycle phase, there is not an exact consensus. This is likely to be due to differences in fixation or drying protocol, which are known to distort the spectra of cells. Cell phase discrimination experiments were first done on live cells more recently (Whelan et al., 2013; Bedolla et al., 2013). Bedolla et al. (2013) used the mitotic shake-off method to select for cells in the mitosis phase of cell division. This ensured that all cells being monitored had a roughly synchronised cell phase progression. The cells were then monitored over a 21 hour period and spectral differences as a function of time could be correlated to different cell phases. Whelan et al. (2013) analysed subsamples of B16 cells synchronised in G0 phase, S phase, and asynchronised by both flow cytometry and FTIR micro-spectroscopy. They found they could distinguish cells into three groups G0/G1, S, and G2/M. They did this primarily on the intensity difference in phosphate I and II at 1080 cm^{-1} and 1230 cm^{-1}, respectively. They showed in subsequent work that they could use this model to classify unknown B16 cells independently of flow cytometry (Bedolla et al., 2014). They also improved the model to enable G0 and G1 phase to be distinguished.

2.10.3 Spectral Changes from Exogenous Molecules

Direct drug detection has not been achieved so far in spectroscopic imaging of living cells, although it has been achieved in fixed cells with a metal-carbonyl derivative compound (Mattson et al., 2013; Clède et al., 2012a; Quaroni et al., 2015). However, studies have demonstrated that biochemical changes from exposure to exogenous molecules and other perturbations can be detected. Munro et al. (2010) exposed cells to 100 µM solution of arsenic trioxide and observed spectral changes

in the lipid region and phosphate bending modes within two hours. Effects have also been reported from nanomolar concentrations of the well studied toxin 2,3,7,8-tetrachlorodibenzo-p-dioxin (TCDD) (Holman et al., 2000a). Spectral changes induced from starvation (Kuimova et al., 2009), UV exposure (Lipiec et al., 2014), and mechanical compression (Birarda et al., 0) have also been reported. It is also worth mentioning that infrared imaging based on the photothermal effect has been recently used to detect an exogenous lipid inhibitor with submicron resolution in a living cell (Zhang et al., 2016).

2.11 ATR-FTIR Spectroscopy and Spectroscopic Imaging

There have been much fewer attempts to apply ATR-FTIR spectroscopy to the study of live cells present in the literature. Schmidt et al. (2007) first demonstrated that ATR-FTIR spectroscopy could be used to examine live cells. Upon cell adhesion to a diamond ATR crystal, infrared bands corresponding to cells could be observed. The strength of infrared bands was related to cell morphology and coverage of the ATR crystal surface. Kuimova et al. (2009) then applied micro ATR-FTIR spectroscopic imaging to live cells. SKOV cells were grown directly onto a diamond ATR crystal and imaged using a Specac ATR imaging Golden Gate. They examined the spectroscopic effects of cell starvation, observing a high reduction of a phosphate I sub-band at 1020 cm^{-1}. One disadvantage of this sampling mode is that when cells are put under stress they tend to become more rounded. This reduces their contact with the crystal, and thus the absorption signal. This can be partially dealt with by normalising the spectra relative to a spectral band known to be constant. Kuimova et al. (2009) used this to show that the band at 1020 cm^{-1} decreased much faster than the amide II band.

There have also been studies involving a related technique, infrared surface plasmon resonance FTIR (SPR-FTIR). It uses a similar setup to ATR-FTIR spectroscopy, using a continuous infrared source with a gold coated high refractive index prism. It measures internal reflectivity as a function of wavelength, which exhibits a sharp minimum during surface plasmon excitation at the metal surface. Changes in the wavelength of minimum reflectance corresponds to changes in the sample's refractive index, which in some setups can be quantitatively determined (Zilbershtein et al., 2012). This technique has been used to detect changes in cholesterol enrichment within the membrane of live cells (Ziblat et al., 2006). It has also been used to detect glucose uptake (Golosovsky et al., 2009).

Multiple-reflection ATR accessories have also been used to study live cells. Although cell populations are studied rather than single cells, this sampling mode is currently the only FTIR setup that has been able to directly detect drugs within living cells (Chan and Fale, 2014). 5-fluorouracil was added to the medium of cells adhered to a multiple-reflection ZnS crystal. Within 20 minutes accumulation of the drug could be detected within the cell population. This methodology was also employed with the drug doxorubicin in three cell lines (Fale et al., 2015). Although the drug was not directly detected in this case, it was shown that amide intensity correlated with cell viability, and it was demonstrated that the three cell lines had different resistance levels to doxorubicin. PCA analysis also highlighted different biochemical responses from the three cell lines, perhaps indicating different modes of action.

2.12 Raman Spectroscopy

Whilst not the main subject of this literature review, it is important to note that Raman spectroscopy, and its related nonlinear scattering techniques, have also been used extensively to the study live cells. To detail this comprehensively would be the subject of an entire literature review, and only a brief summary is presented here.

Generally the laser frequency used in Raman experiments is in the near infrared or visible region, so it can achieve higher spatial resolution than seen in infrared measurements. Spontaneous Raman micro-spectroscopy is able to distinguish the nucleus, nucleolus, cytoplasm, membrane, and endoplasmic reticulum of a cell without the use of Raman probes (Klein et al., 2012). Another advantage of Raman spectroscopy is the low spectral contribution from water in the fingerprint region, reducing the challenge of working in aqueous environments.

If a 532 nm laser is used, Raman micro-spectroscopy benefits from a resonant electronic transition in cytochrome C, present in mitochondria (Onogi and Hamaguchi, 2010). This allows cytochrome C to be studied directly in living cells (Kakita et al., 2013; Yamakoshi et al., 2015). Raman spectroscopy has also been shown capable of quantitative analysis of lipid metabolism (Zhang et al., 2017; Hosokawa et al., 2014).

Spontaneous Raman micro-spectroscopy has also successfully visualised metal-carbonyl complexes in live cells (Meister et al., 2010), as well as paxitol (Salehi et al., 2013), and doxorubicin (Farhane et al., 2015). Surface enhanced Raman spectroscopy (SERS) has been used to monitor drug metabolism within cells (Yang et al., 2012), exploiting the signal enhancement in the cytoplasm from gold nanopar-

ticles. Stimulated Raman scattering (SRS) has also been used to visualise tyrosine kinase inhibitors in living cells. In conjunction with a lysosome specific fluorescence marker, it was also determined that the inhibitors accumulated in the lysosome (Fu et al., 2014).

Whilst Raman can be label-free, there has also been a lot of work developing Raman probes, which typically have a lower molecular weight than fluorescent markers (Palonpon et al., 2013). For example, the uptake and metabolism of allyne and nitrile labelled drugs have been monitored in live cells with SRS (Tipping et al., 2017; Yamakoshi et al., 2014). Stable isotope labelling can also be used to develop Raman probes (Wei et al., 2016, 2013). Both SERS and resonance Raman probes that localise in specific organelles have been developed (Kang et al., 2015; Kuzmin et al., 2016).

3 Experimental

3.1 Cell Culture Equipment and Reagents

HEK 293a cells were maintained in either T25 or T75 tissue culture flasks using high glucose Dulbecco's modified Eagle's (DMEM) medium with GlutaMAX™ (Thermo Fisher Scientific). Cell medium was supplemented with 10% fetal bovine serum, 1% penicillin–streptomycin, and HEPES buffer to a concentration of 25 mM. The cultures were incubated in a 5% CO_2 environment at 37°C using a HERAcell incubator. Where a sterile environment was required, a HEPA filtered Herasafe KS Class II bio-safety cabinet was used.

3.1.1 Subculturing

Cells were subcultured once 70% confluency was reached. Cell medium was aspirated from the flask and the cell culture was washed with PBS buffer. 1 ml of trypLE was added to the flask, which was then incubated for 2 minutes to let the cell culture dissociate. Cell medium was added to make a cell suspension of 5 ml, which was transferred to a 50 ml centrifuge tube and centrifuged. The supernatant was aspirated and the cell pellet was resuspended in 1 ml of new cell medium. 0.2 ml of the cell suspension was added to a new culture flask, previously filled with cell medium, to make a final volume of 5 mL. The remaining suspension was discarded or used for an FTIR measurement. Cells were not explicitly counted using a haemocytometer unless their number was needed to calculate the seeding density in an FTIR measurment.

3.1.2 Cell Freezing Protocol

Cells were subcultured as in section 3.1.1 using a T75 tissue culture flask. After centrifugation, the cell pellet was suspended in 6 ml of freezing medium, and 1 ml aliquots of this suspension were added to 6 Corning self-standing cryogenic vials. The cell density in each vial was approximately 1.4×10^6 cell ml^{-1} . The vials were moved to a Nalgene Cryo 1°C Freezing Container, previously filled with isopropanol,

and placed in a -80°C freezer for at least 12 hours. The vials were then moved to a Stratebourne bio-10 N_2 tank for storage, which was periodically topped up at least once a fortnight with liquid nitrogen.

3.1.3 Cell Thawing Protocol

A cryovial containing frozen cells was thawed in a 37°C water bath for 2 minutes. The vial was than transferred to the bio-safety cabinet, and the cell suspension was added drop-wise to a 50 ml centrifuge tube containing 4 ml of cell medium. After centrifugation, the supernatant was removed and the cell pellet was resuspended in 1 ml of cell medium. Finally, the 1 ml cell suspension was added to a T25 tissue culture flask, prefilled with 4 ml of cell medium, to make a final volume of 5 ml, and incubated. After 24 hours the medium is changed and, once 70% confluence was reached, the cell culture was subcultured.

3.2 Multiple-Reflection ATR-FTIR Spectroscopy Measurements

All single beam FTIR measurements were done using a Bruker IFS 66 spectrometer with a Mercury-Cadmium-Telluride (MCT) detector. The detector was filled with liquid nitrogen and allowed to stabilise for an hour before any measurements. The spectrometer was set up to record between 900-4000 cm^{-1}. As previously mentioned in section 2.4, the highest wavenumber the interferometer can digitise is defined by the number of zero crossings counted before the spectrometer's ADC is triggered. This was set to 3, corresponding to a high wavenumber limit of 5266 cm^{-1}. The interferometer speed was set to 60 kHz so that, combined with an electronic low pass filter, no light of a higher wavenumber than 5266 cm^{-1} would reach the detector, which would result in spectral distortions. The spectral resolution was set to 2 cm^{-1} so that the infrared bands corresponding to water vapour could be more effectively subtracted. Unless otherwise stated, 512 coadded scans were taken during a measurement.

Specac's Gateway™ multiple-reflection ATR accessory was used with a germanium crystal. The accessory must be aligned for optimum signal before measurements can be taken. Referring to figure 3.1, mirror 1 directs infrared light from the spectrometer to the ATR crystal and mirror 2 directs light from the accessory to a parabolic mirror just before the detector. The stage below the accessory has tracks so that the accessory can be secured in the middle of the spectrometer sample chamber.

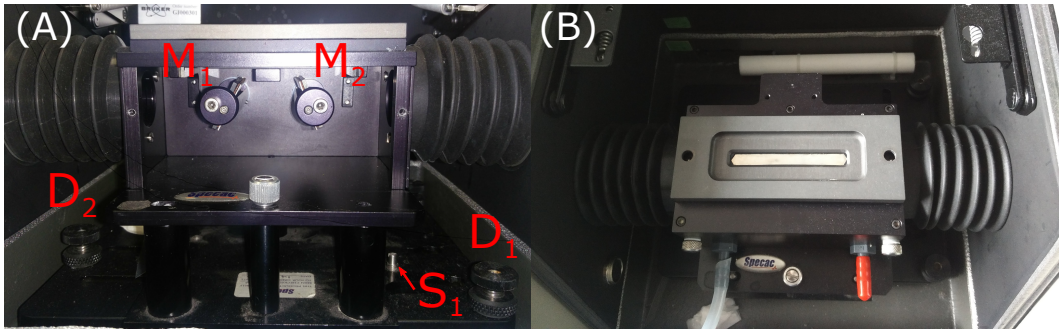


Figure 3.1: The Specac multiple-reflection ATR accessory. Infrared light travels into the sample compartment from the right and hits mirror 1. Mirror 1 controls the angle infrared light meets the ATR crystal. Mirror 2 aligns the path from the accessory to the detector. Screw 1 fixes the accessory position in the sample compartment. Dials 1 and 2 on the stage ensure the accessory is level. (B) The same ATR accessory within the spectrometer's sample compartment and connected to a purged air supply.

Finally, the stage dials can be tweaked to ensure that the accessory is level.

Once the accessory has been aligned, the analog-to-digital converter (ADC) settings are optimised. The ADC converts the voltage produced by the detector element to a 16 bit number, resulting in a maximum range of -32767 to +32768. To maximise the dynamic range of the ADC, and thus the range of signal strengths that can be detected, it must be ensured that the interferogram peak is close to this value. In practice, the absolute value of the centerburst should not be higher than 28000 counts as spectral baseline distortions, due to detector response non-linearity, are observed. In experiments with the multiple-reflection accessory, a 5 mm aperture was used in combination with a gain setting of two. The accessory was also connected to a dry air supply for at least two hours prior to any measurements. This was to ensure that minimal water vapour was present in the infrared beam's optical path.

3.3 Micro ATR-FTIR Spectroscopic Imaging

Micro ATR-FTIR spectroscopic imaging experiments were done using an Agilent 670 spectrometer coupled with a Cary-620 microscope. The microscope is equipped with both a single element MCT detector and a 128×128 pixel MCT-FPA detector, manufactured by Santa Barbra Focalplane. The microscope is also equipped with a 15× 0.62 NA objective with a slide-on germanium ATR accessory

The interferometer scanning speed was set to 5 kHz and the number of zero crossings was set to 4, corresponding to a high wavenumber limit of 3950 cm^{-1}. An

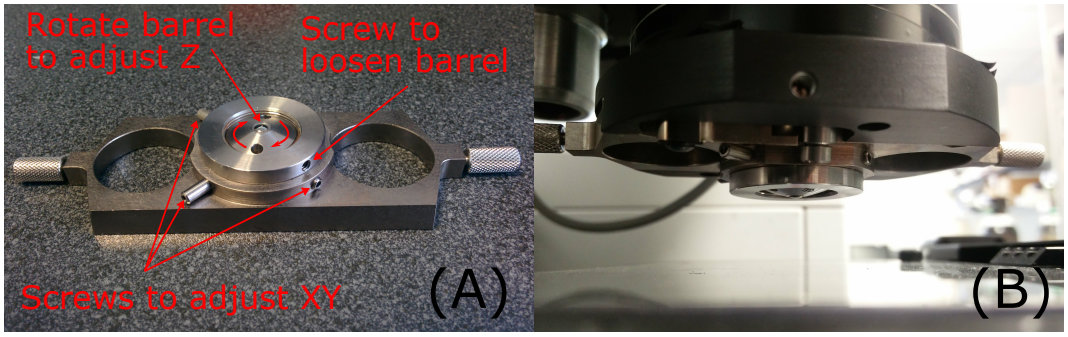


Figure 3.2: Agilent's germanium micro-ATR accessory. Picture (A) shows the accessory inverted. Picture (B) shows the same accessory mounted on the Agilent microscope objective.

3900 cm^{-1} optical low pass filter was placed directly in front of the FPA to ensure no higher frequencies of infrared light reach the detector.

To ensure the best image quality, the germanium ATR accessory must be periodically aligned. Although the FPA has 128×128 pixels, in ATR mode there is virtually no illumination beyond a 64×64 pixel area. WinIR, Santa Barbra Focalplane's software, can be used to set which region of the detector array is active. Only using a subset of the available pixels has the added advantage of allowing the FPA to work at a higher refresh rate. When this particular system is properly aligned in ATR mode, a 64×64 pixel window starting at row 8 and column 8 should be selected.

The Ge accessory must be aligned in the Z direction for optimum focus and in the X-Y plane to ensure that the ATR image corresponds with the centre of the visible image (i.e. when the crystal is removed from the objective). Referring to figure 3.2, the focus is changed by rotating the threaded barrel in middle clockwise or anticlockwise. In practice the best procedure is to optimise Z for maximum illumination and then make sure the illumination hits the middle of the selected area of pixels. Once this has been done generally only minor adjustments to the focus and xy plane position are needed using an 1951 US Air Force (USAF) resolution target. The desired area of the target should be aligned to the centre in the visible microscope. Before lowering the ATR accessory, a non-uniformity correction must be done, so it can be more easily seen when the crystal makes contact with the sample. Figure 3.3 shows the ATR accessory in contact with the USAF target and the corresponding image in the visible microscope when the crystal is well aligned.

As with single element MCTs, the FPA settings must be changed to optimise the ADC. The FPA ADC is 14 bit, corresponding to number range of 0 to 16384. The FPA frame rate should be set as fast as possible for the window size. The integration time, gain, and offset can be used to optimise the ADC. Detector nonlinearity is seen if any of the pixels have a reading above 8192 counts or below around 1000 counts.

When large numbers of scans are needed by this system, fluctuations in the source intensity over time can lead to baseline distortions. This can be greatly reduced by using the aperture required for for 2 cm^{-1} spectral resolution.

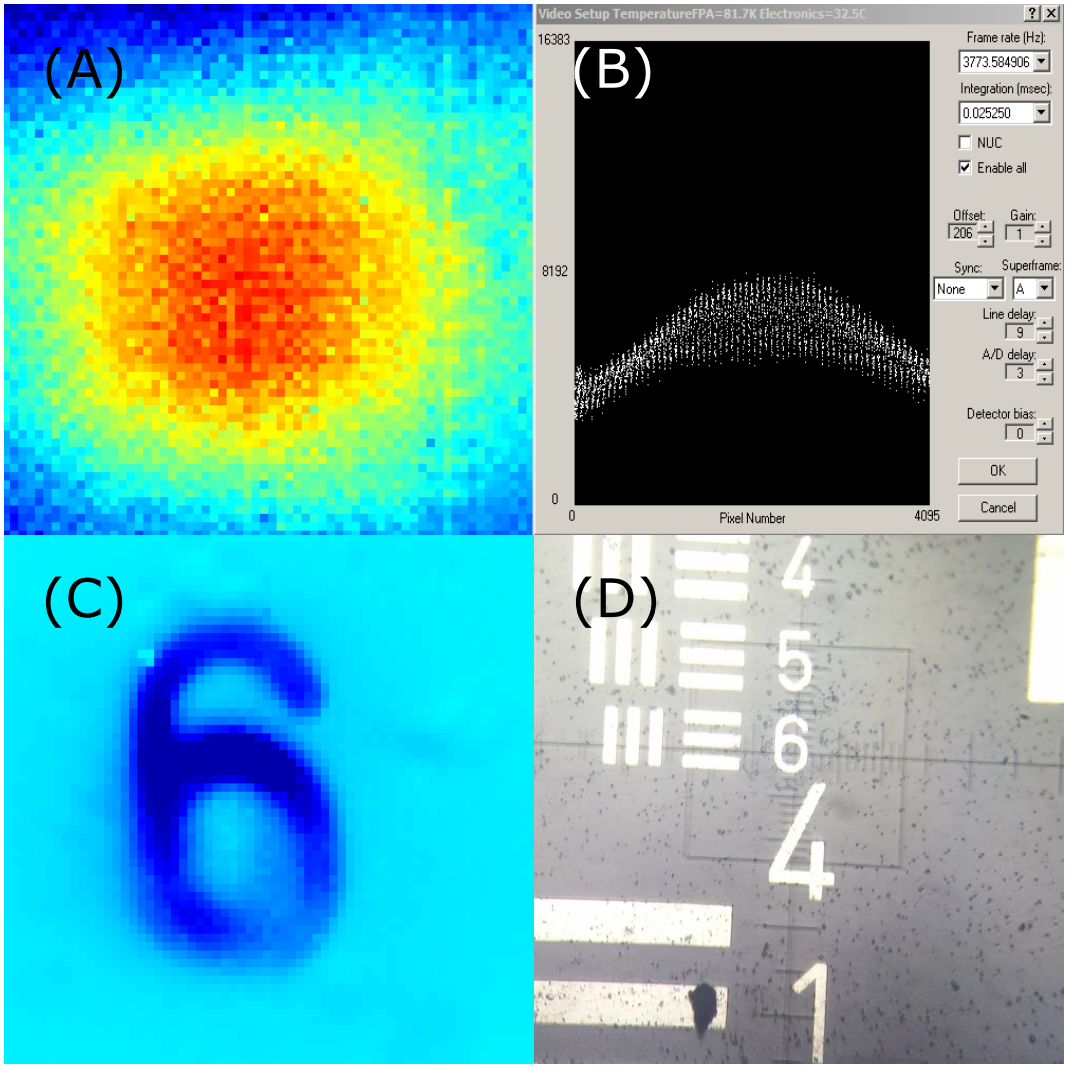


Figure 3.3: (A) Live view of the illumination of the FPA detector in ATR mode when the germanium accessory is well aligned. (B) Settings to achieve the maximum dynamic range from the ADC. (C) Live view of the FPA detector while the germanium accessory is in contact with a USAF 1951 resolution target, after a non-uniformity correction. (D) The corresponding visible image.

3.4 Data Import

Due to the limited data manipulation and analysis offered by Agilent's software Resolutions Pro, data was exported to Matlab. For one spectroscopic image, Resolutions Pro generates three files: the dat file which is the processed data, the seq file which is the raw data (interferograms), and the bsp file which contains the information needed for Resolution Pro to load the dat file. The simplest way to export the file is to the use the 'export to ENVI' option in Resolution Pro. This generates a hdr file which contains some of the information needed by Matlab to interpret the dat file, which is a binary file. The hdr file also contains the wavenumber values. Matlab's multibandread function can then be used to import the dat file. The syntax of the functions is

```
1  ImportedDataArray = multibandread(filename, size, precision, offset,
       interleave, byteorder)
2  % filename - fullpath of the file dat file if not in the current
       directory
3  % size -  Three-element vector of integers consisting of [height,
       width, N]. The values are can be found in the hdr file.
4      % height/samples - total number of rows (number of y pixels)
5      % width/lines - total number of columns (number of x pixels)
6      % N/bands - total number of bands (numbers of discrete
           wavenumbers recorded)
7  % precision - how many bytes per number. Should be set to 'single'.
8  % offset - where the function starts reading. Can be found in the hdr
       file
9  % interleave - how the data is organised in the dat file. Should be
       set to 'bsq'
10 % byteorder - which direction the numbers are written in. Should be
       set to 'ieee-le'
11 %ImportedDataArray = three dimensional number array
```

Importing Opus files from Bruker's software is more straightforward. The open source Matlab toolbox IRootlab (Trevisan et al., 2013) comes with an OpusImport function that can be used separately. This is a Matlab p function that can directly import Opus files to Matlab arrays.

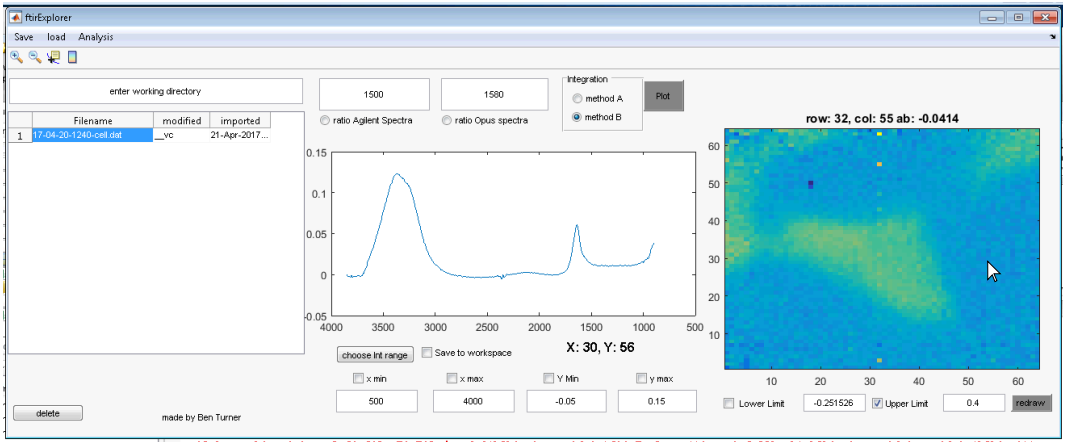


Figure 3.4: Screen shot of the Matlab GUI developed for spectroscopic image analysis. The GUI shows an integrated absorbance image on the right. By clicking on a pixel of interest its spectrum is plotted in the graph in the middle.

3.5 Matlab GUI

Whilst Matlab is more flexible than Opus and Resolutions Pro, it does not have any graphical data exploration tools suitable for spectroscopic imaging data. This lead to the development of a Matlab graphical user interface (GUI) which can import both Opus and Resolutions Pro data files and allows users to do routine univariate analysis. The interface is shown in figure 3.4. Most of the preprocessing and data analysis presented in this thesis was built using this GUI as a platform.

Two functions built into this GUI that were found particularly useful are the ability to average a user defined region of pixels, and to reject pixels outside a user defined area. Other functions built into this GUI are: vector normalisation, MSC, EMSC, PCA denoising, vapour correction, gaussian filtering, box filtering.

3.6 Integration Methods

The most common univariate analysis method for spectroscopic imaging datasets is integration of a particular peak across all of the pixels. There are several ways to achieve this and the nomenclature found in the spectroscopy software Opus is used in this thesis for consistency. The four main methods are illustrated in figure 3.5. Method A simply integrates a specified band region, whereas method B does this relative to a local baseline. Generally, method B integration generates better quality absorbance images as it reduces the effects of baseline variation between pixels. Unless stated otherwise, method B integration is used to generate the integrated absorbance images in this thesis. Method R and P integration simply uses the

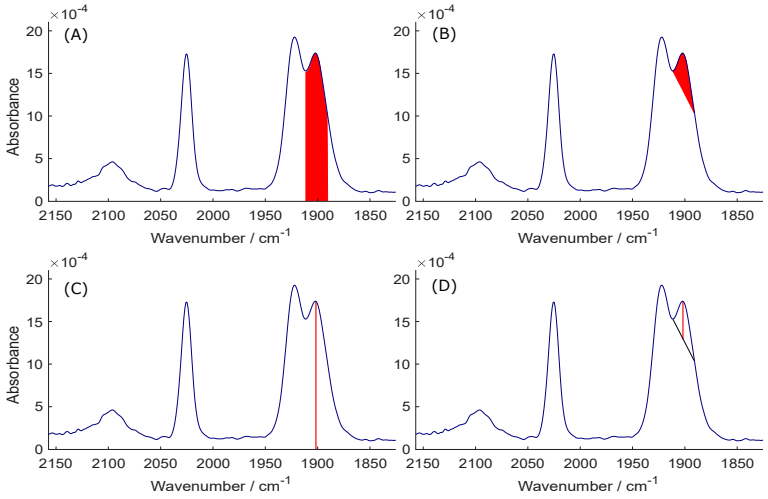


Figure 3.5: Illustration of the four main different integration methods used in univariate analysis of spectroscopic images. These methods, using Bruker's nomenclature, are referred to as: (A) method A, (B) method B, (C) method P, (D) method R.

absorbance value at one wavenumber, with and without a local baseline correction for R and P, respectively. Whilst these were not used to generate absorbance images, these methods of integration were used as part of disrelation mapping analysis in chapter 6.

4 ATR Spectroscopy and Spectroscopic Imaging of Live Cells

This chapter presents the work undertaken to establish the methodology for micro ATR-FTIR spectroscopic imaging of live cells, building on previous experiments carried out in the Kazarian group. The methodology presented here is subsequently used in both chapter 5, where HEK 293a cells are imaged after incubation with a metal-carbonyl derivative compound, and chapter 6, where spectroscopic images of live cells are subjected to disrelation mapping analysis.

4.1 Introduction

Micro ATR-FTIR spectroscopic imaging of live cells was first reported by Kuimova et al. (2009) using an UMA 600 Agilent infrared microscope with a slide-on germanium accessory. To do this cells were cultured directly onto the germanium crystal surface. The microscope had an upright configuration, meaning that when the germanium accessory is mounted on the microscope objective it is inverted, as shown in figure 3.2. This is so it can be lowered into contact with traditional samples placed on the microscope's sample stage. This presented a challenge for the measurement of live cells, as they must be maintained in an aqueous environment whilst the ATR accessory is both upright and inverted.

To overcome this issue a chamber was glued onto the germanium accessory as shown in figure 4.1B. The chamber diameter was small enough to ensure capillary forces could hold cell medium inside the chamber whilst the accessory was inverted. This meant cells could be seeded onto the surface of the accessory whilst upright and the entire accessory could be placed inside an incubator. Once cells were properly adhered to the ATR crystal, the accessory could be inverted, allowing measurements to be taken. To encourage cells to adhere to the crystal, it was previously coated with a thin layer of poly-L-lysine. Figure 4.1 shows the resulting integrated absorbance

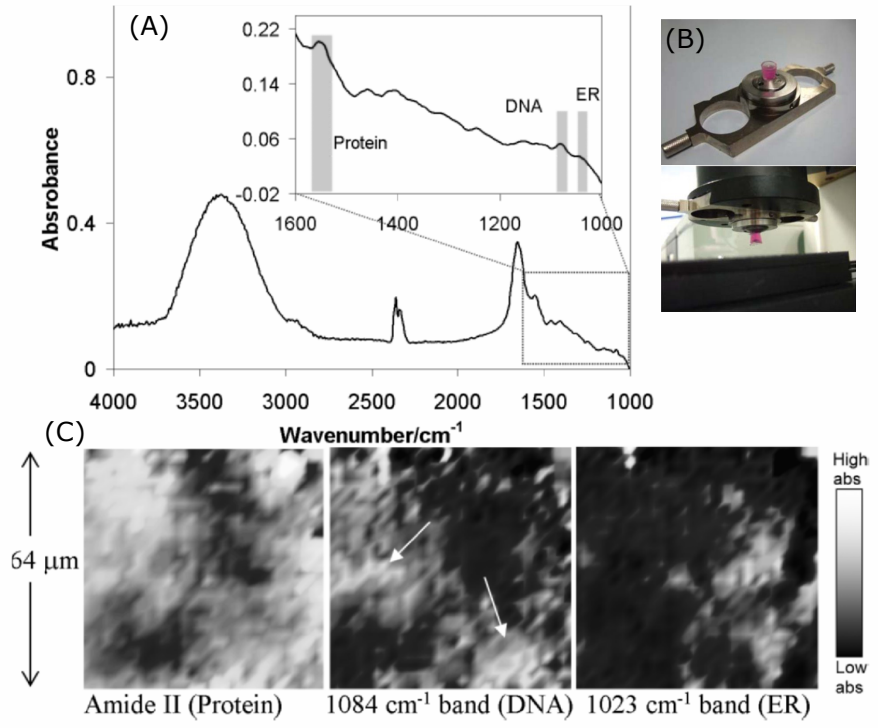


Figure 4.1: Reproduced from Kuimova et al. (2009). (A) A typical spectrum of a cell from a germanium micro ATR-FTIR imaging dataset. (B) Pictures illustrating the chamber used to ensure cells were submerged in medium throughout incubation and measurement. (C) Integrated absorbance images showing the chemical distribution of amide II, phosphate I, and glycogen.

images generated using infrared spectroscopic bands centred at 1540 cm^{-1}, 1080 cm^{-1}, and 1023 cm^{-1}. These correspond to amide II, phosphate I, and a sub-band of phosphate I assigned to glycogen.

4.2 Methodology Development

4.2.1 Chamber

A new chamber was designed for this work by modifying the protective cap that originally came with the ATR accessory. A polydimethylsiloxane (PDMS) mold was fashioned that could be placed inside the cap. When the cap was placed on the ATR accessory the PDMS device formed a chamber around the germanium crystal. This chamber had the benefit of being convenient to remove as it did not require glue, relying on pressure from the cap to form a seal. When the chamber was placed inside the incubator, the top was sealed to minimise water evaporation during the incubation period. To allow gas exchange inside the incubator, a small hole was made through the side of cap and the PDMS device, as illustrated in figure 4.2B.

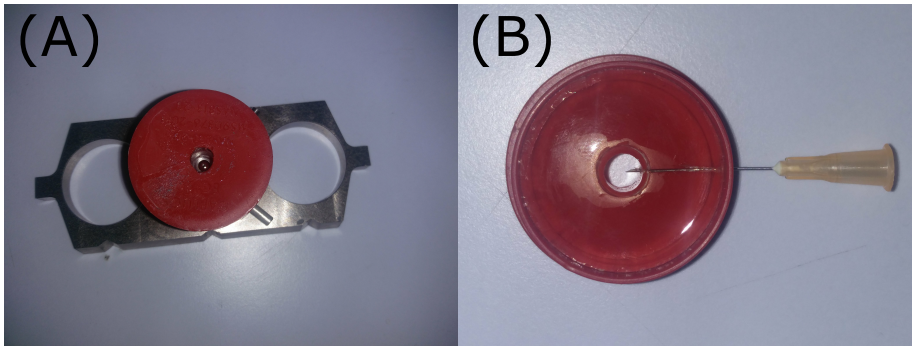


Figure 4.2: Pictures illustrating the new chamber designed for ATR-FTIR spectroscopic imaging experiments on live cells. Picture (A) shows the chamber mounted on the Ge accessory. Picture (B) shows the chamber inverted. The needle illustrates a small hole in the side of the chamber. This was to ensure gaseous exchange during incubation when the top of the chamber is sealed.

4.2.2 Experimental Procedure

The germanium accessory was mounted onto the objective, with the chamber attached, and a background measurement was taken using the settings described in section 3.3. After the background measurement, the ATR accessory was removed from the objective and the chamber was filled with 150 µl of cell medium. HEK 293a cells were then subcultured as detailed in section 3.1.1. A cell suspension was added to the chamber to a final cell density of 1×10^4 cells ml^{-1}. The whole accessory was placed inside a CO_2 incubator for at least 16 hours. The accessory was then remounted and the sample measurement was taken.

4.2.3 Water Vapour Removal

Due to experimental constraints, the background measurement was taken up to 20 hours before the sample measurement. This meant changes in the instrument's environment, such as temperature and local humidity, lead to distortions in the sample's absorbance spectrum. Another complication was that the removal and replacement of the ATR accessory on the microscope objective allowed water vapour to enter the instrument. This caused contamination of the sample's absorbance spectrum with water vapour bands, which particularly affect the amide I and II region.

As the the level of water vapour could not be kept constant between the background and sample measurement, water vapour was instead subtracted from the resulting absorbance spectrum during data processing. A modified version of spectral length minimisation, first proposed by Kozlov and Besov (2011), was eventually used to optimally subtract water vapour. Immediately after the spectroscopic mea-

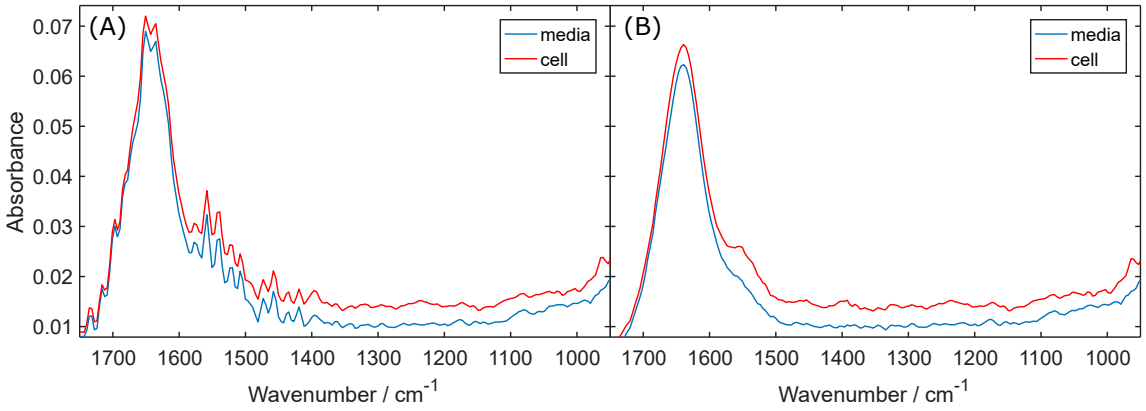


Figure 4.3: Plot (A) shows two spectra taken from the same FTIR spectroscopic imaging dataset but different pixels. The blue and red spectra are typical of cell medium and cells respectively. Plot (B) shows the same two spectra after water vapour has been optimally subtracted

surements of cells, a water vapour spectrum was taken using the single element MCT on the Cary 620 microscope. Water vapour was subtracted from each spectrum in the imaging dataset individually in an iterative fashion. The formula for the subtraction of absorbance spectra is simply

$$D_{IR}(\tilde{\nu}, k) = S_{sample}(\tilde{\nu}) - k.S_{wv}(\tilde{\nu}) \tag{4.1}$$

where D_{IR} is the difference spectrum, k is a real number, $S_{sample}(\tilde{\nu})$ is the sample spectrum, and $S_{wv}(\tilde{\nu})$ is the water vapour spectrum. The optimum k value is found by the minimisation of an appropriate objective function. In the original spectral length minimisation the following objective function is used

$$L(k, \tilde{\nu}) = \sum_{n}^{m} \sqrt{(\tilde{\nu}_n - \tilde{\nu}_{n-1})^2 + [D_{IR}(\tilde{\nu}_n, k) - D_{IR}(\tilde{\nu}_{n-1}, k)]^2} \tag{4.2}$$

which is interpreted as the spectrum's length. This objective function can be simplified by noting

$$\underset{k}{\operatorname{argmin}}\, L(k, \tilde{\nu}) = \underset{k}{\operatorname{argmin}}[L(k, \tilde{\nu})^2]. \tag{4.3}$$

Equation 4.3 states that the value for k that minimises the function $L(k, \tilde{\nu})$ will also minimises $L(k, \tilde{\nu})^2$, meaning it is not necessary to compute the square root. Equation 4.2 can be simplified further by imposing the constraint $(\tilde{\nu}_n - \tilde{\nu}_{n-1}) = 1$. As the values for $\tilde{\nu}$ are evenly spaced this amounts to a change of scale in the

wavenumber dimension. This allows $L(k, \tilde{\nu})$ to be simplified to

$$L(k, \tilde{\nu}) = m + \sum_{n}^{m} [D_{IR}(\tilde{\nu}_n, k) - D_{IR}(\tilde{\nu}_{n-1}, k)]^2 \tag{4.4}$$

The m term is a constant and can be ignored as it will not affect the arg min. The objective function is then

$$\underset{k}{\operatorname{argmin}} \sum_{n}^{m} [D_{IR}(\tilde{\nu}_n, k) - D_{IR}(\tilde{\nu}_{n-1}, k)]^2 \tag{4.5}$$

which can be interpreted as the integral of the squared first derivative spectrum of $D_{IR}(\tilde{\tilde{\nu}}, k)$. This objective function was minimised using a golden search. Figure 4.3 shows the absorbance spectrum of a cell and cell medium in the amide I and II region before and after water vapour subtraction.

4.2.4 Surface Modification of Germanium Accessory

To attempt to improve cell adhesion, biological coating protocols were attempted. After the background measurement, a poly-L-lysine solution was added to the chamber for 15 minutes. The chamber was then washed with sterile water and either allowed to dry prior to adding medium or medium was directly after washing. UV/ozone cleaning was also attempted. The germanium accessory was UV treated using a Bioforce UV cleaner for 20 minutes. The background measurement was taken im-

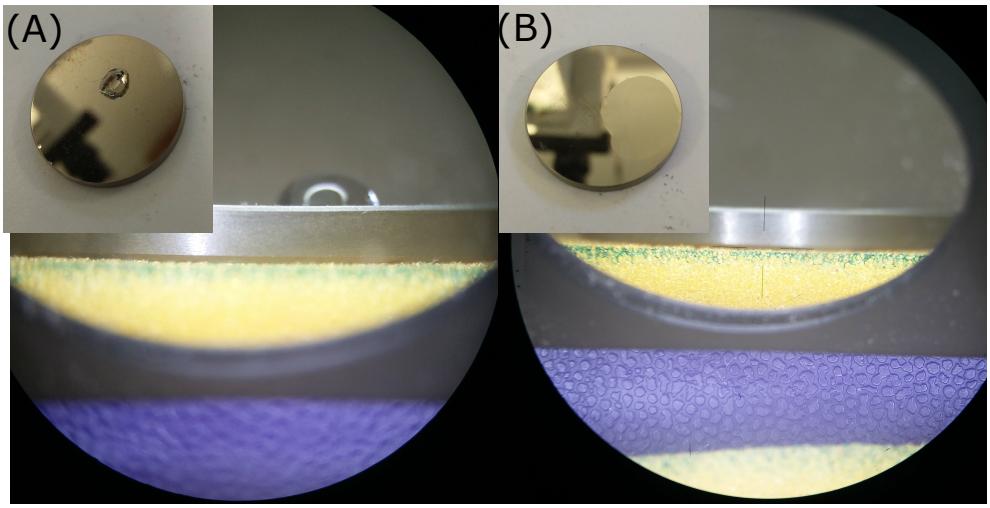


Figure 4.4: Pictures illustrating the difference in surface wettability of a germanium disk before (A) and after (B) UV/ozone cleaning. From the side on view it can be seen that the contact angle has been reduced to zero in picture (B) after UV/ozone cleaning.

mediately after cleaning and then covered with cell medium. As can be seen in figure 4.4, there is a significant improvement in germanium's surface wettability after the UV treatment.

4.3 Results and Discussion

4.3.1 Spatial Resolution of Micro ATR-FTIR Spectroscopic Imaging

As previously discussed, the USAF 1951 resolution target is an idealised sample and is not a good indicator for the achieved spatial resolution in real samples. For this reason, a polymer laminate was used to assess the spatial resolution of the Agilent Cary-620 microscope in ATR mode, as published in Kimber et al. (2016).

The integrated area between 3251 cm^{-1} and 3448 cm^{-1} was taken to generate the chemical image presented in figure 4.5. To assess the spatial resolution, one row of pixels going through the interface was selected and the integrated absorbance was plotted as a function of distance across the image, which was calculated using the projected pixel size. A logistic function was then fitted to the absorbance profile, which took the form

$$f(x) = \frac{L}{1 + e^{-k(x-x_0)}} + C \tag{4.6}$$

where x_0 is the midpoint and k is the steepness of the curve. $L + C$ and C define the curve's maximum and minimum value at the curve's limits. The least resolvable distance in this setting was defined as the distance between 5% and 95% of the

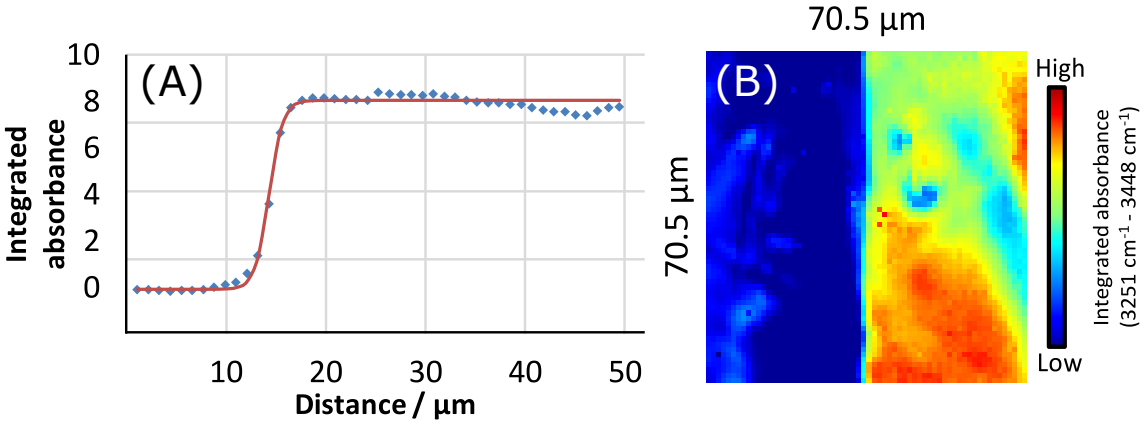


Figure 4.5: Integrated absorbance image of a polymer laminate obtained using micro ATR mode, adapted from Kimber et al. (2016). Plot (A) shows the integrated absorbance of one row of pixels extracted from integrated absorbance image (B). A sigmoid function has been fitted to plot (A) to assess the spatial resolution.

curve's maximum value. Using this framework, the microscope's spatial resolution was calculated as 3 µm in the 3251 cm^{-1} to 3448 cm^{-1} region, as shown in figure 4.5.

4.3.2 Cell Morphology on Germanium Surface

Initial tests indicated that cells would adhere and grow normally on a germanium window without any biological coating or surface modification. However, when cells were seeded onto the germanium ATR accessory they appeared rounded and ultimately were never successfully detected with ATR-FTIR imaging.

Poly-L-ysine coating of the crystal was also attempted. Figure 4.6 illustrates HEK 293a cells on the Ge accessory surface 16 hours after seeding onto to the crystal. Section A of the figure shows HEK cells 16 after seeding on a poly-L-lysine pretreated surface. There was no observable difference in morphology as a result of coating and cells were also not successfully detected with spectroscopic imaging.

UV/ozone cleaning was attempted to remove trace organic contaminants from the Ge accessory and to improve the hydrophilicity of the crystal. As shown in section B of figure 4.4, the contact angle of water was reduced to 0 ° after UV/ozone cleaning. Figure 4.6B shows the improved cell morphology 16 hours after seeding on a UV/ozone pretreated surface.

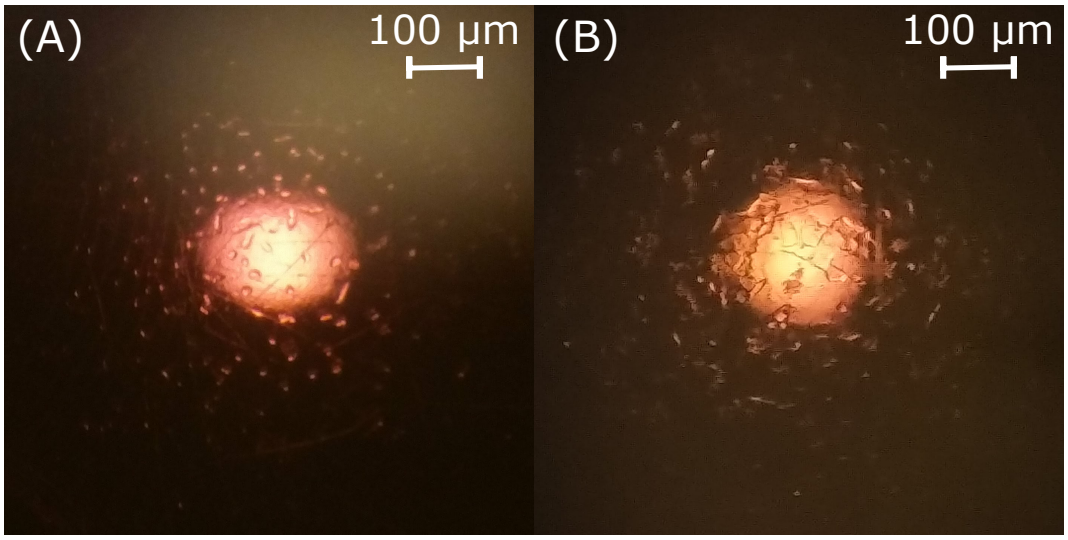


Figure 4.6: Visible images of cells directly on the Ge ATR accessory 16 hours after seeding. Both Images were acquired using a visible microscope in reflection mode. Image (A) shows the result of poly-L-lysine coating. Image (B) shows the result of UV/ozone cleaning.

4.3.3 Cell Detection Using the Amide II Band

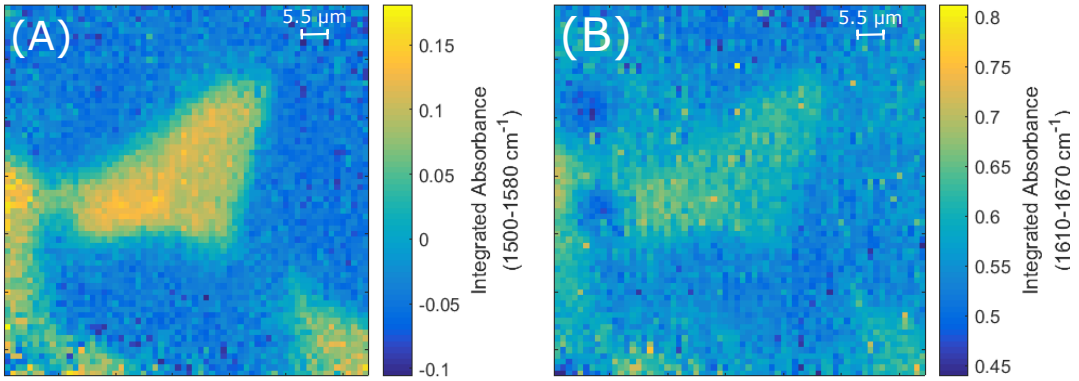


Figure 4.7: Integrated absorbance images of amide II (A) and amide I (B).

To acquire spectroscopic images with sufficient signal to noise, it was found that both good cell morphology, as shown in figure 4.6B, and 1024 coadded scans were required. Figure 4.7 shows a plot of the integrated absorbance of amide I and II. These are the strongest spectroscopic bands seen in cells and provide a good image of the whole cell. It can be seen that the image of amide II provides better contrast than amide I. This is because amide I overlaps with the OH bending mode of water. Although amide I absorbance increases inside the cell, compared to the surrounding cell medium, the concentration of water also decreases. This results in a lower overall difference in integrated absorbance across the pixels.

The integrated absorbance of amide II band in combination with k-means clustering was found to be an effective method of separating cell spectra from cell medium spectra. Figure 4.8C and D shows the results of k-means clustering on the amide II absorbance. Not only can cell be distinguished from medium but the cell border can be distinguished. It was found that the results of k-means clustering was greatly improved if a 3×3 box filter was applied to the image before clustering. In figure 4.8C noise across the image can be seen to affect the classification accuracy of the cell border from cell medium, which is not an problem in image D.

Figure 4.8E shows the average spectrum from all of the clusters found in figure 4.8D. It is important to note that the absorbance values obtained in these experiments appear to be roughly four times lower than shown in Kuimova et al. (2009). The absorbance values shown in Kuimova et al. (2009) are closer to values seen when using a diamond ATR accessory rather than germanium as reported.

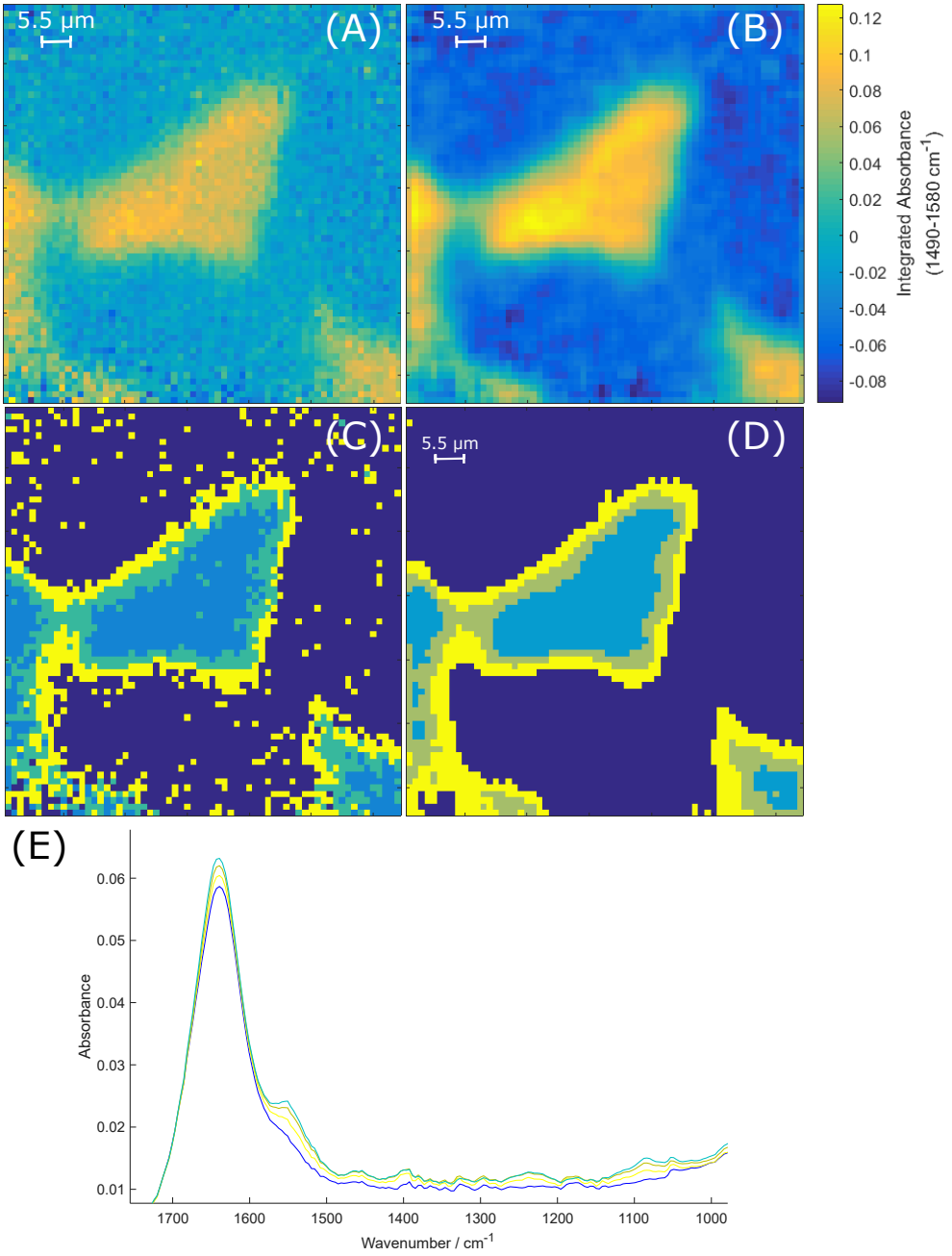


Figure 4.8: Integrated absorbance images of amide II before (A) and after (B) a 3×3 box filter was applied to the image. Image (C) and (D) show the results of k-means cluster analysis of image (A) and (B) respectively. Each colour represents membership to a different cluster. Plot (E) shows the average spectrum taken from all of the clusters in image (D).

4.3.4 Visualising the Cell Nucleus

To better visualise the cell spectrum, a spectrum of cell medium was subtracted from the dataset. Using the k-means cluster analysis shown earlier, an average medium spectrum could be obtained from the dataset directly. This ensured the water present in both the sample dataset and medium spectrum were at the same temperature. The medium spectrum was subtracted from each spectra in the imaging dataset using the equation

$$D_{IR}(\tilde{\nu}, k) = S_{sample}(\tilde{\nu}) - k.S_{medium}(\tilde{\nu}). \tag{4.7}$$

The k was value kept constant for each spectrum in the sample dataset. Using arbitrary integration limits $\tilde{\nu_1}$ and $\tilde{\nu_2}$, the integrated absorbance of a spectrum before and after the subtraction is related by

$$\int_{\tilde{\nu_1}}^{\tilde{\nu_2}} D_{IR}(\tilde{\nu}, k)d\tilde{\nu} = \int_{\tilde{\nu_1}}^{\tilde{\nu_2}} S_{sample}(\tilde{\nu})d\tilde{\nu} - C \tag{4.8}$$

where

$$C = k \int_{\tilde{\nu_1}}^{\tilde{\nu_2}} S_{medium}(\tilde{\nu})d\tilde{\nu}. \tag{4.9}$$

This means that each element of an integrated absorbance image generated after the spectral subtraction would simply be linearly offset by C, allowing the comparison of absorbance images whether or not a cell medium spectrum had been subtracted. However, this approach had the disadvantage that contributions from cell medium would not be optimally subtracted from each the spectrum in the spectroscopic imaging dataset. The k value was chosen to avoid over-subtraction in the spectra corresponding to cell. Figure 4.9 shows the result of the cell medium subtraction.

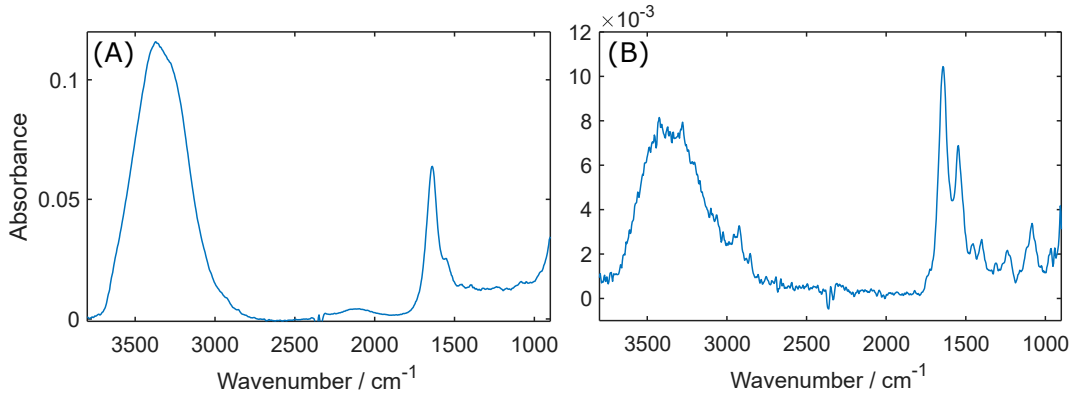


Figure 4.9: Spectrum recorded from one FPA pixel before (A) and after (B) cell medium subtraction.

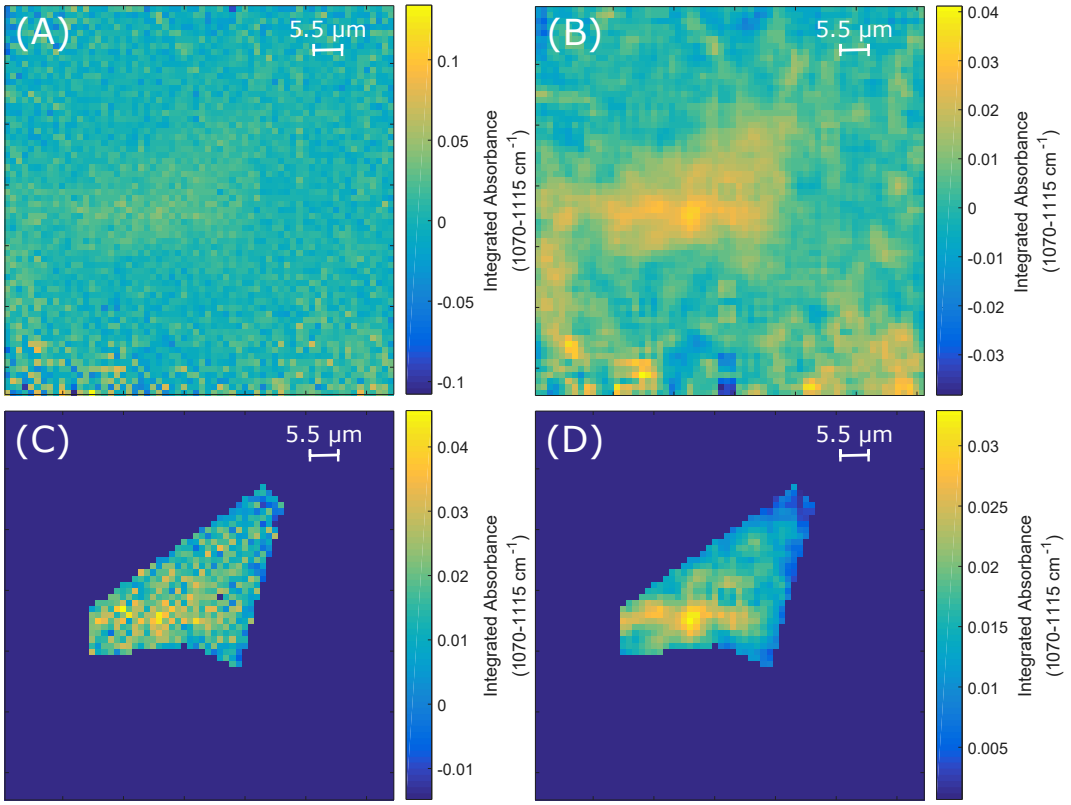


Figure 4.10: Integrated absorbance images of phosphate I before (A) and after (B) a 3×3 box filter is applied to the image. Image (C) and (D) are (A) and (B) respectively, with image area corresponding to cell medium discarded

As can be seen from figure 4.9, the absorbance of the phosphate I band at 1080 cm^{-1} is the strongest band corresponding to nucleic acids, and is therefore the most likely band to generate an integrated absorbance images with good signal to noise. Figure 4.10A shows the result of integrating phosphate I. The distribution of phosphate I cannot be easily distinguished above noise. Figure 4.10B shows the phosphate I integrated absorbance image after applying a box filter. Whilst now the chemical distribution can be more easily seen there is still significant noise distorting the image.

To avoid this problem, the image area known to contain cell was isolated by setting the image area containing cell medium to zero. Cells near the border of the image were also ignored. Figure 4.10D shows the improved visualisation of the nuclear region once the image has been subjected to a box filter and cell medium spectra are removed. There is no sharp border between the nucleus and the cytoplasm or perinuclear area, which is expected to be because the phosphate I band has contributions from both DNA and RNA. However, it is possible to see lineshape variations in the phosphate I band in the nuclear region versus the cytoplasm. Figure 4.11 shows averaged spectra from two regions of the cell compared to an average

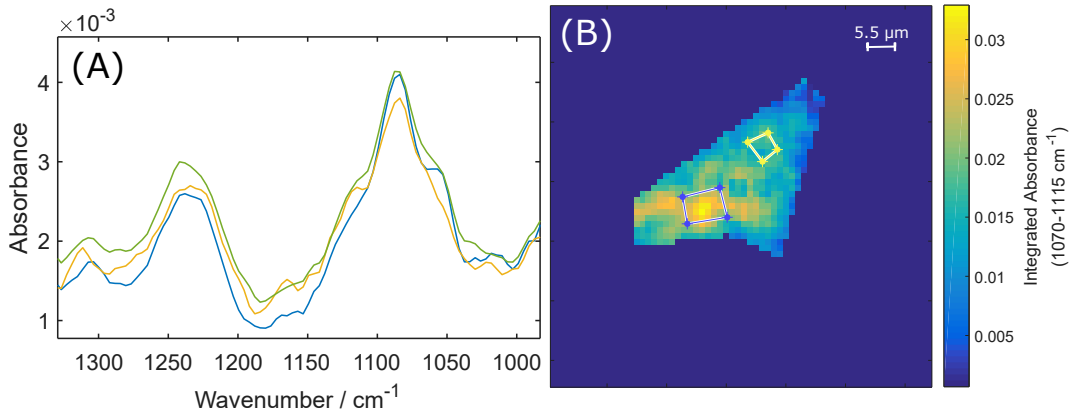


Figure 4.11: Plot (A) shows spectra illustrating the difference in lineshape of the phosphate I band in different regions of the cell. The yellow and blue spectrum correspond to the cytoplasm and nucleus respectively. The green spectrum was generated by averaging the whole cell. Image (B) shows the integrated absorbance of phosphate I with the area known to correspond to cell medium discarded. The blue and yellow squares indicate the area averaged to generate the spectra seen in plot (A).

spectrum from the whole cell. The region proposed to be the nucleus has a strong shoulder at 1050 cm^{-1} but not at 1120 cm^{-1}, with good agreement to the spectra of extracted nuclei presented in Zucchiatti et al. (2016). The strong band at 1050 cm^{-1} is characteristic of double stranded DNA, whilst the band at 1120 cm^{-1} was shown to be mostly due to RNA. The averaged spectrum from the region proposed to be the cytoplasm shows the reverse, a large absorbance at the shoulder 1120 cm^{-1} and a much lower absorbance at 1050 cm^{-1}. The averaged spectrum of the phosphate I region from the whole cell also shows good agreement with average spectrum from whole cells reported by Zucchiatti et al. (2016).

4.3.5 Visualising other Sub-Cellular Regions

Two methods have previously been reported to visualise other subcellular features in FTIR spectroscopic imaging. The ratio between CH_2 at 2925 cm^{-1} and CH_3 at 2960 cm^{-1} has been reported to distinguish the nuclear, perinuclear, and cytoplasm in cells (Sandt et al., 2013; Clède et al., 2014). This was attempted, as shown in figure 4.12A, but no obvious distribution can be seen. As the depth of penetration of the evanescent field is around 0.5 µm in this region, it is anticipated that the signal to noise level isn't sufficient.

The second method was proposed by Kuimova et al. (2009). The spectroscopic band at 1023 cm^{-1} was assigned to glycogen and it was noted that the endoplasmic region is glycogen rich. Previous studies have also assigned glycogen to bands at

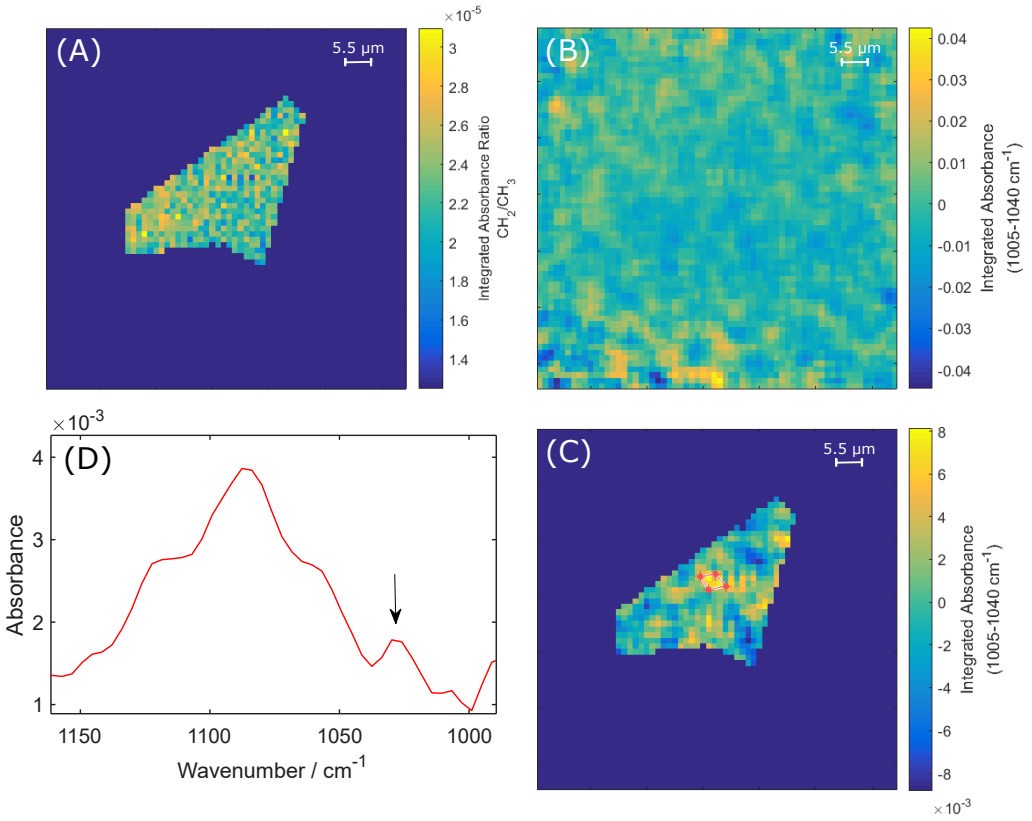


Figure 4.12: (A) Image of the integrated absorbance ratio between the CH_2 and CH_3 bands. (B) Integrated absorbance image of the glycogen band at 1030 cm^{-1}. Image (C) is identical to image (B), except the image area corresponding to cell medium has been removed. (D) Average spectrum generated from the red square indicated in image (C).

1028 cm^{-1} (Gazi et al., 2003) or 1030 cm^{-1} (Chiriboga et al., 1998). Figure 4.12B shows the integrated absorbance image generated using the limits 1005 cm^{-1} and 1040 cm^{-1}, after a 3×3 box filter was then applied to the image. It can be seen that noise from the outer edges dominates the image. Figure 4.12C shows the same integrated absorbance image with the image area near the border or known to correspond to cell medium discarded. The distribution of glycogen can now be seen, with a high absorbance region adjacent to the nuclear area. Figure 4.12D shows a spectrum generated from averaging the region within the red square shown in 4.12C, illustrating a clear peak at 1030 cm^{-1} not present to the same degree in figure 4.11. In the data presented by Kuimova et al. (2009) no water subtraction was carried out before the band assignment. In addition, a baseline distortion can be seen on the left side of the spectrum shown in figure 4.1. It is likely that these two factors are the cause of the different band position previously reported compared to what is shown in this work.

4.4 Conclusion

This chapter presents germanium ATR-FTIR spectroscopic images of live cells. It was found not possible to repeat measurements of live cells by the method reported in (Kuimova et al., 2009). Specifically, it was found not possible to generate images with sufficient signal to noise to distinguish cells from cell medium with the number of scans reported. The integrated absorbance images also required further image processing to visualise the distribution of the phosphate I band between 1040-1140 cm^{-1} and the glycogen band at 1030 cm^{-1}. The absorbance from spectral measurements of cells presented in this chapter also appear to be about four times lower than previously reported for micro ATR-FTIR imaging with a germanium accessory.

A number of improvements to the initial methodology have also been presented. A PDMS chamber that does not require glue along with an efficient way to remove spectral contributions from water vapour in the sample spectrum made experiments more reproducible. Ozone/UV cleaning was also found to be an effective way to improve the wettability of germanium, which improved cell adhesion to the germanium crystal surface.

For the first time, it has been demonstrated from a single infrared spectroscopic imaging dataset that different lineshapes of the phosphate I band at 1080 cm^{-1} can be seen across the cell. The nuclear region shows relatively low contributions of RNA and high contributions of DNA, shown by a low absorbance of the shoulder at 1120 cm^{-1} and a high absorbance of the shoulder at 1060 cm^{-1}. Conversely, the cytoplasm shows high RNA signal and low DNA signal, shown by a high absorbance of the shoulder at 1120 cm^{-1} and a low absorbance of the shoulder at 1060 cm^{-1}. Results also indicate that glycogen distribution can be used to visualise the endoplasmic reticulum. A peak at 1030 cm^{-1} was identified, which is in good agreement with glycogen bands reported in previous works.

5 ATR-FTIR Spectroscopy and Spectroscopic Imaging for Drug Detection in Living Cells

This chapter presents the application of both ATR-FTIR spectroscopy and spectroscopic imaging to detect a model drug within living cells. The drug chosen was a rhenium tris-carbonyl derivative, which was synthesised and kindly provided by Clotilde Policar's group.

The first part of this chapter will describe the work undertaken to set up the methodology for multiple-reflection ATR-FTIR spectroscopy of live cells, and then its subsequent use to detect drug accumulation in a cell population. The last section describes the investigation of the ability of micro ATR-FTIR spectroscopic imaging to detect the same drug in a single cell, and the extent to which subcellular localisation can be observed. This section uses the methodology developed in chapter 4.

5.1 Introduction

Transition metal-carbonyl functional groups consist of carbon monoxide ligands bonded with a transition metal atom. The bond between CO and the metal atom involves a weak sigma bond and pi back-bonding. The CO ligand donates a lone pair to form the sigma bond and the metal atom back donates from a d orbital to a CO anti-bonding molecular orbital. The interaction with the anti-bonding molecular orbital of CO reduces the bond order of the CO ligand, and thus the vibrational frequency of the CO stretching mode, ν(CO). This means that infrared spectroscopy can be used to determine the strength of pi back-bonding in transition metal complexes. The ν(CO) bands for most metal-carbonyl groups fall within the 2100-1700 cm^{-1} range, compared to 2148 cm^{-1} for gaseous CO. There are very few infrared vibrational transitions seen in this region.

Another advantage of using a metal-carbonyl derivative compound is that the

ν(CO) vibrational mode gives rise to some of the most intense absorbance bands seen in infrared spectroscopy. As a consequence of pi back-bonding between the CO ligand and the metal atom, the CO bond is both more polarised and has a higher electron density than seen in a normal carbonyl functional group. This means a particularly large change in molecular dipole moment is seen as a function of the ν(CO) mode, leading to a strong interaction with infrared light of the correct frequency.

The convenient position of the metal-carbonyl ν(CO) bands and their high molar absorptivity lead to interest in their development as infrared probes. The first example of this was the development of estrogen receptor assays, which were as sensitive as the alternative radiolabelled assays (Jaouen et al., 1985). Metal-carbonyl labelling of steroid hormone derivatives allowed the assessment of estrogen receptor number, an important marker in breast cancer (Jaouen and Vessières, 1985). Quantitative assays were developed later and metal-carbonyl labelled analytes dissolved in carbon tetrachloride have been detected by infrared spectroscopy in concentrations as low as 300 fM (Salmain et al., 1992, 1991).

Metal-carbonyl complexes have also been employed as infrared imaging probes. Kong et al. (2007) first showed that water soluble metal-carbonyls could be detected within dried cells by FTIR spectroscopic imaging. The Policar group has also developed a variety of metal-carbonyl derivatives for multimodal imaging studies (Clède and Policar, 2015). Figure 5.1 shows one example of a rhenium tri-carbonyl derivative they developed, which will be referred to henceforth as compound **1**. This compound was kindly provided for the work undertaken in this chapter. In addition to the strong infrared signature of compound **1**, it also has the advantage of being luminescent (Clède et al., 2012b). Fluorescence imaging showed that the drug accumulated in the Golgi apparatus of cells. In the same study, compound **1** was also detected in a single fixed cell by FTIR micro-spectroscopy combined with a synchrotron source. More recently, FTIR spectroscopic imaging using a multibeam synchrotron source also detected the same drug (Mattson et al., 2013). A similar rhenium tri-carbonyl derivative, which was an analogue to the drug tamoxifin, has also been detected in fixed cells by FTIR micro-spectroscopy using a synchrotron source (Clède et al., 2012a) and with photothermally induced resonance infrared (PTIR) mapping (Policar et al., 2011).

Although multiple-reflection ATR-FTIR spectroscopy has been successfully used to detect drug accumulation in a living cell population (Chan and Fale, 2014), drug detection by FTIR spectroscopic imaging in live cells has so far not been reported.

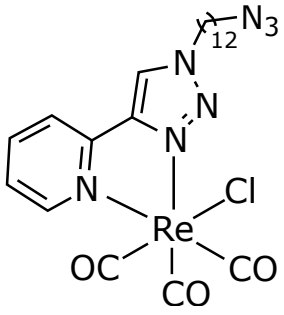


Figure 5.1: Schematic of the chemical structure of the metal-carbonyl based compound, kindly provided by the Policar group. Referred to in the text as compound 1

5.2 Multiple-Reflection ATR-FTIR Spectroscopy

5.2.1 Sample Preparation

HEK 293a cells were subcultured as detailed in section 3.1.1 until centrifugation. The cell pellet was then resuspended in L-15 cell medium, which doesn't require a 5% CO_2 environment. Cells were counted using a haemocytometer to establish the cell density. Compound **1** was dissolved in DMSO to a final concentration of 5 mM to form a stock solution.

5.2.2 Instrument Setup

The instrument settings were optimised as detailed in chapter 3. A Specac Gateway™ ATR accessory equipped with a trough top-plate was used for these experiments. The accessory was heated for two hours prior to the background measurement, after which 1 ml of L-15 cell medium was added to the top plate and heated for 1 hour to ensure the cell medium was at 37°C. Once the cell medium was at the correct temperature a cell suspension was added to a final density of 2×10^5 cells ml^{-1} and covered. All infrared measurements coadded 512 scans at 2 cm^{-1} spectral resolution. 16 hours after seeding, compound **1** was added to the medium. To do this, 200 µl of medium was removed from ATR accessory, 5 µl was removed and then 5 µl of compound **1** stock solution was added. The mixture was re-added dropwise to the ATR accessory.

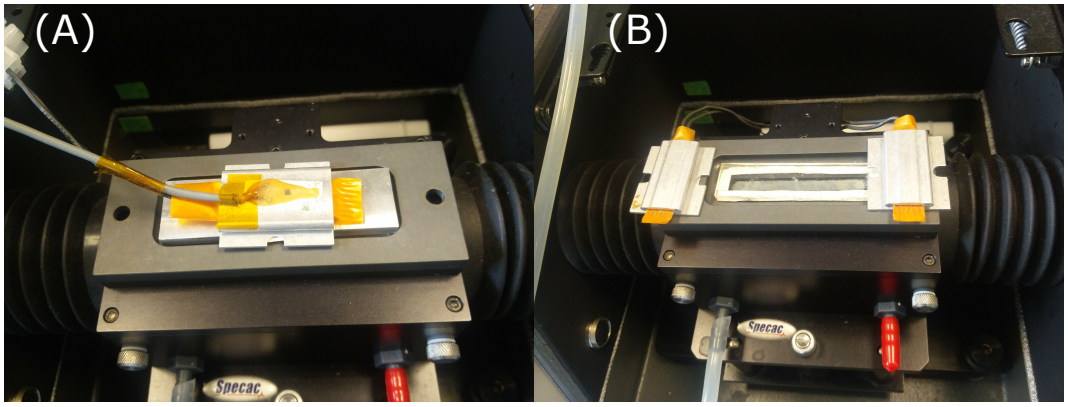


Figure 5.2: Illustration of the two setups to heat the multiple-reflection ATR accessory. Picture (A) shows the use of a heated aluminium lid. A PDMS spacer is between the aluminium lid and the ATR accessory to create a seal. A platinum temperature sensor is attached to the heater directly. Picture (B) shows the setup to heat the accessory directly. Two 20 W heaters and the temperature sensor were attached to the ATR top-plate. An acetate lid and PDMS spacer was used to create a seal.

5.2.3 Heating System

An in house heating system was built for these experiments. The heater used a PID controller with a thin film platinum resistance temperature sensor to control enclosed heating elements. Two methods of heating the top plate were attempted, as shown in figure 5.2. For the set up shown in figure 5.2B, the sensor and two 20 W heating elements were attached to the top plate with heat sink tape. To stop medium evaporating away during the experiment, a PDMS spacer and an acetate lid were made using a laser cutter. When downward pressure was applied using a small weight, the trough was effectively sealed. In the other approach, illustrated in figure 5.2A, an aluminium lid was used and the lid itself was heated using a 50 W heating element. The sensor was attached directly to the heating element. The PID controller was set to the temperature that would ensure the cell medium in the accessory's trough was kept at 37°C. This was 60°C when heating the lid and 45°C when heating the top plate directly.

5.3 Results and Discussion

5.3.1 Multiple-Reflection Accessory

It was found that when the top plate was heated directly the cell culture could not be kept alive for the required time. Figure 5.3 shows that initially, upon seeding cells onto the surface of the germanium crystal, cells could not be distinguished from cell

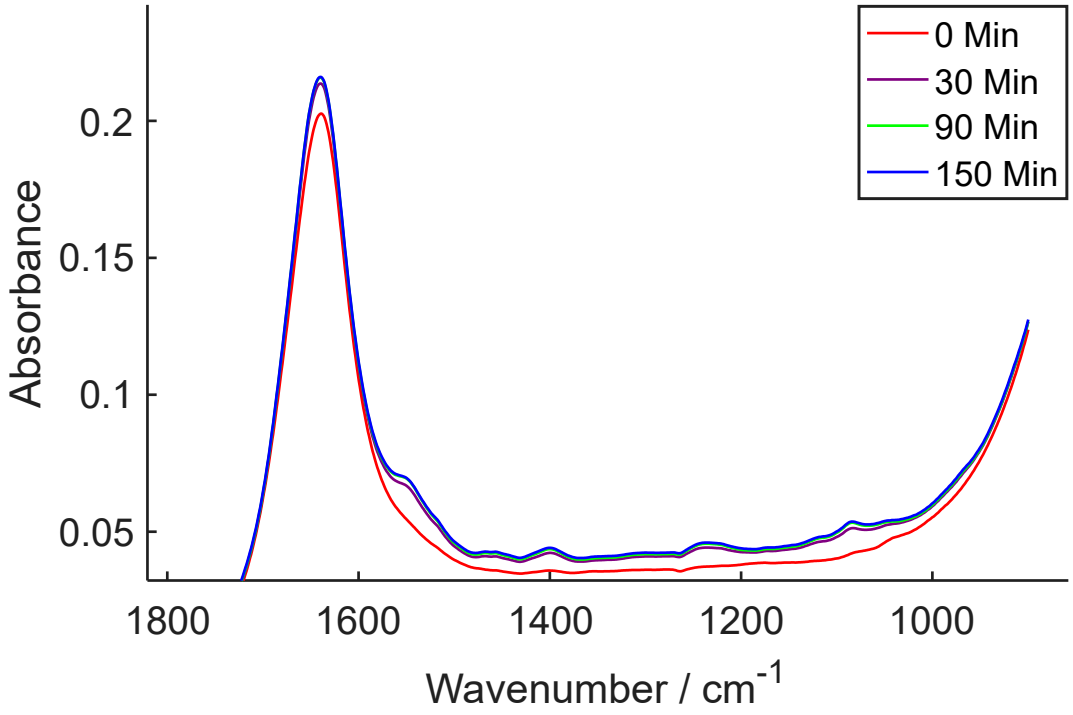


Figure 5.3: Spectral kinetic illustrating the increase in absorbance of bands corresponding to cells as the cell population adheres to the germanium ATR crystal surface

medium, but as cells start to adhere to the surface, infrared bands corresponding to cells can be seen. From 90 minutes onwards, no increase in amide II could be seen. Cells were then left for 12 hours and the amide II absorbance decreased, as shown in figure 5.4A. The accessory top plate was removed and cell viability was tested using trypan blue. As can be seen from figure 5.4B, most of the cells in the field of view of the microscope were found to be dead.

Figure 5.4 part C and D show that when the aluminium top plate was used cells remained viable after 16 hours. However, the limited increase in amide II absorbance from 90 minutes onwards indicates that the cell culture was not growing as normal. This is expected to be a combination of the effects from using a different cell medium and the surface properties of germanium.

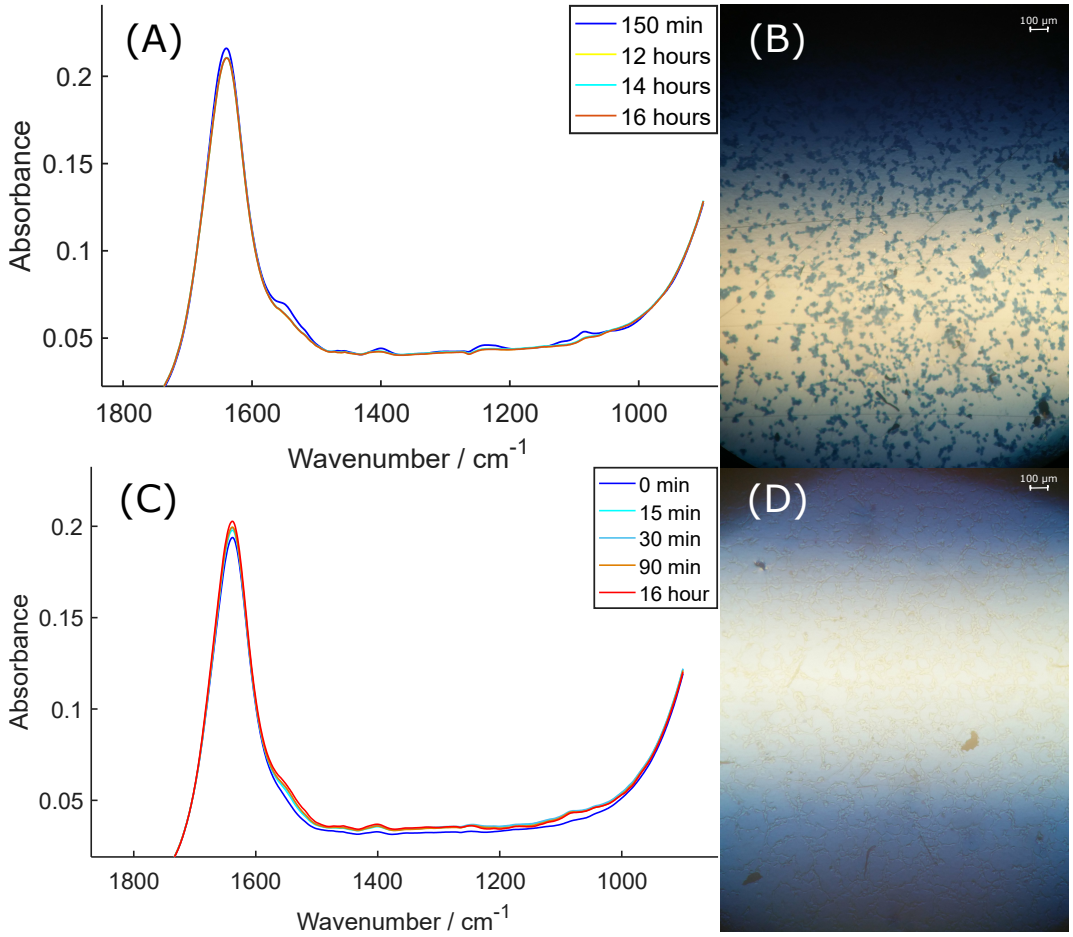


Figure 5.4: Spectral kinetic (A) and picture (B) show that cells were found to be mostly dead after 16 hours when the ATR top-plate was heated directly. Spectral kinetic (C) and picture (d) indicate that, although showing limited growth, cells remained viable 16 hours when the heated top plate was used.

5.3.2 Cell Tolerance to DMSO

5-flurourical was the drug used to demonstrate that multiple-reflection ATR-FTIR was capable of detecting drug accumulation in living cells (Chan and Fale, 2014). This drug is relatively water soluble so the stock solution and subsequent dilutions could be made using cell medium alone. However most drugs are not very water soluble. In particular, compound **1** used for this work required dissolution in DMSO before subsequent dilution into cell medium. Cells were first subjected to DMSO only, so that effects due to DMSO exposure could be distinguished from compound **1**. As can be seen from figure 5.5, upon addition of DMSO to a percentage volume of 1%, there is an immediate reduction in the spectroscopic bands due to cells which did not recover. Fortunately, when cell viability was tested, the majority of cells were still found to be alive.

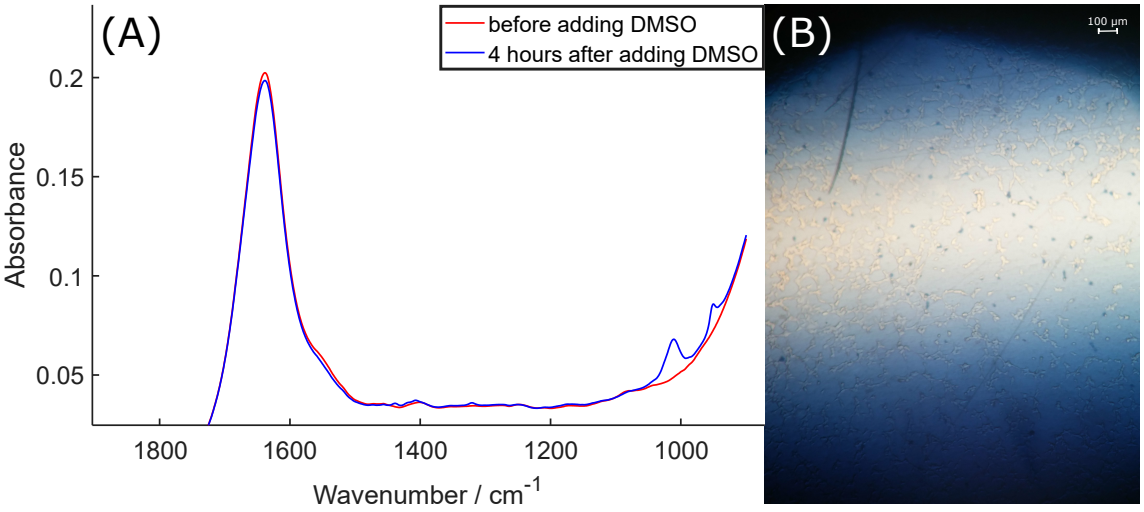


Figure 5.5: (A) Spectra illustrating the reduction in spectral band absorbance as a result of adding DMSO. Picture (B) shows cell exposure to trypan blue after the experiment, indicating cells are still viable 4 hours after DMSO addition

5.3.3 Detecting the Cellular Uptake of Metal-Carbonyl Derivative

Having setup the methodology for multiple-reflection ATR-FTIR spectroscopy of live cells, a cell population adhered to the ATR crystal was exposed to compound **1**. Within 10 minutes of adding compound **1**, to a final concentration of 25 µM, a doublet centred at 1915 cm^{-1} and a singlet peak at 2015 cm^{-1} could be detected, as shown in figure 5.6. These have been previously assigned as the E-band and A_1-band, corresponding to the asymmetric and symmetric metal-carbonyl stretching

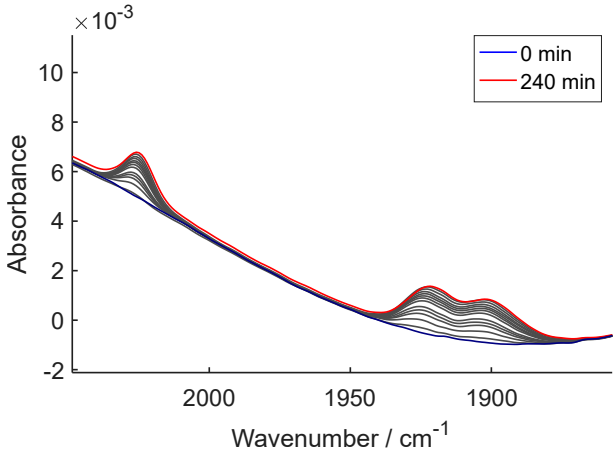


Figure 5.6: Spectral kinetic from a multiple-reflection ATR-FTIR experiment. The increase in absorbance of metal-carbonyl bands can be seen, indicating an accumulation of the metal-carbonyl derivative compound within cells.

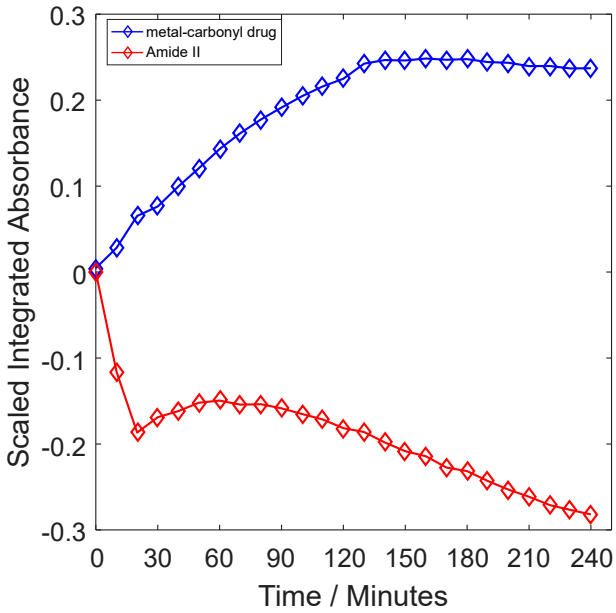


Figure 5.7: Integrated absorbance of amide II and the A_1-band versus time. The absorbance kinetics have been vector normalised to more easily view the two profiles together.

mode, respectively (Clède et al., 2012b).

Upon adding compound **1**, there is an immediate reduction in the absorbance of spectroscopic bands corresponding to cells, as can be seen from figure 5.7 and 5.8, which is expected to be caused by DMSO. The DMSO concentration near the germanium surface can then be seen to decrease, as it diffuses into the cell medium bulk. From 20 minutes to 60 minutes there is a also subsequent increase in spectroscopic bands due to cells. It is expected that the cell's environment becomes less stressful as the local concentration of DMSO decreases, and this accounts for the slight improvement in cell adhesion between 20-60 minutes. From 60 minutes onwards there is a continual decrease in the spectroscopic bands of cells and this is probably caused by drug accumulation rather than DMSO.

As shown in figure 5.7, the absorbance of drug increases linearly until 150 minute, where it plateaus. It is expected that drug continues to accumulate within the cell population beyond this, but at 60 minutes the cell starts to show signs of stress due to the accumulation of the drug itself. The decreasing contact of cells with the ATR crystal surface could offset the increasing presence of drug within the cell. This is further evidence that that the drug is accumulating within the cell and not on the ATR crystal surface. The results seen also indicate the optimal parameters for a spectroscopic imaging experiment. The optimal incubation time would be 2 hours for the best chance of detecting the drug, however 1 hour would be the optimal incubation time to detect the cell itself.

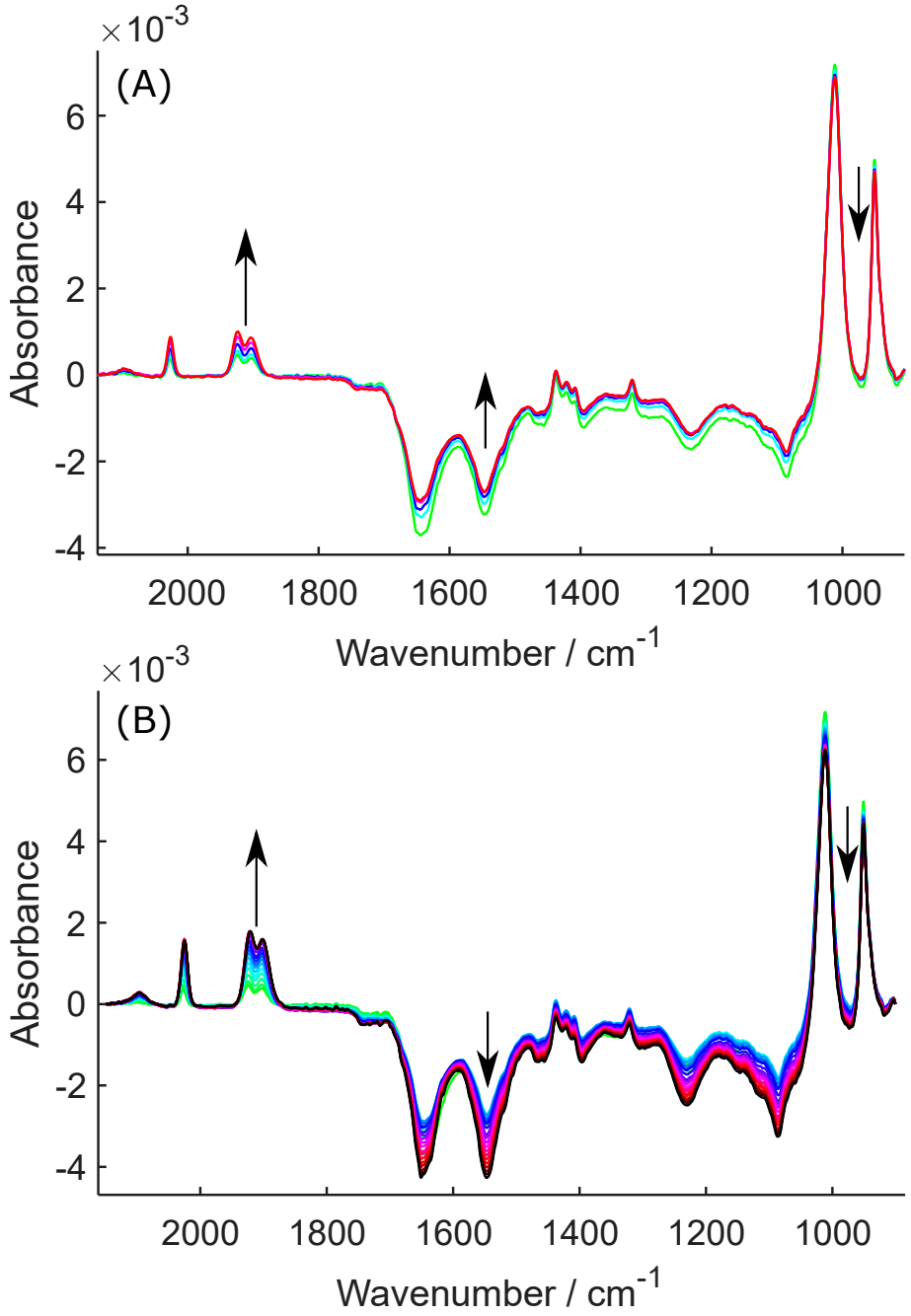


Figure 5.8: Spectral kinetic illustrating the spectral band changes within the first 60 minutes (A) and 60 minutes onwards (B)

5.3.4 Metal-Carbonyl Band Shift

Closer examination of the metal carbonyl bands indicates a shift to lower wavenumber during the experiment. As can be seen from figure 5.9, a shift of around 5 cm^{-1} can be seen in the E band. As compound **1** contains amine groups it is speculated that the local environment of compound **1** is becoming more alkaline throughout the experiment. This would lead to deprotonation of amine groups, increasing the

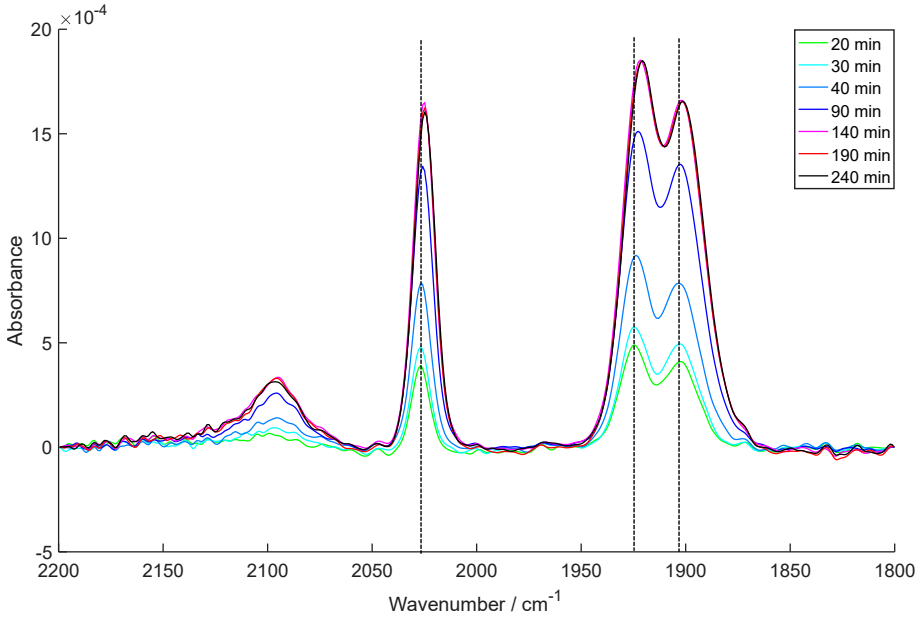


Figure 5.9: Spectral kinetic illustrating the shift to lower wavenumber of the metal-carbonyl bands

strength of pi back-bonding, and could potentially be the cause of the slight shift to lower wavenumber (Anson et al., 1996).

5.4 Germanium ATR-FTIR Spectroscopic Imaging

5.4.1 Instrument Settings

As conducted previously in chapter 4, all measurements were carried out using 8 cm^{-1} spectral resolution and 1024 scans were coadded. The interferometer speed was set to 5 kHz and each measurement took 20 minutes.

5.4.2 Experimental Setup

The method development behind micro ATR-FTIR spectroscopic imaging of live cells is detailed in chapter 4. Cells were seeded onto the germanium crystal, after a background measurement was taken, and left to incubate for 20 hours. Cells were then imaged to determine if they could be detected spectroscopically, which often was not the case. Cell medium was then aspirated from the chamber and replaced with a 25 µM solution of compound **1** in cell medium. The accessory was then incubated for between 40 minutes and 120 minutes before the sample measurement was taken.

5.5 Results and Discussion

5.5.1 Cell Detection

In addition to the markedly lower signal to noise compared to multiple-reflection ATR-FTIR, spectroscopic imaging experiments had the initial difficulty of inverting the accessory and mounting it onto the objective before measurements could be taken. This disturbance became much more likely to dislodge cells once they were under stress caused by the presence of compound **1** and DMSO. Cell cultures incubated with compound **1** longer than 1 hour consistently detached from the germanium crystal surface once the accessory was inverted. The maximum time cells could be incubated with the drug and remain detectable on the germanium surface was 40 minutes. Figure 5.10 shows amide II integrated absorbance images of cells before incubation and 40 minutes after incubation. As the sample measurement itself takes 20 minutes the image represents cells exposed to compound **1** for between 40-60 minutes. As can be seen from the absorbance images, the cell morphology is markedly different after incubation. Cells appear smaller and, as can be seen from the scale in figure 5.10, the integrated absorbance is lower, indicating their contact with the surface has decreased. In both images five cells can be seen, but it is not certain if the cells from the right and left images are the same, as it is not known how far cells would move in a 40 minute time frame.

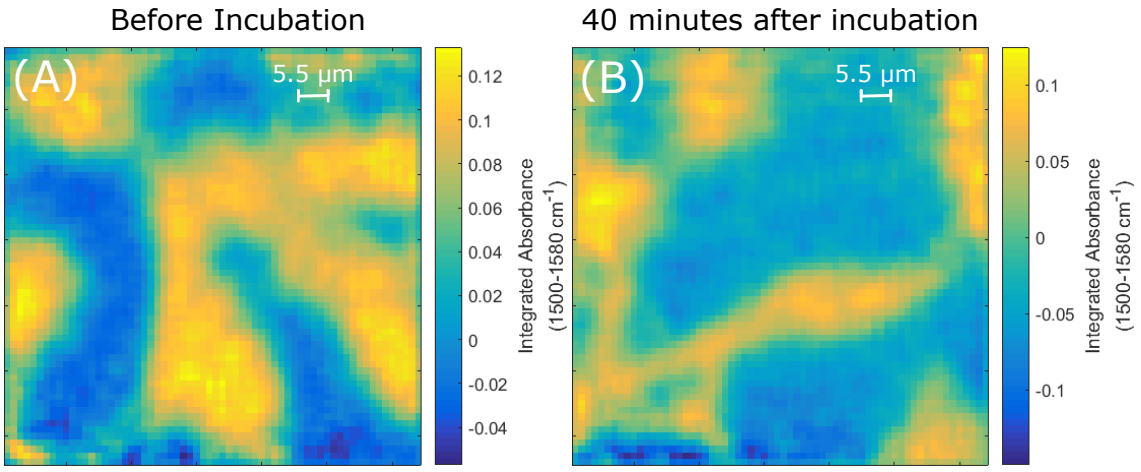


Figure 5.10: Integrated absorbance image using the amide II band showing cells (A) before and (B) 40 minutes after incubation with compound 1

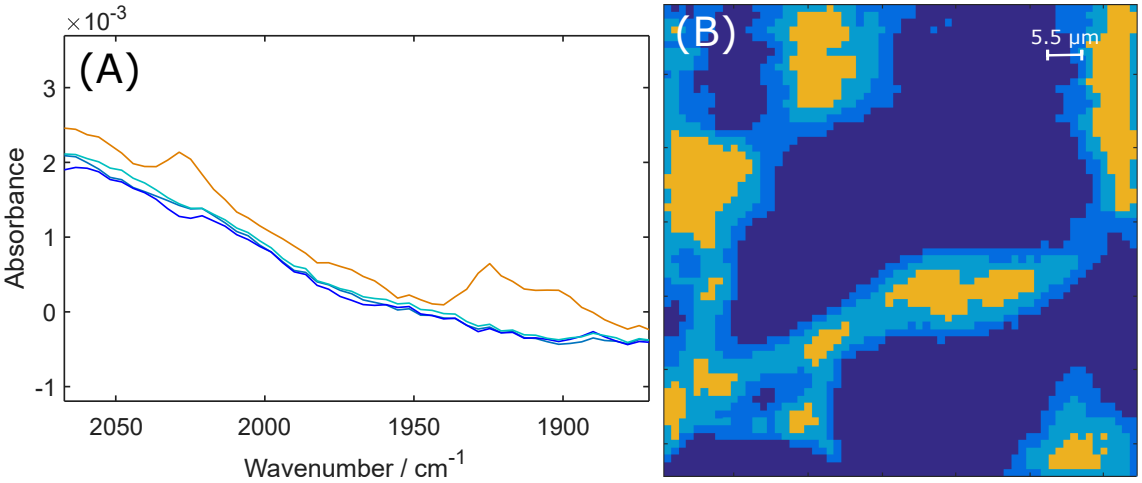


Figure 5.11: k-means clustering of the Amide II integrated absorbance image. Each colour represents membership to a distinct cluster. The spectra in plot (A) show the average spectrum from each cluster in image (B) of the corresponding colour.

5.5.2 Drug Detection

To test for the presence of the drug, k-means clustering of the amide II absorbance band was carried out to separate cell, cell border, and cell medium area of the image. The average spectrum from each cluster was then taken. As can be seen from figure 5.11, there is no evidence of the drug present within the cell medium or the outer edge of the cell. However, the A-$_1$ and E metal carbonyl band can both be seen within the orange cluster, corresponding to the middle of the cell.

5.5.3 Sub-Cellular Localisation

As was demonstrated in chapter 4, isolating the pixels corresponding to one cell near the middle of the image, where the illumination of the ATR crystal is best, can greatly aid image analysis. It is known from previous work that compound **1** localises in the Golgi aparatus of cells. As there was no reliable infrared spectral signature for the Golgi aparatus, this could not be verified directly with ATR-FTIR spectroscopic imaging. However, it is possible to verify if the drug is accumulating in the perinuclear region of the cell.

Figure 5.12 shows integrated absorbance images of the band corresponding to metal-carbonyl E band and the phosphate 1 band of one isolated cell. The E-band integrated absorbance image doesn't show a clear distribution. However the nuclear region of the cell can still be visualised with the phosphate 1 band integration. The nuclear region indicated by the blue square in figure 5.12 was averaged and the cell

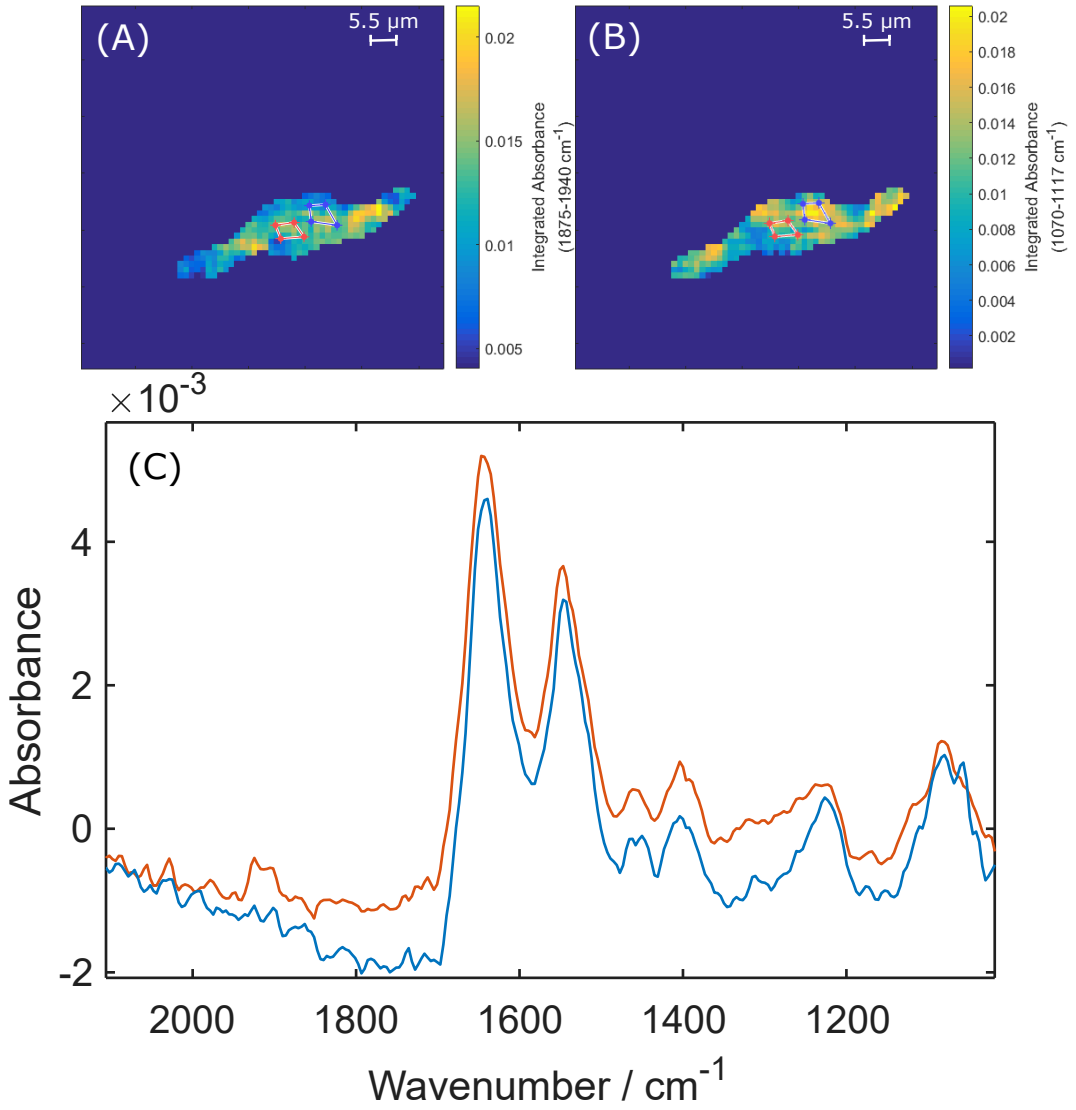


Figure 5.12: Integrated absorbance images generated using the metal-carbonyl E band (A) and the cell's phosphate I band (B). The red and blue spectrum in plot (C) shows the average spectrum from the red and blue marked regions indicated in both images (A) and (B).

medium spectrum was subtracted. The medium spectrum was obtained by averaging the image area known to correspond to cell medium. The same was done for the region indicated in the red square, which is thought to be the perinuclear region. The result is shown at the bottom of figure 5.12. As can be seen, the phosphate 1 band from the nuclear region spectrum shows a lineshape consistent with the nucleus shown earlier in chapter 4. No presence of compound **1** can be seen in the infrared transparent window. However compound **1** can be seen in the averaged spectrum from the perinuclear region. The E-band can be clearly resolved, although the A_1 band cannot be easily distinguished above the noise.

5.6 Conclusion

This chapter demonstrates that ATR-FTIR-spectroscopic imaging is capable of detecting drugs within living cells. Multiple-reflection ATR-FTIR spectroscopy of live cells was shown capable of detecting accumulation of a metal-carbonyl derivative compound within 10 minutes of exposure despite the negative effects of DMSO. The drug was shown to start affecting cell contact with the surface of the crystal within 60 minutes. The maximum level of compound **1** was detected 120 minutes after the initial addition to the cell medium. A small shift was also seen in the metal carbonyl band, perhaps indicating a local change in pH in the Golgi apparatus, where the compound is known to accumulate.

Micro ATR-FTIR spectroscopic imaging was also shown to be capable of detecting metal-carbonyl groups within cells. It was found that cells could not be detected if exposed to the drug for more than 40 minutes, and large distortions to the imaged cells' morphology can be seen from the amide II integrated absorbance image. K-means cluster analysis demonstrated that accumulation of the drug was not seen in the cell medium or near the border of the cell. The nuclear region of the cell also showed no signs of the presence of compound **1**, whereas the perinuclear region did. The signal to noise was found to be insufficient to generate a convincing integrated absorbance image of the metal-carbonyl distribution, but metal-carbonyl bands could be seen when regions of pixels were averaged.

6 Two-Dimensional Correlation Analysis to Investigate Molecular States of Water in Living Cells

This chapter presents the application of 2D correlation analysis to investigate the extent to which different molecular states of water can be seen in living cells. This form of multivariate analysis allowed further insight to be drawn from datasets collected using the methods developed in chapter 4 and 5. Section 6.1 will summarise the literature on the infrared band sub-structure of water's OH stretching mode and its sensitivity to hydrogen bonding. The procedure to calculate disrelation maps from spectroscopic imaging datasets will also be discussed. In section 6.3.1 2D correlation analysis is carried out to establish the synchronous and asynchronous character of the dynamic infrared spectrum of water perturbed by temperature. The same analysis of cell adhesion to a ZnSe crystal is carried out in section 6.4. Finally, disrelation analysis and disrelation mapping of ATR-FTIR spectroscopic images of live cells, similar to that published in (Shinzawa et al., 2017), is presented.

6.1 Introduction

Although hydrogen bonds cannot be directly detected in mid-infrared spectroscopy, it is known that the OH stretching band of water is highly sensitive to its hydrogen bonding environment (Brubach et al., 2005). One water molecule can engage in between zero and four hydrogen bonds with its neighbours, and the restoring force of the OH stretching vibration is weakened with the increasing number of hydrogen bonds. This leads to a decrease in vibrational frequency with increasing participation in hydrogen bonding. The lineshape of water's OH stretching band is often interpreted as a superposition of 3 sub-bands, each reflecting a different hydrogen bonding environment of water.

However, even when looking at pure water, studies have reached different conclusions as to the correct number of sub-bands. Most infrared experiments investigating

the effect of temperature on the infrared spectrum of water determine that the OH stretching band is best decomposed into three gaussian components (Brubach et al., 2005; Bergonzi et al., 2014). These are normally referred to free, intermediate, and coordinated water, although the reported peak positions vary. Virtually the same experiment using Raman spectroscopy reports 5 sub-bands (Sun, 2009), which has been used in subsequent Raman studies (Choe et al., 2016).

Studies have also shown that infrared spectroscopy is capable of differentiating bulk water from water associated with membranes (Binder, 2007), or inorganic surfaces (Yalamanchili et al., 1996). Generally these studies also determine that three sub-bands best describes the overall OH stretching band's lineshape, and simply note different distributions of the three same gaussian components. Different sub-bands can be observed when water is not the bulk solvent. For instance when water is dissolved in ionic liquids, bands at 3640 cm^{-1} and 3560 cm^{-1} can be seen (Cammarata et al., 2001). The effects of salts in aqueous electrolyte solutions also give rise to different molecular states of water (Kitadai et al., 2014).

2D correlation analysis has been used to investigate hydrogen bonding systems, taking advantage of the increased spectral resolution to examine the sub-band structure. Hetero-correlation analysis was performed on mid-infrared with near-infrared spectra of water (Boguslawa et al., 2005). This was done to examine the synchronous and asynchronous changes seen in the dynamic spectrum of water as a function of temperature. One advantage of 2D correlation analysis is that no prior assumption of the number of sub-bands needs to be made. This study, along with 2D correlation analysis of water diffusion into polymers, also reached the same conclusion of 3 sub-bands (Wu and Siesler, 2003).

To date there is a single study investigating the OH stretching band in live cells, which used Raman micro-spectroscopy (Tiwari et al., 2013). By using non-negative matrix factorisation (NNMF), they determined five distinct OH stretching band lineshapes.

In infrared spectroscopy water's OH stretching mode has a stronger absorbance than the OH bending mode. In transmission mode experiments, even at path lengths of 10 µm, the OH stretching region of the infrared spectrum is saturated. This is normally overlooked as the fingerprint region contains the main spectroscopic bands of interest. This means any information about the hydrogen bonding environment of water is lost in these datasets. The advantage of infrared spectroscopic imaging in ATR mode is the the OH stretching region of the spectrum is not saturated, and thus can be recorded with much greater signal to noise.

6.2 Methods

6.2.1 Sample Preparation

HEK 293a cells were subcultured as detailed in section 3.1.1 until centrifugation. The cell pellet was then re-suspended in L-15 medium, which doesn't require a 5% CO_2 environment. Cells were counted using a heamocytometer to establish the cell density.

6.2.2 Experimental Setup

For multiple-reflection ATR-FTIR measurements, the instrument settings were optimised as detailed in chapter 3. A Specac Gateway™ ATR accessory, equipped with a trough top-plate, was used for these experiments. A ZnSe multiple-reflection crystal was used and the accessory was not heated. 1 ml of L-15 cell medium was added to the trough after a background measurement had been taken. Cells were seeded onto the surface and measurements were taken every 10 minutes for 4 hours. In all measurements 512 scans were coadded at 2 cm^{-1} spectral resolution.

To obtain spectra of water at various temperatures the same multiple-reflection accessory was used but with a germanium multiple-reflection ATR crystal. Water was added to the crystal surface and covered by the heated top plate described in chapter 5. Water was heated from room temperature to 40 degrees. Measurements were taken every 2 minutes for 40 minutes. In all measurements 512 scans were coadded at 2 cm^{-1} spectral resolution.

The procedure for obtaining spectra of live cells using ATR-FTIR spectroscopic imaging is detailed in chapter 4.

6.2.3 2D Correlation Analysis

The theory behind 2D correlation analysis is detailed in section 2.8, which describes how to calculate the synchronous and asynchronous intensity, in discrete and continuous perturbation space, between two spectral variables. Linear algebra allows one to calculate the synchronous correlation between all frequencies with one equation. The set of spectra first needs to be arranged into a single matrix, where each column corresponds to a discrete wavenumber, and each row represents a sample measurement. This is known as the dynamic spectrum $\tilde{Y}$. The synchronous spectrum is then calculated by the following following matrix equation.

$$\Phi = \frac{1}{m-1}\tilde{Y}^{\top}\tilde{Y} \tag{6.1}$$

which denotes matrix multiplication of the dynamic spectrum with its transpose, and then the division of each element in the resulting matrix by the number of samples in the dynamic spectrum. The whole asynchronous spectrum can be calculated in a similar manor

$$\Psi = \frac{1}{m-1}\tilde{Y}^{\top} N \tilde{Y} \tag{6.2}$$

where N is the Noda-Hilbert matrix, which has the following structure

$$N = \frac{1}{\pi}\begin{bmatrix} 0 & 1 & \frac{1}{2} & \frac{1}{3} & \dots \\ -1 & 0 & 1 & \frac{1}{2} & \dots \\ -\frac{1}{2} & -1 & 0 & 1 & \dots \\ -\frac{1}{3} & -\frac{1}{2} & -1 & 0 & \dots \\ \dots & \dots & \dots & \dots & \dots \end{bmatrix}. \tag{6.3}$$

6.2.4 Disrelation Mapping

The disrelation spectrum is an approximation of the asynchronous spectrum. It has the advantage of being easier to compute specific spectral variables of interest without calculating the whole spectrum, as it avoids the use of the Noda-Hilbert matrix. The disrelation intensity between the variance at two spectral variables can be calculated directly from the synchronous spectrum.

$$\Lambda(\nu_1, \nu_2) = \sqrt{\Phi(\nu_1, \nu_1)\Phi(\nu_2, \nu_2) - \Phi^2(\nu_1, \nu_2)} \tag{6.4}$$

which will equal zero on the diagonal elements of the synchronous spectrum and close to zero if there is a synchronous relationship between the variance of ν_1 and ν_2.

Disrelation mapping, developed recently by Hideyuki Shinzawa (Shinzawa et al., 2016), extends disrelation analysis to FTIR spectroscopic images. It can be conceptually viewed as an image convolution technique. Doubly correlated 2D correlation analysis is applied to each element of the image with its neighbours, which are defined by the size of the convolution window. Figure 6.1 illustrates the construction of an image based on the disrelation intensity. High disrelation intensity within an image element indicates ν_1 and ν_2 vary out-of-phase with each other within a local spatial area.

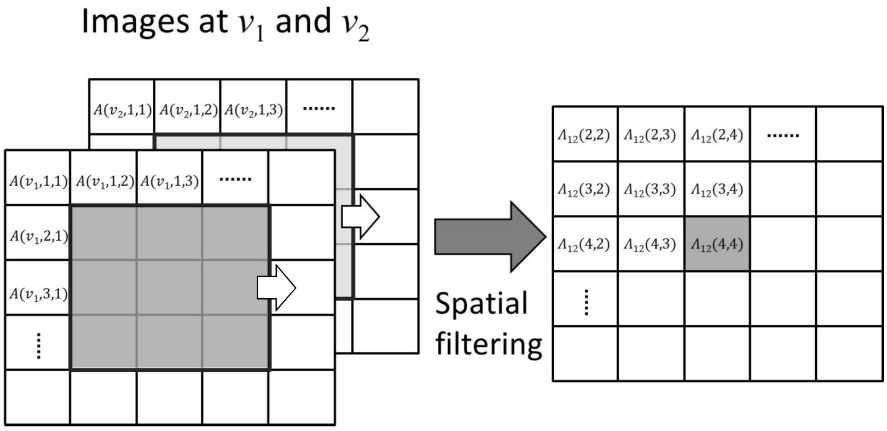


Figure 6.1: Schematic showing the generation of disrelation maps from two method P absorbance images.

6.3 Results and Discussion

6.3.1 2D Correlation Analysis of Water Perturbed by Temperature

2D hetero-correlation analysis has been done to compare the effects of temperature on the absorbance spectrum of water in the mid-infrared with the near infrared region. However, generalised 2D correlation analysis has not been done to characterise this effect in the mid-infrared region.

Figure 6.2 shows the results of heating water from 22 to 37 °C. A baseline distortion as a result temperature can be seen as the kinetic progresses. Fortunately, in this region the baseline distortion is linear and can be removed by subtracting a constant. A general decrease in the band's intensity can be seen, except at the shoulder present at 3600 cm^{-1}, which is increasing.

Figure 6.3 shows the synchronous and asynchronous spectrum generated from the spectral kinetic of water. The synchronous spectrum allows the better visualisation of the sub-band at 3600 cm^{-1}. The crosspeak at 3600/3260 cm^{-1} has a negative sign, indicating a synchronous relationship between the decrease at 3260 cm^{-1} and the increase at 3600 cm^{-1}. The sub-band at 3600 cm^{-1} has been previously assigned to free water so the increase of this band as a function of temperature is expected. The asynchronous spectrum indicates that there are two more sub-bands at 3220 cm^{-1} and 3400 cm^{-1}. We know that both of these bands are decreasing from the spectral kinetic, however they are not decreasing with a conserved phase relationship. The sign indicates that the band at 3220 cm^{-1} is decreasing first followed by the band at 3400 cm^{-1}. The bands at 3220 cm^{-1} and 3400 cm^{-1} have been assigned to bound water

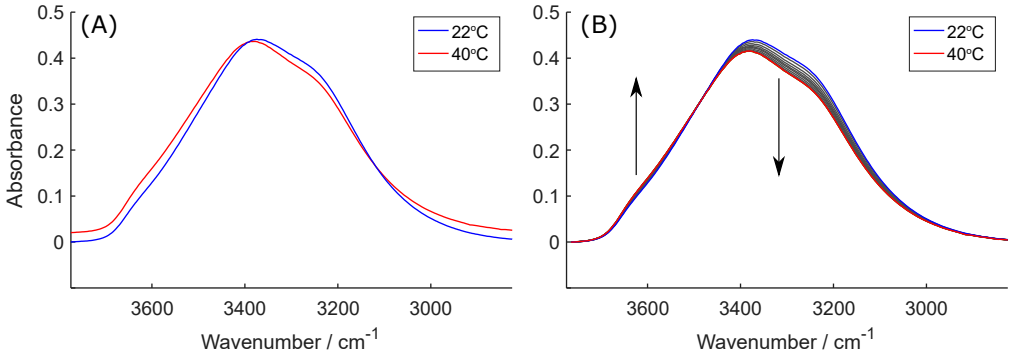


Figure 6.2: (A) Illustration of the linear baseline distortion caused by the change in temperature. (B) A spectral kinetic showing the changes in water's OH stretching band as a function of temperature, after a linear offset correction was applied to the data.

and intermediate water, respectively. Bound water corresponds to water engaged in four hydrogen bonds, whereas intermediate water is thought to be a mixture of water engaged in 2 or 3 hydrogen bonds (Brubach et al., 2005). As water is heated it is expected that water engaged in four hydrogen bonds could become intermediately bound as well as free water. The intermediate water would tend to become free water. This explains the synchronous relationship with the increase in free water and the overall decrease in bound and intermediate water collectively. It also explains why bound and intermediate water do not decrease synchronously.

The synchronous and asynchronous spectra indicate that a three sub-band picture best describes the dynamic spectrum of the OH stretching band perturbed by temperature. This is in good agreement with previous studies (Brubach et al., 2005; Bergonzi et al., 2014).

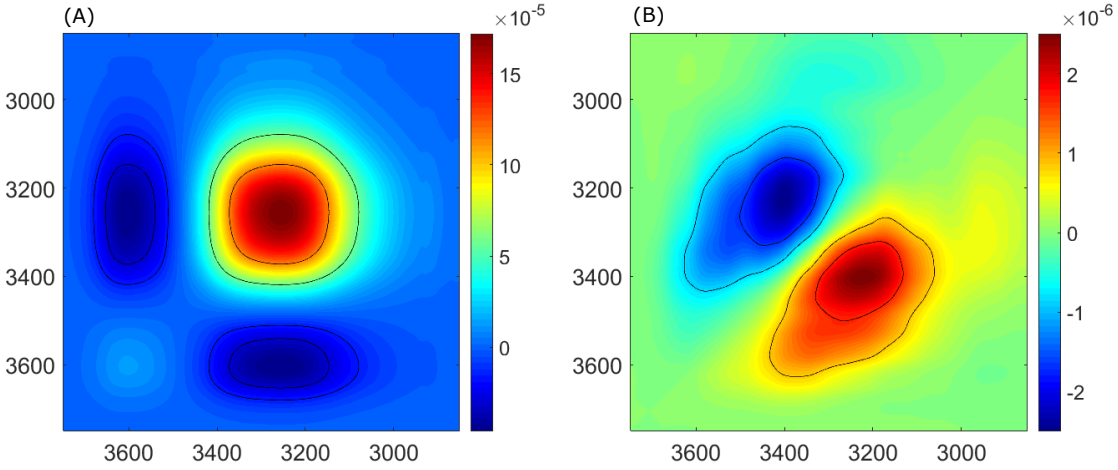


Figure 6.3: Synchronous (A) and asynchronous (B) spectrum generated from generalised 2D correlation analysis of the spectra presented in figure 6.2.

6.4 2D Correlation Analysis of Cell Adhesion

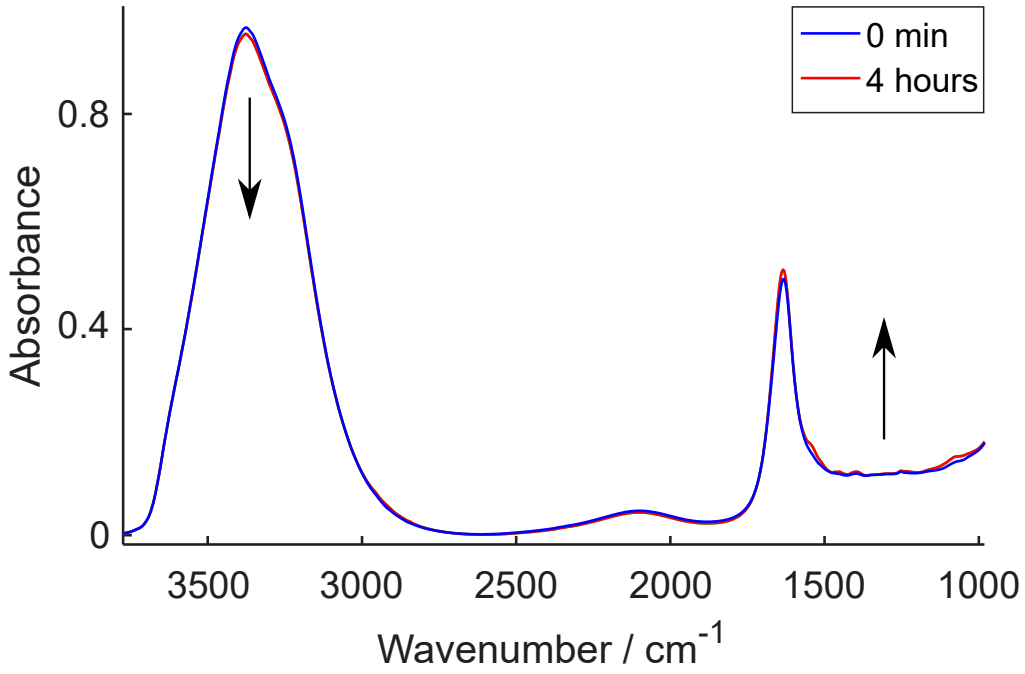


Figure 6.4: Spectra at 0 minutes and 4 hours after seeding cells onto the ZnSe ATR crystal at room temperature. Although measurements were taken every 10 minutes for 4 hours, only the first and last spectrum are shown here.

To investigate the change in the OH stretching lineshape as a function of cell adhesion multiple-reflection ATR-FTIR spectroscopy was first employed. It was demonstrated in the previous section that temperature can affect the OH stretching lineshape. For this reason the accessory was not heated for these experiments. To maximise the signal in the OH stretching region, a zinc selenide crystal was used instead of germanium. Zinc sulphide was also attempted but the absorbance of water was found to be too great in the 3000-3700 cm^{-1} region and saturation was reached. Cells were not expected to adhere well under these conditions but, as can be seen by figure 6.4, the presence of cells can still be detected. After initially seeding cells onto the Zinc selenide crystal, cells were measured over a 4 hour period. Although temperature variations during this time were minimal, baseline distortions did affect the 2D correlation analysis. This was minimised in the OH stretching region with an offset correction at 3700 cm^{-1}

The results of the 2D correlation analysis can be seen in figure 6.5. The synchronous spectrum in figure 6.5A captures the overall decrease in absorbance of the OH stretching band. The crosspeak at 2925/3370 cm^{-1} has a negative sign. This illustrates that CH_3 bands increase synchronously as the overall OH band is decreas-

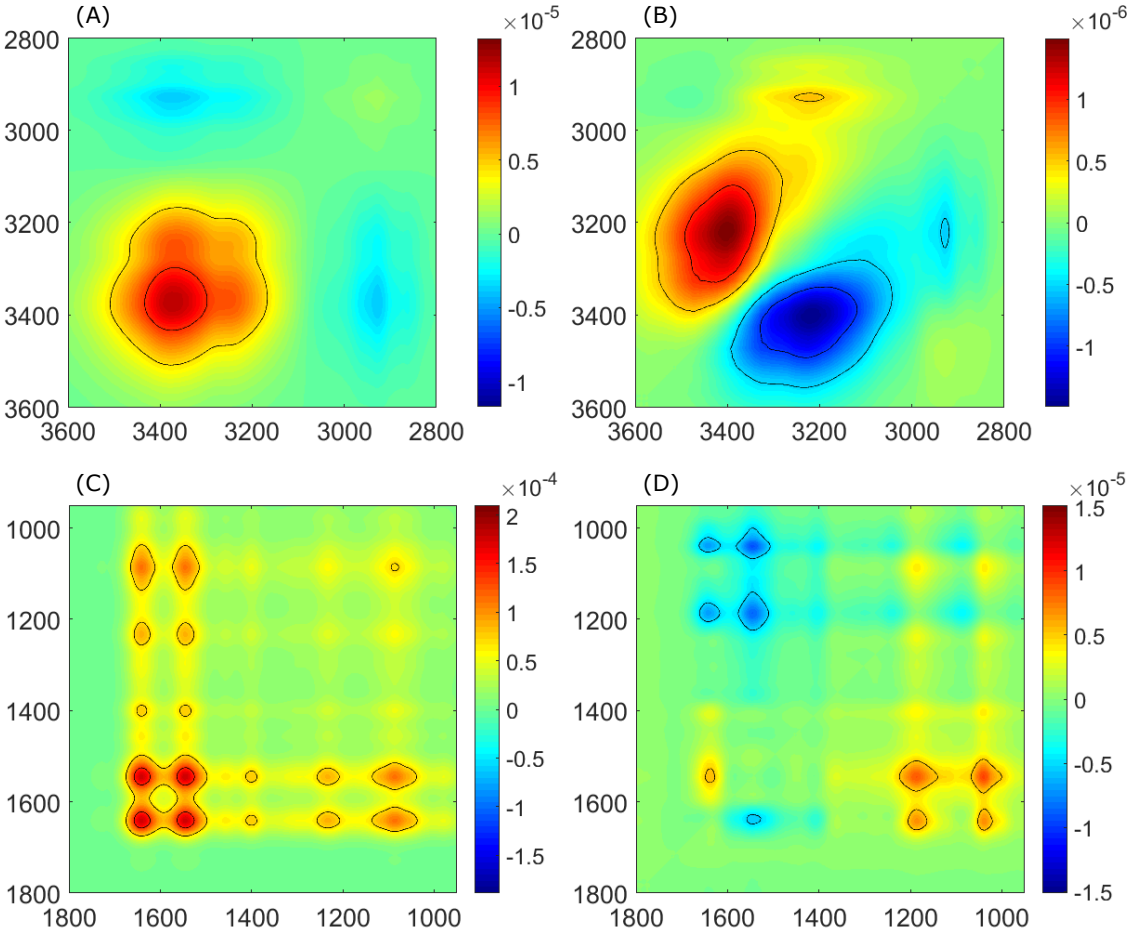


Figure 6.5: Part (A) and (B) show the synchronous and asynchronous 2D correlation spectrum, respectively, of the OH stretching region from the spectral kinetic shown in figure 6.4. Part (C) and (D) show the synchronous and asynchronous 2D correlation spectrum from the same spectral kinetic in the fingerprint region

ing. The CH_3 band is associated with the cell membrane, so it can be said that the increasing presence of the cell population is synchronous with the decrease in the OH stretching band. The decrease is expected as the concentration of water is lower within the cell compared to cell medium.

The asynchronous spectrum in figure 6.5B shows a crosspeak at 3220/3420 cm^{-1}, similar to the one present in figure 6.3B. However, here the crosspeak is negative. The interpretation using Noda's rules is that the sub-band at 3420 cm^{-1} is changing before the sub-band at 3220 cm^{-1} in this case. This crosspeak also implies the distribution of water at 3220 cm^{-1} and 3420 cm^{-1} is essentially different between cells and cell medium.

2D correlation analysis was also carried out in the fingerprint region after an offset correction at 1750 cm^{-1}, which can be seen in figure 6.5C and D. The synchronous spectrum shows the synchronous increase of the main bands associated with cells in this region. The asynchonous spectrum shows a cross peak at 1640/1540 cm^{-1} indicating amide I and II do not increase synchronously as the presence of cell increases. This is expected to be due to the simultaneous decrease in absorbance of water's OH bending mode, which overlaps with the amide I band. Interestingly, the asynchronous spectrum in figure 6.5D indicates the presence of two bands and 1030 cm^{-1} and 1185 cm^{-1} whose intensity is not correlated with either bands corresponding to protein or nucleic acids. The band at 1030 cm^{-1} was assigned to glycogen previously in chapter 4. The band at 1185 cm^{-1} has been previously assigned to 2-phosphoglycerate, an intermediate in the glycolytic pathway, in other studies (Quaroni and Zlateva, 2014). What can be said empirically is both peaks were strongly asynchronous with protein bands, and weakly asynchronous with nucleic acid bands at 1230 cm^{-1} and 1085 cm^{-1}. As there is no asynchronous intensity between the bands at 1185 cm^{-1} and 1030 cm^{-1}, it is likely that the band at 1185 cm^{-1} is at least strongly associated with the presence of glycogen.

6.5 Disrelation Mapping of the OH Stretching Region

To examine the spectral differences in the OH stretching region between cells and cell medium spectroscopic imaging was employed. One advantage of using a spectroscopic imaging dataset is that the effects due to temperature on the OH stretching band can be avoided, unlike the multiple-reflection study described in the previous section. To decide the best parameters for disrelation mapping a line of spectra going through the interface between cell and cell medium was extracted as shown

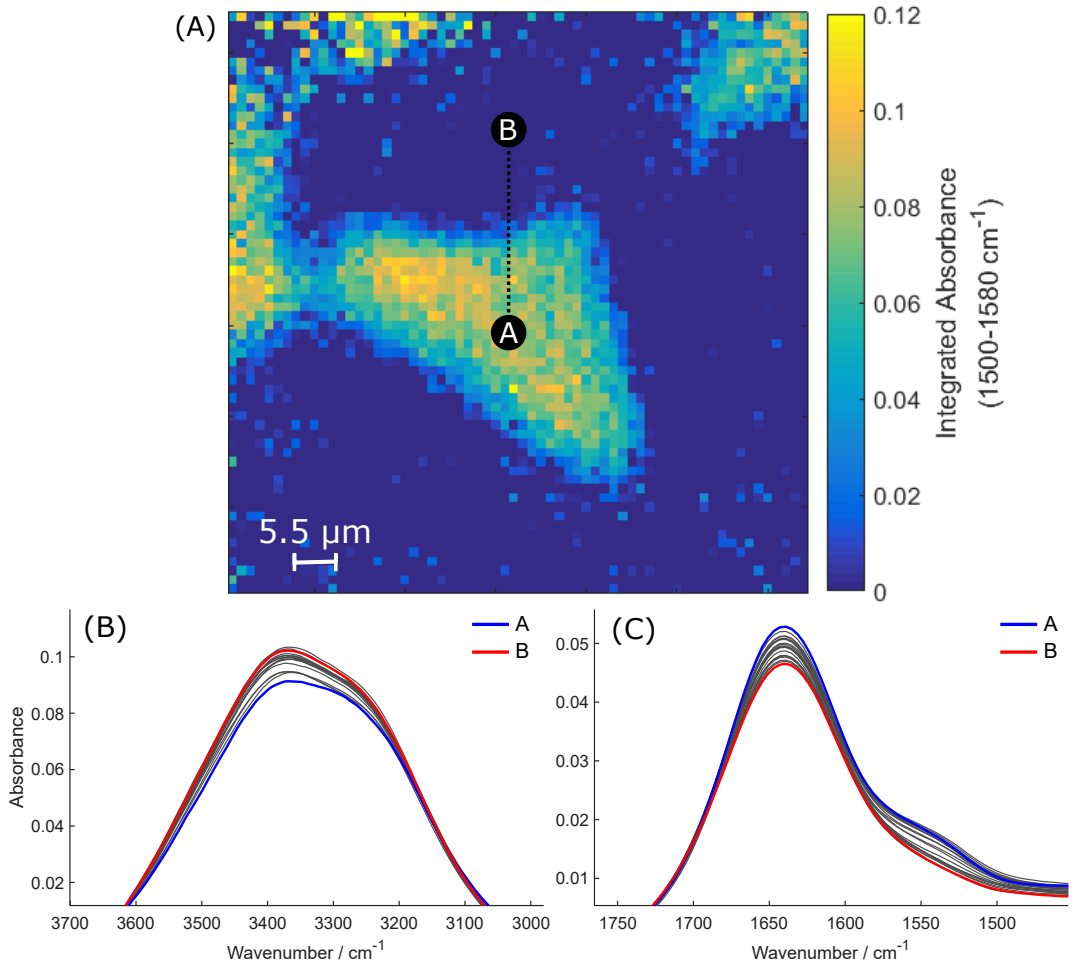


Figure 6.6: (A) Integrated absorbance image of amide II. The line illustrates the spectra extracted for disrelation analysis. The plots below show the extracted spectra after an offset-correction at (B) 3700 cm^{-1} in the 3600 - 3000 cm^{-1} region, and (C) 1750 cm^{-1} in 1750 - 1450 cm^{-1} region.

in figure 6.6 and the resulting spectra are shown in section B and C of the figure.

Figure 6.6 shows an increase in the OH stretching band in cell medium compared to the cell, which is more striking than compared to the spectra obtained from multiple-reflection spectroscopy. Another advantage of spectroscopic imaging is that regions corresponding to cell and cell medium are spatially isolated, whereas multiple-reflection experiments obtain an average spectrum from a mixture of cell medium and cell in contact with the crystal. The disrelation analysis of the OH stretching band from this line is shown in figure 6.7. As with previous analysis, the synchronous OH autopeak in figure 6.7A captures the overall decrease of the OH stretching band. The disrelation spectrum in figure 6.7B also shows a similar cross-peak position to that seen in the previous 2D correlation analysis. This indicates again that there is a disrelation in the variance of two sub-bands as a function of distance through the cell border, which is not temperature dependent. This pro-

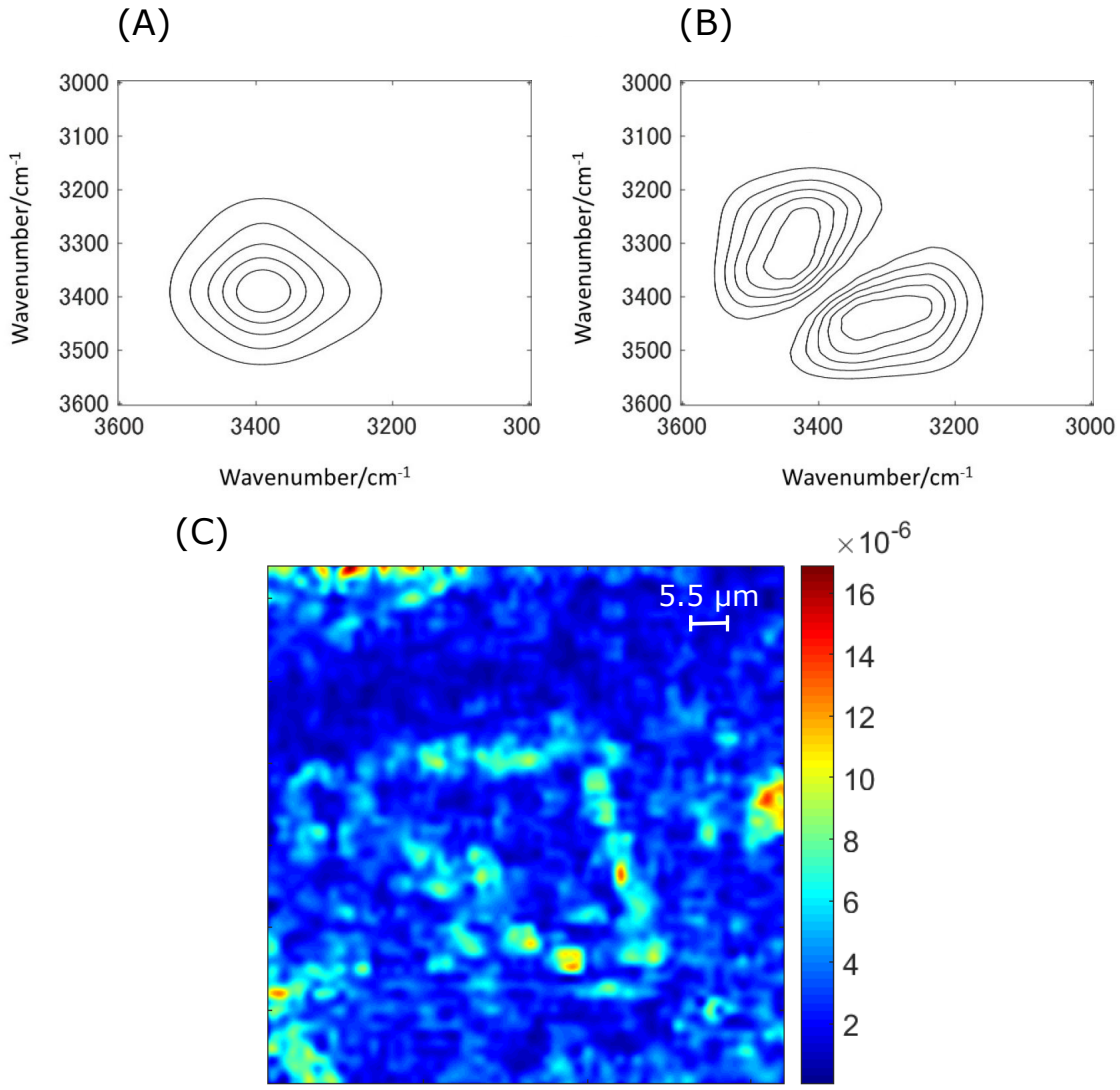


Figure 6.7: Synchronous (A) and disrelation (B) analysis of the spectra extracted from the line illustrated in figure 6.6. Image (C) shows a disrelation map generated from the disrelation intensity between 3220 cm^{-1} and 3420 cm^{-1}.

vides further evidence that the change in the OH lineshape from cell to cell medium cannot be explained simply from the change in concentration of water, and different distributions of hydrogen bonded states of water are seen within cells.

To investigate the disrelation between the two sub-bands at 3220 cm^{-1} and 3420 cm^{-1} throughout the whole image disrelation mapping was employed. It was found that comparing the disrelation between two method R generated absorbance images gave much better results than using method P absorbance images, which disrelation mapping initially used (Shinzawa et al., 2016). As mentioned in section 3.6, in method R integrated absorbance images, a local linear baseline is drawn between

two user defined wavenumbers. The absorbance value at the desired point is then modified by subtracting the value of the local baseline at the same wavenumber. For both the method R absorbance images at 3220 cm^{-1} and 3420 cm^{-1}, the baseline was drawn between 3700 cm^{-1} and 3100 cm^{-1}. Figure 6.7C shows clearly that there is significant disrelation intensity mostly at the border of the cell with cell medium.

6.6 Disrelation Mapping of the Amide/OH Region

To investigate the cause of the disrelation between the OH stretching sub-bands further, disrelation analysis was carried out between the fingerprint region and the OH stretching region. As can be seen from figure 6.8A, disrelation intensity is present between the amide bands and the 3420 cm^{-1} sub-band, but not the 3220 cm^{-1} sub-band. This implies an asynchronous relationship between the variation of protein and intermediate water but not bound water. The disrelation map generated using the 3420/1540 cm^{-1} crosspeak, shown in figure 6.8B, also shows a very similar pattern to the 3220/3420 cm^{-1} disrelation map. The increasing presence of protein is therefore correlated with the increasing ratio of bound to intermediate water. No significant disrelation intensity is seen between either the phosphate 1 band at 1080 cm^{-1}, or the CH_3 band at 2930 cm^{-1}, with the 3420 cm^{-1} sub-band as shown in figure 6.8C and D.

To compare this with the multiple-reflection ATR-FTIR experiments, 2D correlation analysis was carried out on the 3700-2800 cm^{-1} region with the 1800-950 cm^{-1} region, which is shown in figure 6.9. Here asynchronous crosspeaks between intermediate water and phosphate I can be seen, in addition to crosspeaks between intermediate water and the amide bands. The x axis position of these bands is consistent with the disrelation analysis in figure 6.7. The two slightly different results regarding the phosphate I band can be explained by the lack of spatial resolution in multiple-reflection ATR-FTIR spectroscopy measurements.

In the spectroscopic imaging data, spatially resolved spectra are being examined across the boundary of a single cell that is already adhered to the surface. From the disrelation map generated using the 3220/3420 cm^{-1}, it can be seen that the disrelation mainly occurs at the cell boundary as opposed to further inside the cell. The nucleus of the cell, where the strongest phosphate signal is present, is not at the boundary of the cell with cell medium.

In the multiple-reflection ATR-FTIR measurements, much higher signal to noise is seen but there is no spatial resolution. What is measured is the average increase in the presence of cells as they adhere to the crystal. The correlation analysis of

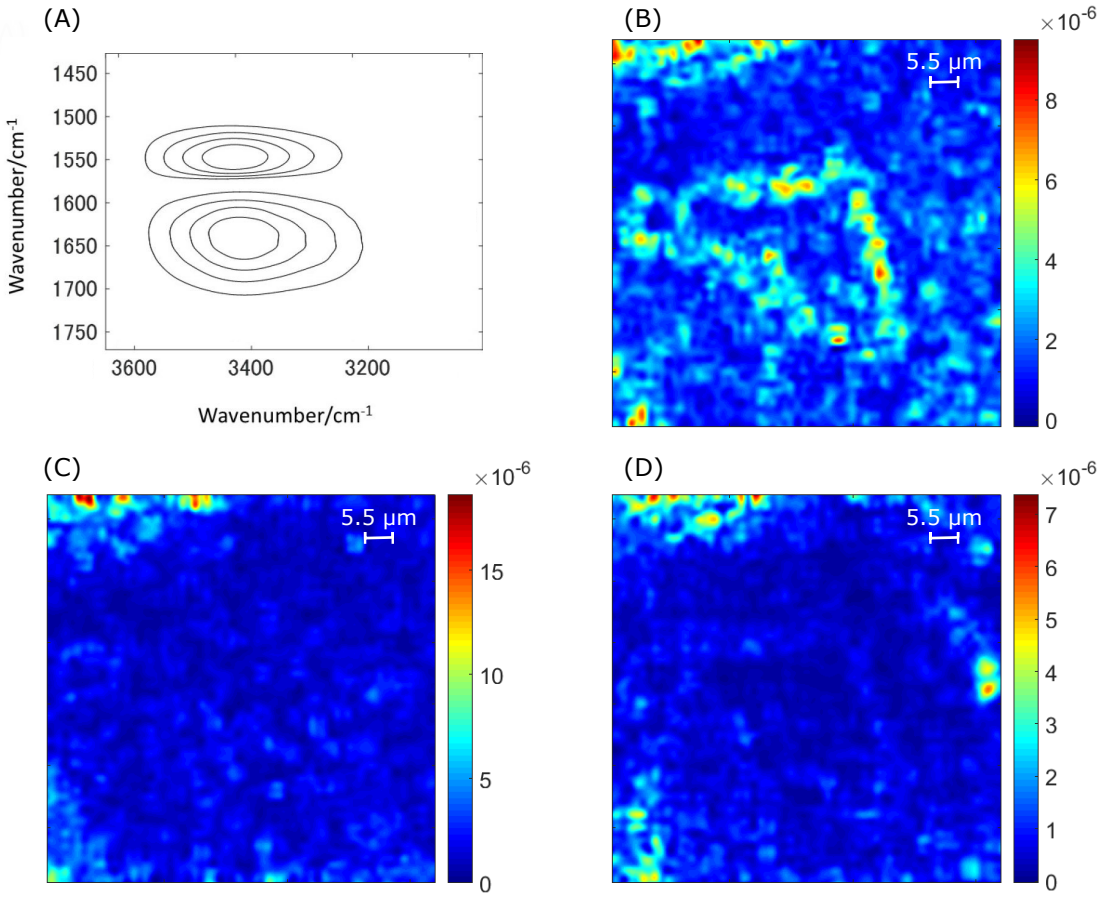


Figure 6.8: (A) Disrelation analysis of the amide region between 1750-1400 cm^{-1} with the OH stretching region between 3000-3600 cm^{-1}. The crosspeaks at 3420/1640 cm^{-1} and 3420/1540 cm^{-1} show there is out-of-phase variation between protein and intermediately bound water. The disrelation maps were generated using the following crosspeaks: (B) 1540/3420 cm^{-1}, (C) 2930/3420 cm^{-1}, (D) 1080/3420 cm^{-1}. Significant disrelation intensity been be seen at the cell/cell medium interface in image (B) but not in images (C) and (D).

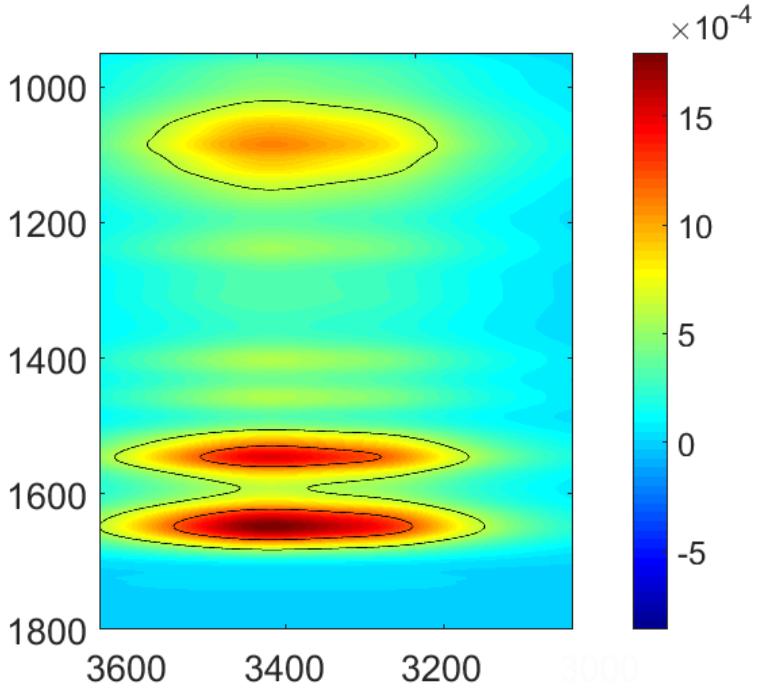


Figure 6.9: Asynchronous spectrum between fingerprint region and OH stretching region of the spectral kinetic presented in figure 6.4.

the fingerprint region shown in figure 6.5 also shows that there was no significant disrelation between the evolution of amide I and II with phosphate I in the multiple-reflection ATR measurements. This makes it unsurprising that there is asynchronous intensity between intermediate water and phosphate I in the multiple-reflection ATR measurements.

6.7 Conclusion

This chapter presented 2D correlation analysis to investigate the presence of different molecular states of water in living cells. First 2D correlation analysis identified three main sub-bands under the water's OH stretching band, in good agreement with previous literature.

2D correlation analysis was then carried out to see the effects of cell adhesion on the water's OH stretching lineshape. Whilst bands at different frequencies were not seen, the distribution of intermediate and bound water was found to be different between cells and cell medium.

Finally, disrelation mapping was carried out on spectroscopic imaging data of a single adhered cell. It was found that the 3420/3220 cm^{-1} disrelation crosspeak was strongly associated with the increasing presence of protein within the cell. Strong disrelation intensity was seen at 1540/3420 cm^{-1} but not 1540/3220 cm^{-1} , indicating that the change in bound water was correlated with the change in protein.

This analysis highlights the importance of the OH stretching region for the analysis of a cell's internal environment, information that is not accessible from fixed cells or currently by transmission mode infrared spectroscopic imaging. More generally, this work demonstrates that the combination of spectroscopic imaging with 2D correlation analysis can provide valuable insight not easily obtained with traditional multivariate methods.

7 Conclusion and Future Work

In this thesis, the methodology for micro ATR-FTIR spectroscopic imaging of live cells was further developed. Subsequent studies were then done to explore whether it was possible to detect a metal-carbonyl derivative compound in living cells. Finally, the recently developed analysis technique disrelation mapping was applied to spectroscopic imaging datasets of live cells.

7.1 ATR-FTIR Spectroscopic Imaging of Live Cells

A considerable portion of this thesis was dedicated to improving the reproducibility of micro ATR-FTIR spectroscopic imaging of live cells. Micro ATR-FTIR spectroscopic imaging can both achieve better spatial resolution than seen in transmission mode and is able to work in bulk aqueous environments, making it a potentially powerful tool to study live cells. A major technical challenge was found to be ensuring good contact of cells with the ATR crystal. In practice the only way to achieve this, whilst ensuring cells remained viable after the measurement, was to directly seed and culture cells on the ATR crystal.

Effective cleaning of the crystal and the improved surface wettability from ozone/UV treatment was found to be the most successful way of ensuring good cell adhesion. Water vapour removal combined with box filtering of amide II integrated absorbance images was found to be a robust method for the initial identification of cells on the ATR crystal surface. By removing areas of integrated absorbance images known to correspond to cell medium, the distribution of weaker spectroscopic bands corresponding to nucleic acids and glycogen could also be visualised within cells. The nucleus, perinucleus, and cytoplasm was found to be distinguishable with univariate analysis after this preprocessing. Different lineshapes of the phosphate I band corresponding to DNA and RNA were also seen for the first time in a living cell.

This work demonstrates that micro ATR-FTIR spectroscopic imaging can be used to examine living cells in bulk aqueous environments with subcellular resolution.

7.2 Micro ATR-FTIR Spectroscopic Imaging for Drug Detection within Living Cells

This thesis presents the first demonstration that micro FTIR spectroscopic imaging is capable of detecting exogenous molecules directly within living cells. A metal-carbonyl derivative was kindly provided by the Policar group for this work.

Preliminary studies were done using multiple-reflection ATR-FTIR spectroscopy. This is the second example of direct drug detection with this methodology, and the first time a drug was used that required the use of DMSO. Even at a 0.5% volume, the presence of DMSO in cell medium had an observable negative effect on the spectra of live cells. Specifically, cells rounded due stress induced by DMSO, reducing contact with the ATR crystal. In spite of this, the drug's presence was detectable within cells after 10 minutes. There were also signs that the pH environment of the metal-carbonyl drug changed during the experiment. This work shows that multiple-reflection ATR-FTIR spectroscopy can be used to monitor dynamic changes of live cell populations in response to exogenous molecules. In addition, chemical modifications of the drug can be monitored simultaneously.

Spectroscopic imaging experiments to detect the same compound were much more challenging. The stress induced by the addition of the DMSO and the drug itself meant cell adhesion was inherently poorer. The maximum time cells could be incubated with the drug and still successfully measured was found to be 40 minutes. Amide II integrated absorbance images revealed significant phenotypic changes in the cell's morphology. It was also demonstrated that the drug could be detected directly within a single cell, but not the cell's outer extremity or the surrounding cell medium. The drug was also shown to be present in the perinuclear region but not the nucleus, in agreement with previous results.

This work shows micro ATR-FTIR spectroscopic imaging can be used to investigate sub-cellular drug distribution within living cells. It can simultaneously provide phenotypic information about the cell's morphology.

7.3 Disrelation Mapping to Investigate Molecular States of Water in Live Cells

A combination of generalised 2D correlation analysis, disrelation analysis, and disrelation mapping was applied to spectroscopy and spectroscopic imaging datasets of live cells. For the first time different distributions of molecular states of water were

observed in live cells with both methodologies.

2D correlation analysis was carried out to investigate the change in water's dynamic spectrum as a function of heating. This indicated that three sub-bands best describes the evolution of water's OH stretching band, which were assigned to bound, free, and intermediate water. Disrelation analysis of spectroscopic images of live cells showed a similar cross peak to that observed in the water heating experiment. As all the spectra within the spectroscopic imaging dataset were taken simultaneously, it is not expected that significant variations in temperature would be seen across the image. This implies different distributions of the three states of water are present within cells compared to aqueous medium.

Disrelation mapping provided more striking evidence of this, showing a significant disrelation intensity at the interface between the cell and the surrounding cell medium. Disrelation analysis also provided a further insight, attributing the change in molecular states of water to the strong increase of water associated with protein.

This work further illustrates that disrelation mapping of spectroscopic images is a powerful tool to highlight subtle spectral differences in complex samples.

7.4 Overall Conclusions

A convenient method of conducting FTIR spectroscopic imaging measurements on live cells, without the need of microfluidic technology, has been developed in ATR mode. The increased spatial resolution combined with the ability to generate an average spectrum from regions of interest proved particularly useful in the analysis of spectroscopic images. DNA and RNA was found to be distinguishable using the phosphate I band and an exogenous molecule was detected within a living cell for the first time using FTIR spectroscopic imaging. A further benefit of the data generated from this methodology is the high signal to noise of the OH stretching region, which allowed the hydrogen bonding environment of water to be investigated. These results show that ATR-FTIR spectroscopic imaging of live cells has great potential in the fields of cell biology and early stage drug discovery.

7.5 Recommendations for Future Work

Many of the challenges encountered in this work stem from the fact that the Agilent ATR-FTIR microscope was not designed explicitly for imaging of live cells. Some ideas to further the methodology for infrared spectroscopic imaging of live cells are presented below.

1. The coupling of a quantum cascade laser to an infrared microscope capable of ATR imaging mode is expected to greatly improve the quality of spectroscopic measurements. As quantum cascade lasers (QCL) are discrete sources of infrared, specific wavenumbers could be scanned. This would greatly improve the measurement time in ATR spectroscopic imaging. The brilliance of the source would also improve the signal to noise, allowing better utilisation of the high spatial resolution seen in ATR spectroscopic imaging. A QCL source would also improve transmission imaging as larger path lengths could be utilised. In addition, transflection of live cells could be explored further. As light would travel through the same cell twice a greater proportion of the absorbance signal would come from cells, compared to transmission imaging with an increased path length.

2. A heated micro ATR crystal would allow continuous monitoring of cells with an infrared microscope. As seen in multiple-reflection ATR experiments, continuous monitoring greatly improves the ability to measure the kinetics of drug accumulation within the cell and detect changes in both the drug and the cell.

3. A different ATR accessory design would greatly improve infrared spectroscopic imaging of live cells. For example the ATR crystal should not be glued in place, but designed to be held in place mechanically. This would allow more effective cleaning and allow other forms of surface modification to be carried out on the ATR crystal to improve the hydrophilicity of the surface. This could also allow the use of Surface Enhanced Infrared Absorption Spectroscopy (SEIRAS), which can increase the signal by 2 orders of magnitude (Ataka and Heberle, 2007).

4. Ultimately, super-resolution techniques will be required for infrared spectroscopy to properly investigate organelles smaller than the nucleus. Systems like this have been developed but so far they have not been applied to live cells. This would be a very interesting area to pursue.

5. Micro ATR-FTIR spectroscopic imaging is capable of distinguishing the nucleus from cytoplasm. This is valuable information for the development of

chemotherapy drugs, which often accumulate in the nucleus. This application should be explored further. It is speculated that with the instrumentation improvements suggested above other exogenous chemical groups, in addition to metal-carbonyl derivatives, could be detected.

6. Metal-carbonyl derivatives have been proven straight forward to detect by multiple-reflection ATR spectroscopy of cell populations. There is great scope here for live cell assay development using metal-carbonyl derivatives as probes. One advantage of infrared spectroscopy over fluorescence is that it is more straight forward to make quantitative measurements within cells, as fluorescence intensity of is affected by the local environment within cells.

7. The combination of spectroscopic imaging with two-dimensional correlation spectroscopy has proven very useful. Spectroscopic imaging is useful for highlighting areas of chemical heterogeneity within a sample area. Two-dimensional correlation analysis, or disrelation mapping, can then be effectively utilised to further investigate the spectral changes that occur across this boundary, which are often not easy to characterise. It is expected that this method of analysis will be very useful in a variety of applications of spectroscopic imaging.

Bibliography

Alberts, B., Johnson, A., Lewis, J., Walter, P., Raff, M., Roberts, K., 2002. Molecular Biology of the Cell 4th Edition: International Student Edition. Routledge.

Anson, C. E., Baldwin, T. J., Creaser, C. S., Fey, M. A., Stephenson, G. R., 1996. Ir-active organometallic ph probes. Organometallics 15 (5), 1451–1456.

Ataka, K., Heberle, J., 2007. Biochemical applications of surface-enhanced infrared absorption spectroscopy. Analytical and bioanalytical chemistry 388 (1), 47–54.

Atkins, P., de Paula, J., 2002. Atkins' Physical Chemistry, 7th Edition. Oxford University Press.

Atkins, P. W., Friedman, R. S., 2011. Molecular quantum mechanics. Oxford university press.

Averett, L. A., Griffiths, P. R., Nishikida, K., 2008. Effective path length in attenuated total reflection spectroscopy. Analytical chemistry 80 (8), 3045–3049.

Balaz, S., Lukacova, V., 2002. Subcellular pharmacokinetics and its potential for library focusing. Journal of Molecular Graphics and Modelling 20 (6), 479–90.

Bambery, K. R., Wood, B. R., Don, M., 2012. Resonant mie scattering (RMieS) correction applied to FTIR images of biological tissue samples. Analyst 137 (1), 126–32.

Bedolla, D., Kenig, S., Mitri, E., Ferraris, P., Marcello, A., Grenci, G., Vaccari, L., 2013. Determination of cell cycle phases in live b16 melanoma cells using IRMS. Analyst 138 (14), 4015–4021.

Bedolla, D. E., Kenig, S., Mitri, E., Storici, P., Vaccari, L., 2014. Further insights into the assessment of cell cycle phases by ftir microspectroscopy. Vibrational Spectroscopy 75, 127–135.

Bellisola, G., Sorio, C., 2012. Infrared spectroscopy and microscopy in cancer research and diagnosis. American Journal of Cancer Research 2, 1–21.

Bergonzi, I., Mercury, L., Brubach, J., Roy, P., 2014. Gibbs free energy of liquid water derived from infrared measurements. Phys Chem Chem Phys 16 (45), 24830–24840.

Binder, H., 2007. Water near lipid membranes as seen by infrared spectroscopy. European Biophysics Journal 36 (4-5), 265–279.

Birarda, G., Grenci, G., Businaro, L., Marmiroli, B., Pacor, S., Piccirilli, F., Vaccari, L., 0. Infrared microspectroscopy of biochemical response of living cells in microfabricated devices. Vibrational Spectroscopy 53 (1), 6–11.

Birarda, G., Ravasio, A., Suryana, M., Maniam, S., Holman, H. N., Grenci, G., 2016. IR-Live: fabrication of a low-cost plastic microfluidic device for infrared spectromicroscopy of living cells. Lab Chip 16 (9), 1644–1651.

Boguslawa, C., Pilorz, S., Hawranek, J. P., 2005. Temperature-dependent water structural transitions examined by near-IR and mid-IR spectra analyzed by multivariate curve resolution and two-dimensional correlation spectroscopy. Analytica Chimica Acta 544 (1-2), 15–25.

Boydston-White, S., Gopen, T., Houser, S., Bargonetti, J., Diem, M., 1999. Infrared spectroscopy of human tissue. v. infrared spectroscopic studies of myeloid leukemia (ml-1) cells at different phases of the cell cycle. Biospectroscopy 5 (4), 219–227.

Brubach, J., Mermet, A., Filabozzi, A., Gerschel, A., Roy, P., 2005. Signatures of the hydrogen bonding in the infrared bands of water. J Chem Phys 122 (18), 184509.

Buijs, H., 2006. Incandescent sources for mid- and far-infrared spectrometry. Handbook of Vibrational Spectroscopy. Vol. 1. John Wiley & Sons, Ltd.

Cammarata, L., Kazarian, S. G., Salter, P., Welton, T., 2001. Molecular states of water in room temperature ionic liquids. Physical Chemistry Chemical Physics 3 (23), 5192–5200.

Chan, A. K. L., Fale, P. L., 2014. Label-Free in situ quantification of drug in living cells at micromolar levels using infrared spectroscopy. Analytical Chemistry 86 (23).

Chan, A. K. L., Kazarian, S. G., 2013a. Aberration-free FTIR spectroscopic imaging of live cells in microfluidic devices. Analyst 138 (14), 4040–4047.

Chan, A. K. L., Kazarian, S. G., 2013b. Correcting the effect of refraction and dispersion of light in FT-IR spectroscopic imaging in transmission through thick infrared windows. Analytical chemistry 85 (2), 1029–1036.

Chan, A. K. L., Kazarian, S. G., 2016. Attenuated total reflection fourier-transform infrared (ATR-FTIR) imaging of tissues and live cells. Chem Soc Rev 45 (7), 1850–64.

Chan, A. K. L., Kazarian, S. G., Mavraki, A., Williams, D., 2005. Fourier transform infrared imaging of human hair with a high spatial resolution without the use of a synchrotron. Applied Spectroscopy 59 (2), 149–155.

Chan, A. K. L., Kazarian, S. G., Vassou, D., Gionis, V., Chryssikos, G. D., 2007. In situ high-throughput study of drug polymorphism under controlled temperature and humidity using ft-ir spectroscopic imaging. Vibrational spectroscopy 43 (1), 221–226.

Chan, A. K. L. A., Kazarian, S. G., 2011. Tip-enhanced raman mapping with top-illumination afm. Nanotechnology 22 (17), 175701.

Chen, L., Holman, H. N., Hao, Z., Bechtel, H. A., Martin, M. C., Wu, C., Chu, S., 2012. Synchrotron infrared measurements of protein phosphorylation in living single PC12 cells during neuronal differentiation. Analytical Chemistry 84 (9), 4118–25.

Chiriboga, L., Xie, P., Yee, H., Vigorita, V., Zarou, D., Zakim, D., Diem, M., 1998. Infrared spectroscopy of human tissue. i. differentiation and maturation of epithelial cells in the human cervix. Biospectroscopy 4 (1), 47–53.

Choe, C., Lademann, J., Darvin, M. E., 2016. Depth profiles of hydrogen bound water molecule types and their relation to lipid and protein interaction in the human stratum corneum in vivo. Analyst 141 (22), 6329–6337.

Clède, S., Lambert, F., Sandt, C., Gueroui, Z., Delsuc, N., Dumas, P., Vessières, A., Policar, C., 2012a. Synchrotron radiation FTIR detection of a metal-carbonyl tamoxifen analog. correlation with luminescence microscopy to study its subcellular distribution. Biotechnology Advances 31 (3), 393–5.

Clède, S., Lambert, F., Sandt, C., Gueroui, Z., Réfrégiers, M., Plamont, M.-A., Dumas, P., Vessières, A., Policar, C., 2012b. A rhenium tris-carbonyl derivative as a single core multimodal probe for imaging (scompi) combining infrared and luminescent properties. Chemical Communications 48 (62), 7729–7731.

Clède, S., Policar, C., 2015. Metal–Carbonyl units for vibrational and luminescence imaging: Towards multimodality. Chemistry–A European Journal 21 (3), 942–958.

Clède, S., Policar, C., Sandt, C., 2014. Fourier transform infrared (FT-IR) spectromicroscopy to identify cell organelles: Correlation with fluorescence staining in MCF-7 breast cancer cells. Applied Spectroscopy.

Cohen, L., 1998. The generalization of the wiener-khinchin theorem. Acoustics, Speech and Signal Processing, 1998. Proceedings of the 1998 IEEE International Conference on. Vol. 3. IEEE, pp. 1577–1580.

Dazzi, A., Prater, C. B., Hu, Q., Chase, D. B., Rabolt, J. F., Marcott, C., 2012. Afm–ir: combining atomic force microscopy and infrared spectroscopy for nanoscale chemical characterization. Applied Spectroscopy 66 (12), 1365–1384.

Derenne, A., Gasper, R., Goormaghtigh, E., 2011. The FTIR spectrum of prostate cancer cells allows the classification of anticancer drugs according to their mode of action. Analyst 136 (6), 1134–41.

Draux, F., Jeannesson, P., Gobinet, C., Josep, S., Pijanka, J., Sandt, C., Dumas, P., Manfait, M., Sockalingum, G. D., 2009. IR spectroscopy reveals effect of non-cytotoxic doses of anti-tumour drug on cancer cells. Analytical and Bioanalytical Chemistry 395 (7), 2293–301.

Evans, C. L., Potma, E. O., Puoris' haag, M., Côté, D., Lin, C. P., Xie, X. S., 2005. Chemical imaging of tissue in vivo with video-rate coherent anti-stokes raman scattering microscopy. Proceedings of the National Academy of Sciences of the United States of America 102 (46), 16807–16812.

Fale, P. L., Altharawi, A., Chan, A. K. L., 2015. In situ fourier transform infrared analysis of live cells' response to doxorubicin. Biochimica et Biophysica Acta (BBA)-Molecular Cell Research 1853 (10), 2640–2648.

Fang, Y., 2006. Label-free cell-based assays with optical biosensors in drug discovery. Assay and drug development technologies 4 (5), 583–595.

Fang, Y., 2014. Label-free drug discovery. Front Pharmacol 5, 52.

Farhane, Z., Bonnier, F., Casey, A., Byrne, H. J., 2015. Raman micro spectroscopy for in vitro drug screening: subcellular localisation and interactions of doxorubicin. Analyst 140 (12), 4212–4223.

Fayer, M. D., 2001. Elements of quantum mechanics. Oxford University Press on Demand.

Flower, K. R., Khalifa, I., Bassan, P., Démoulin, D., Jackson, E., Lockyer, N. P., T, M. A., Miles, P., Vaccari, L., Gardner, P., 2011. Synchrotron FTIR analysis of drug treated ovarian a2780 cells: an ability to differentiate cell response to different drugs? Analyst 136 (3), 498.

Fu, D., Zhou, J., Zhu, W. S., Manley, P. W., Wang, Y. K., Hood, T., Wylie, A., Xie, X. S., 2014. Imaging the intracellular distribution of tyrosine kinase inhibitors in living cells with quantitative hyperspectral stimulated raman scattering. Nature chemistry 6 (7), 614–622.

Gazi, E., Dwyer, J., Gardner, P., Ghanbari-Siahkali, A., Wade, A., Miyan, J., Lockyer, N. P., Vickerman, J. C., Clarke, N. W., Shanks, J. H., et al., 2003. Applications of fourier transform infrared microspectroscopy in studies of benign prostate and prostate cancer. a pilot study. The Journal of pathology 201 (1), 99–108.

Geladi, P., Kowalski, B. R., 1986. Partial least-squares regression: a tutorial. Analytica chimica acta 185, 1–17.

Gelfand, P., Smith, R. J., Stavitski, E., Borchelt, D. R., Miller, L. M., 2015. Characterization of protein structural changes in living cells using Time-Lapsed FTIR imaging. Analytical ....

Golosovsky, M., Lirtsman, V., Yashunsky, V., Davidov, D., Aroeti, B., 2009. Mid-infrared surface-plasmon resonance: A novel biophysical tool for studying living cells. Journal of Applied Physics 105 (10).

Grenci, G., Birarda, G., Mitri, E., Businaro, L., Pacor, S., Vaccari, L., Tormen, M., 2012. Optimization of microfluidic systems for IRMS long term measurement of living cells. Microelectronic Engineering 98, 698–702.

Gronholtz, J., Herres, W., 1984. Understanding ft-ir data processing. part 1: Data acquisition and fourier transformation. Comp. App. Lab 2, 216.

Holman, H.-Y. N., Goth-Goldstein, R., Martin, M. C., Russell, M. L., McKinney, W. R., 2000a. Low-dose responses to 2, 3, 7, 8-tetrachlorodibenzo-p-dioxin in single living human cells measured by synchrotron infrared spectromicroscopy. Environmental science & technology 34 (12), 2513–2517.

Holman, H.-Y. N., Martin, M. C., Blakely, E. A., Bjornstad, K., McKinney, W. R., 2000b. Ir spectroscopic characteristics of cell cycle and cell death probed by synchrotron radiation based fourier transform ir spectromicroscopy. Biopolymers 57 (6), 329–335.

Hosokawa, M., Ando, M., Mukai, S., Osada, K., Yoshino, T., Hamaguchi, H.-o., Tanaka, T., 2014. In vivo live cell imaging for the quantitative monitoring of lipids by using raman microspectroscopy. Analytical chemistry 86 (16), 8224–8230.

Jackson, R. S., 2006. Continuous scanning interferometers for mid-infrared spectrometry. Handbook of Vibrational Spectroscopy. Vol. 1. John Wiley & Sons, Ltd.

Jaouen, G., Vessières, A., 1985. Transition metal carbonyl oestrogen receptor assay. Pure and applied chemistry 57 (12), 1865–1874.

Jaouen, G., Vessieres, A., Top, S., Ismail, A. A., Butler, I. S., 1985. Metal carbonyl fragments as a new class of markers in molecular biology. Journal of the American Chemical Society 107 (16), 4778–4780.

Jimenez-Hernandez, M., Brown, Hughes, C., Clarke, N., Gardner, P., 2015. Characterising cytotoxic agent action as a function of the cell cycle using fourier transform infrared microspectroscopy. Analyst.

Kakita, M., Okuno, M., Hamaguchi, H.-o., 2013. Quantitative analysis of the redox states of cytochromes in a living l929 (nctc) cell by resonance raman microspectroscopy. Journal of biophotonics 6 (3), 256–259.

Kandel, M. E., Sridharan, S., Liang, J., Luo, Z., Han, K., Macias, V., Shah, A., Patel, R., Tangella, K., Kajdacsy-Balla, A., et al., 2017. Label-free tissue scanner for colorectal cancer screening. Journal of Biomedical Optics 22 (6), 066016.

Kang, J. W., So, P. T., Dasari, R. R., Lim, D.-K., 2015. High resolution live cell raman imaging using subcellular organelle-targeting sers-sensitive gold nanoparticles with highly narrow intra-nanogap. Nano letters 15 (3), 1766–1772.

Kasprowicz, R., Suman, R., O'Toole, P., 2017. Characterising live cell behaviour: Traditional label-free and quantitative phase imaging approaches. The international journal of biochemistry & cell biology 84, 89–95.

Kazarian, S. G., Chan, K. L. A., 2010. Micro-and macro-attenuated total reflection fourier transform infrared spectroscopic imaging. Applied Spectroscopy 64 (5), 135A–152A.

Kidder, L. H., Haka, A. S., Lewis, E. N., 2006. Instrumentation for ft-ir imaging. Handbook of Vibrational Spectroscopy. John Wiley & Sons, Ltd.

Kimber, J. A., Foreman, L., Turner, B., Rich, P., Kazarian, S. G., 2016. FTIR spectroscopic imaging and mapping with correcting lenses for studies of biological cells and tissues. Faraday Discuss.

Kitadai, N., Sawai, T., Tonoue, R., Nakashima, S., Katsura, M., Fukushi, K., 2014. Effects of ions on the oh stretching band of water as revealed by atr-ir spectroscopy. Journal of Solution Chemistry 43 (6), 1055–1077.

Klein, K., Gigler, A. M., Aschenbrenner, T., Monetti, R., Bunk, W., Jamitzky, F., Morfill, G., Stark, R. W., Schlegel, J., 2012. Label-free live-cell imaging with confocal raman microscopy. Biophysical journal 102 (2), 360–368.

Koch, C., Posch, A. E., Goicoechea, H. C., Herwig, C., Lendl, B., 2014. Multi-analyte quantification in bioprocesses by fourier-transform-infrared spectroscopy by partial least squares regression and multivariate curve resolution. Analytica chimica acta 807, 103–110.

Kong, K. V., Chew, W., Lim, L. H. K., Fan, W. Y., Leong, W. K., 2007. Bioimaging in the mid-infrared using an organometallic carbonyl tag. Bioconjugate chemistry 18 (5), 1370–1374.

Kozlov, D., Besov, A., 2011. Method of spectral subtraction of Gas-Phase fourier transform infrared (FT-IR) spectra by minimizing the spectrum length. Applied Spectroscopy 65 (8), 918–923.

Kühn, J., Shaffer, E., Mena, J., Breton, B., Parent, J., Rappaz, B., Chambon, M., Emery, Y., Magistretti, P., Depeursinge, C., et al., 2013. Label-free cytotoxicity screening assay by digital holographic microscopy. Assay and drug development technologies 11 (2), 101–107.

Kuimova, M. K., Chan, A. K. L., Kazarian, S. G., 2009. Chemical imaging of live cancer cells in the natural aqueous environment. Applied Spectroscopy 63 (2), 164–171.

Kuzmin, A. N., Pliss, A., Lim, C.-K., Heo, J., Kim, S., Rzhevskii, A., Gu, B., Yong, K.-T., Wen, S., Prasad, P. N., 2016. Resonance raman probes for organelle-specific labeling in live cells. Scientific reports 6.

Li, Y., Almassalha, L. M., Chandler, J. E., Zhou, X., Stypula-Cyrus, Y. E., Hujsak, K. A., Roth, E. W., Bleher, R., Subramanian, H., Szleifer, I., et al., 2017. The effects of chemical fixation on the cellular nanostructure. Experimental Cell Research.

Lipiec, E., Bambery, K. R., Heraud, P., Kwiatek, W. M., McNaughton, D., Tobin, M. J., Vogel, C., Wood, B. R., 2014. Monitoring uvr induced damage in single cells and isolated nuclei using sr-ftir microspectroscopy and 3d confocal raman imaging. Analyst 139 (17), 4200–4209.

Loutherback, K., Chen, L., Holman, H.-Y. N., 2015. Open-channel microfluidic membrane device for long-term ft-ir spectromicroscopy of live adherent cells. Analytical chemistry 87 (9), 4601–4606.

Majeed, H., Kandel, M. E., Han, K., Luo, Z., Macias, V., Tangella, K., Balla, A., Popescu, G., 2015. Breast cancer diagnosis using spatial light interference microscopy. Journal of biomedical optics 20 (11), 111210–111210.

Mariangela, C., Seydou, Y., Diego, S., Sabine, C., Augusto, M., Petibois, C., 2011. Experimental ATR device for real-time FTIR imaging of living cells using brilliant synchrotron radiation sources. Biotechnology Advances 31 (3), 402–7.

Marquet, P., Depeursinge, C., Magistretti, P. J., 2014. Review of quantitative phase-digital holographic microscopy: promising novel imaging technique to resolve neuronal network activity and identify cellular biomarkers of psychiatric disorders. Neurophotonics 1 (2), 020901–020901.

Marquet, P., Rappaz, B., Magistretti, P. J., Cuche, E., Emery, Y., Colomb, T., Depeursinge, C., 2005. Digital holographic microscopy: a noninvasive contrast imaging technique allowing quantitative visualization of living cells with subwavelength axial accuracy. Opt Lett 30 (5), 468.

Mattson, E. C., Unger, M., Clède, S., Lambert, F., Policar, C., Imtiaz, A., Roshan, D., Hirschmugl, C. J., 2013. Toward optimal spatial and spectral quality in wide-field infrared spectromicroscopy of IR labelled single cells. Analyst 138 (19), 5610–5618.

Mazzarello, P., 1999. A unifying concept: the history of cell theory. Nature Cell Biology 1 (1), E13–E15.

Meister, K., Niesel, J., Schatzschneider, U., Metzler-Nolte, N., Schmidt, D. A., Havenith, M., 2010. Label-free imaging of metal–carbonyl complexes in live cells

by raman microspectroscopy. Angewandte Chemie International Edition 49 (19), 3310–3312.

Mertz, J., 2004. Nonlinear microscopy: new techniques and applications. Current opinion in neurobiology 14 (5), 610–616.

Miller, L. M., Dumas, P., 2006. Chemical imaging of biological tissue with synchrotron infrared light. Biochimica et Biophysica Acta (BBA)-Biomembranes 1758 (7), 846–857.

Miller, L. M., Dumas, P., 2010. From structure to cellular mechanism with infrared microspectroscopy. Current Opinion in Structural Biology 20 (5), 649–656.

Mirabella, F. M., 2006. Principles, theory and practice of internal reflection spectroscopy. Handbook of Vibrational Spectroscopy. Vol. 1. John Wiley & Sons, Ltd.

Mitri, E., Birarda, G., Vaccari, L., Kenig, S., Tormen, M., Grenci, G., 2014. SU-8 bonding protocol for the fabrication of microfluidic devices dedicated to FTIR microspectroscopy of live cells. Lab on a Chip 14 (1), 210–218.

Mitri, E., Kenig, S., Coceano, G., Bedolla, D. E., Tormen, M., Grenci, G., Vaccari, L., 2015. Time-resolved ft-ir microspectroscopy of protein aggregation induced by heat-shock in live cells. Analytical chemistry 87 (7), 3670–3677.

Moffat, J. G., Vincent, F., Lee, J. A., Eder, J., Prunotto, M., 2017. Opportunities and challenges in phenotypic drug discovery: an industry perspective. Nature Reviews Drug Discovery 16 (8), nrd–2017.

Molder, A., Sebesta, M., Gustassson, M., Gisselson, L., Wingren, A. G., Alm, K., 2008. Non-invasive, label-free cell counting and quantitative analysis of adherent cells using digital holography. Journal of Microscopy 232 (2), 240–247.

Mouras, R., Bagnaninchi, P., Downes, A., Elfick, A., 2013. Multimodal, label-free nonlinear optical imaging for applications in biology and biomedical science. Journal of Raman Spectroscopy 44 (10), 1373–1378.

Munro, K., Bambery, K., Carter, E., Puskar, L., Tobin, M., Wood, B., Dillon, C., 2010. Synchrotron radiation infrared microspectroscopy of arsenic-induced changes to intracellular biomolecules in live leukemia cells. Vibrational Spectroscopy 53 (1), 39–44.

Nasse, M. J., Walsh, M. J., Mattson, E. C., Reininger, R., André, K., Macias, V., Bhargava, R., Hirschmugl, C. J., 2011. High-resolution fourier-transform infrared

chemical imaging with multiple synchrotron beams. Nature Methods 8 (5), 413–416.

Noda, I., 1989. Two-dimensional infrared spectroscopy. Journal of the American Chemical Society 111 (21), 8116–8118.

Noda, I., 1993. Generalized two-dimensional correlation method applicable to infrared, raman, and other types of spectroscopy. Applied Spectroscopy.

Noda, I., 2000. Determination of Two-Dimensional correlation spectra using the hilbert transform. Appl Spectrosc 54 (7), 994–999.

Noda, I., Ozaki, Y., 2005. Two-dimensional correlation spectroscopy: applications in vibrational and optical spectroscopy. John Wiley & Sons.

Norman, R., Lodwich, D., 2007. The Flesh and Bones of Medical Cell Biology. Mosby.

Onogi, C., Hamaguchi, H.-o., 2010. In vivo resonance raman detection of ferrous cytochrome c from mitochondria of single living yeast cells. Chemistry Letters 39 (3), 270–271.

Palonpon, A. F., Sodeoka, M., Fujita, K., 2013. Molecular imaging of live cells by raman microscopy. Current opinion in chemical biology 17 (4), 708–715.

Pavillon, N., Fujita, K., Isaac Smith, N., 2014. Multimodal label-free microscopy. Journal of Innovative Optical Health Sciences 7 (05), 1330009.

Pike Technologies, 2011. ATR CRYSTAL SELECTION. Online.
URL `https://www.piketech.com/ATR-Crystal-Selection.html`

Pilling, M., Gardner, P., 2016. Fundamental developments in infrared spectroscopic imaging for biomedical applications. Chem Soc Rev 45 (7), 1935–1957.

Policar, C., Waern, J., Plamont, M., Clède, S., Mayet, C., Prazeres, R., Ortega, J., Vessières, A., Dazzi, A., 2011. Subcellular IR imaging of a Metal–Carbonyl moiety using photothermally induced resonance. Angew Chem-ger Edit 123 (4), 890–894.

Quaroni, L., Obst, M., Nowak, M., Zobi, F., 2015. Three-dimensional mid-infrared tomographic imaging of endogenous and exogenous molecules in a single intact cell with subcellular resolution. Angewandte Chemie International Edition 54 (1), 318–322.

Quaroni, L., Zlateva, T., 2014. Real-time metabolic analysis of living cancer cells with correlated cellular spectro-microscopy. Analytical chemistry 86 (14), 6887–6895.

Rahmelow, K., Hubner, W., 1997. Infrared spectroscopy in aqueous solution: Difficulties and accuracy of water subtraction. Applied Spectroscopy 51 (2), 160–170.

Rappaz, B., Breton, B., Shaffer, E., Turcatti, G., 2014. Digital holographic microscopy: a quantitative label-free microscopy technique for phenotypic screening. Combinatorial chemistry & high throughput screening 17 (1), 80–88.

Reddy, R. K., Walsh, M. J., Schulmerich, M. V., Carney, S. P., Bhargava, R., 2013. High-definition infrared spectroscopic imaging. Applied Spectroscopy 67 (1), 93–105.

Sako, Y., Uyemura, T., 2002. Total internal reflection fluorescence microscopy for single-molecule imaging in living cells. Cell structure and function 27 (5), 357–365.

Salehi, H., Derely, L., Vegh, A.-G., Durand, J.-C., Gergely, C., Larroque, C., Fauroux, M.-A., Cuisinier, F. J., 2013. Label-free detection of anticancer drug paclitaxel in living cells by confocal raman microscopy. Applied Physics Letters 102 (11), 113701.

Salmain, M., Vessières, A., Brossier, P., Butler, I. S., Jaouen, G., 1992. Carbonylmetalloimmunoassay (cmia) a new type of non-radioisotopic immunoassay: Principles and application to phenobarbital assay. Journal of immunological methods 148 (1-2), 65–75.

Salmain, M., Vessieres, A., Jaouen, G., Butler, I. S., 1991. Fourier transform infrared spectroscopic method for the quantitative trace analysis of transition-metal carbonyl-labeled bioligands. Analytical chemistry 63 (20), 2323–2329.

Sandt, C., Frederick, J., Dumas, P., 2013. Profiling pluripotent stem cells and organelles using synchrotron radiation infrared microspectroscopy. Journal of biophotonics 6 (1), 60–72.

Schmidt, M., Wolfram, T., Rumpler, M., Tripp, C., 2007. Live cell adhesion assay with attenuated total reflection infrared spectroscopy. Biointerphases.

Schwaighofer, A., Alcaráz, M. R., Araman, C., Goicoechea, H., Lendl, B., 2016. External cavity-quantum cascade laser infrared spectroscopy for secondary structure analysis of proteins at low concentrations. Scientific Reports 6, 33556.

Shinzawa, H., Mizukado, J., Kazarian, S. G., 2016. Fourier transform infrared (FT-IR) spectroscopic imaging analysis of partially miscible PMMA-PEG blends using Two-Dimensional disrelation mapping. Appl Spectrosc 71, 1189–1197.

Shinzawa, H., Turner, B., Mizukado, J., Kazarian, S. G., 2017. Protein hydration in living cells probed by fourier transform infrared (FT-IR) spectroscopic imaging. Analyst 142, 2475–2483.

Sommer, A. J., 2006. Mid-infrared transmission microspectroscopy. Handbook of Vibrational Spectroscopy. Vol. 1. John Wiley & Sons, Ltd.

Stephens, D. J., Allan, V. J., 2003. Light microscopy techniques for live cell imaging. Science 300 (5616), 82–86.

Sun, Q., 2009. The raman oh stretching bands of liquid water. Vibrational Spectroscopy 51 (2), 213–217.

Taylor, M. W., 2014. Viruses and Man: A History of Interactions. Springer.

Theocharous, E., Birch, J., 2006. Detectors for mid- and far-infrared spectrometry: Selection and use. Handbook of Vibrational Spectroscopy. Vol. 1. John Wiley & Sons, Ltd.

Tipping, W. J., Lee, M., Serrels, A., Brunton, V. G., Hulme, A. N., 2017. Imaging drug uptake by bioorthogonal stimulated raman scattering microscopy. Chemical Science 8, 5606–5615.

Tiwari, S., Ando, M., Hamaguchi, H., 2013. Investigation of organelle-specific intracellular water structures with raman microspectroscopy. Journal of Raman Spectroscopy 44 (2), 167–169.

Trevisan, J., Angelov, P. P., Scott, A. D., Carmichael, P. L., Martin, F. L., 2013. Irootlab: a free and open-source matlab toolbox for vibrational biospectroscopy data analysis. Bioinformatics 29 (8), 1095–1097.

Vaccari, L., Birarda, G., Businaro, L., Pacor, S., Grenci, G., 2012a. Infrared microspectroscopy of live cells in microfluidic devices (MD-IRMS): toward a powerful Label-Free Cell-Based assay. Analytical Chemistry 84 (11), 4768–4775.

Vaccari, L., Birarda, G., Grenci, G., Pacor, S., Businaro, L., 2012b. Synchrotron radiation infrared microspectroscopy of single living cells in microfluidic devices: advantages, disadvantages and future perspectives. J Phys Conf Ser 359 (1), 012007.

van de Linde, S., Heilemann, M., Sauer, M., 2012. Live-Cell Super-Resolution imaging with synthetic fluorophores. Annual Review of Physical Chemistry.

Venyaminov, S. Y., Prendergast, F. G., 1997. Water (h2o and d2o) molar absorptivity in the 1000-4000 cm-1 range and quantitative infrared spectroscopy of aqueous solutions. Analytical Biochemistry 248 (2), 234–245.

Vobornik, D., Margaritondo, G., Sanghera, J., Thielen, P., Aggarwal, I., Ivanov, B., Tolk, N., Manni, V., Grimaldi, S., Lisi, A., et al., 2005. Spectroscopic infrared scanning near-field optical microscopy (ir-snom). Journal of alloys and compounds 401 (1), 80–85.

Walsh, M., Reddy, R., Bhargava, R., 2012. Label-Free biomedical imaging with Mid-IR spectroscopy. IEEE Journal of Selected Topics in Quantum Electronics 18 (4), 15021513.

Wei, L., Hu, F., Chen, Z., Shen, Y., Zhang, L., Min, W., 2016. Live-cell bioorthogonal chemical imaging: stimulated raman scattering microscopy of vibrational probes. Accounts of chemical research 49 (8), 1494–1502.

Wei, L., Yu, Y., Shen, Y., Wang, M. C., Min, W., 2013. Vibrational imaging of newly synthesized proteins in live cells by stimulated raman scattering microscopy. Proceedings of the National Academy of Sciences 110 (28), 11226–11231.

Weigelin, B., Bakker, G.-J., Friedl, P., 2016. Third harmonic generation microscopy of cells and tissue organization. J Cell Sci 129 (2), 245–255.

Whelan, D., Bambery, K., Puskar, L., Don, M., Wood, B., 2013. Synchrotron fourier transform infrared (FTIR) analysis of single living cells progressing through the cell cycle. Analyst 138 (14), 3891–3899.

Wrobel, T., Vichi, A., Baranska, M., 2015. Micro-attenuated total reflection fourier transform infrared (micro atr ft-ir) spectroscopic imaging with variable angles of incidence. Applied Spectroscopy.

Wu, P., Siesler, H., 2003. Water diffusion into epoxy resin: a 2D correlation ATR-FTIR investigation. Chemical Physics Letters 374 (1-2), 74–78.

Wu, Q., Ghislain, L. P., Elings, V., 2000. Imaging with solid immersion lenses, spatial resolution, and applications. Proceedings of the IEEE 88 (9), 1491–1498.

Yalamanchili, M., Atia, A., Miller, J., 1996. Analysis of interfacial water at a hydrophilic silicon surface by in-situ ftir/internal reflection spectroscopy. Langmuir 12 (17), 4176–4184.

Yamakoshi, H., Palonpon, A., Dodo, K., Ando, J., Kawata, S., Fujita, K., Sodeoka, M., 2015. A sensitive and specific raman probe based on bisarylbutadiyne for live cell imaging of mitochondria. Bioorganic & medicinal chemistry letters 25 (3), 664–667.

Yamakoshi, H., Palonpon, A. F., Dodo, K., Ando, J., Kawata, S., Fujita, K., Sodeoka, M., 2014. Simultaneous imaging of protonated and deprotonated carbonylcyanide p-trifluoromethoxyphenylhydrazone in live cells by raman microscopy. Chemical Communications 50 (11), 1341–1343.

Yamauchi, T., Iwai, H., Yamashita, Y., 2011. Label-free imaging of intracellular motility by low-coherent quantitative phase microscopy. Optics express 19 (6), 5536–5550.

Yang, J., Cui, Y., Zong, S., Zhang, R., Song, C., Wang, Z., 2012. Tracking multiplex drugs and their dynamics in living cells using the label-free surface-enhanced raman scattering technique. Molecular pharmaceutics 9 (4), 842–849.

Zhang, C., Li, J., Lan, L., Cheng, J.-X., 2017. Quantification of lipid metabolism in living cells through the dynamics of lipid droplets measured by stimulated raman scattering imaging. Analytical Chemistry 89 (8), 4502–4507.

Zhang, D., Li, C., Zhang, C., Slipchenko, M. N., Eakins, G., Cheng, J.-X., 2016. Depth-resolved mid-infrared photothermal imaging of living cells and organisms with submicrometer spatial resolution. Science advances 2 (9), e1600521.

Zheng, N., Tsai, H. N., Zhang, X., Rosania, G. R., 2011. The subcellular distribution of small molecules: from pharmacokinetics to synthetic biology. Molecular pharmaceutics 8 (5), 1619–1628.

Ziblat, R., Lirtsman, V., Davidov, D., Aroeti, B., 2006. Infrared surface plasmon resonance: A novel tool for real time sensing of variations in living cells. Biophysical Journal 90 (7), 2592–2599.

Zilbershtein, A., Golosovsky, M., Lirtsman, V., Aroeti, B., Davidov, D., 2012. Quantitative surface plasmon spectroscopy: Determination of the infrared optical constants of living cells. Vibrational Spectroscopy 61, 43–49.

Zucchiatti, P., Mitri, E., Kenig, S., Billè, F., Kourousias, G., Bedolla, D. E., Vaccari, L., 2016. Contribution of ribonucleic acid (rna) to the fourier transform infrared (ftir) spectrum of eukaryotic cells. Analytical Chemistry 88 (24), 12090–12098.

Appendices

Table 7.1: Table summarising the properties of the main label-free microscopy techniques discussed in section 2.2.*Lateral resolution of infrared spectroscopic imaging is typically 8 µm in transmission mode and 3 µm in ATR mode.

Technique	Resolution	Advantages & Disadvantages
Quantitative phase microscopy	0.4 µm	**Advantages** fast acquisition quantitative measure of optical thickness **Disadvantages** no chemical information obtained
Second harmonic generation microscopy	0.5 µm	**Advantages** optical sectioning without confocal setup deep tissue imaging possible **Disadvantages** non-centrosymetric symmetry required high power pulsed laser system required
Third harmonic generation microscopy	0.4 µm	**Advantages** optical sectioning without confocal setup Third order optical response seen in all media **Disadvantages** high power pulsed laser system required
Raman mapping	1 µm	**Advantages** chemical information obtained high resolution compared to infrared **Disadvantages** high power laser required long acquisition time typically low sensitivity without use of SERS probes

Technique	Resolution	Advantages & Disadvantages
Infrared spectroscopic imaging	3/8* µm	**Advantages** low risk of photo-damage fast acquisition of spectroscopic images **Disadvantages** high absorbance of infrared light by water relatively low lateral resolution
Nonlinear Raman microscopy	1 µm	**Advantages** fast acquisition of specific frequencies chemical information obtained **Disadvantages** acquisition is slow if whole spectrum is required nonlinear optical setup required high power pulsed lasers are required